Neutron scattering study of the iron based superconductors

A Dissertation Presented for the

Doctor of Philosophy

Degree

The University of Tennessee, Knoxville

Miaoyin Wang

August 2013

To my parents, whose love and support made me who I am.

Acknowledgements

First, I would like to thank my adviser Professor Pengcheng Dai for his guidance in academics. His passion for science and dedication to his students have made these five years an extremely important portion of my life. I would like to thank the former members of Dai′s group: Dr. Shiliang Li, Dr. Oliver Lipscomb, Dr. Songxue Chi, Dr. Leland Harriger and Dr. Jun Zhao. I appreciate the supports from the current group members Chenglin Zhang, Mengshu Liu, Scott Carr, Yu Song, Yu Li and undergraduate students Zachary Sims, Nickolas F. Luttrell, Jim Teal, Caleb Redding and Tucker Netherton.

I would like to give my special thanks to Dr. Chenglin Zhang and Dr. Songxue Chi for their generous help throughout my Ph.D. studies; Dr. Guotai Tan for his hard work in the lab and his great efforts in the crystal growth. I would also like to thank Dr. Huiqian Luo, Dr. Meng Wang, Dr. Chunhong Li, Xingye Lu and Rui Zhang in IOP, Beijing, China, for their collaboration and sample growth.

I would like to acknowledge the help from all local contacts who have assisted me in my work: Douglas L. Abernathy (SNS, ORNL), Matthew B. Stone (SNS, ORNL), Mark Lumsden (HFIR, ORNL), Andy Christiansen (HFIR, ORNL), Wei Tian (HFIR, ORNL), Songxue Chi (HFIR, ORNL), Jeffery Lynn (NCNR, NIST) and Russell Ewings (ISIS, UK). Finally, I would like to acknowledge my collaborators Dr. Jiangpin Hu, Dr. Daoxin Yao and Dr. Fang Chen for their support with theories and calculations.

In the end, I am grateful to the NSF and DOE funding agencies that supported my work. Also, I am grateful to my committee members for their time and suggestions on my dissertation. I sincerely appreciate the help of the faculty and staff in the Department of Physics and Astronomy, University of Tennessee. I would like to thank UT and ORNL for their support and sponsorship.

Abstract

In most iron-based and copper-oxide superconductors, the T_c [superconducting critical temperature] gradually increases upon charge carrier doping or isovalent doping. In the under-doped regime of electron-doped $BaFe_2As_2$ [Barium Iron 2 Arsenic 2], the superconductivity appears before the complete suppression of AF [antiferromagnetic] long-range order, creating a SC-AF [superconducting-antiferromagnetic] coexisting area. The interplay between long-range magnetic order and superconductivity was studied using a triple-axis thermal neutron spectrometer under an in-plane magnetic field. The suppression of superconductivity and the enhancement of long-range AF order were discovered under 11 Tesla, suggesting the competing nature of these two phases and the itinerant nature of iron-pnictides. We also measured the evolution of the neutron spin resonance in under-doped $BaFe_{1.925}Ni_{0.075}As_2$ [Barium Iron 1.925 Nickel 0.075 As 2] and in over-doped $BaFe_{1.85}Ni_{0.15}As_2$ [Barium Iron 1.85 Nickel 0.15 As 2]. Combining the previous results, we were able to compare the evolution of the neutron spin resonance energies in both $BaFe_{2-x}Ni_xAs_2$ [Barium Iron (2-x) Nickel (x) Arsenic 2] and $BaFe_{2-x}Co_x$ As_2 [Barium Iron (2-x) Cobalt (x) Arsenic 2].

In late 2010, another type of iron-based superconductor alkali iron selenide $A_{0.8}Fe_{1.6+y}Se_2$ [Alkali 0.8 Iron (1.6+y) Selenium 2] (or 245 system) was discovered. It is a unique system among the family of unconventional (high-T_c) superconductors because of its novel phase diagram, insulating parent compounds and huge magnetic moment. Using the inelastic time-of-flight technique, we are able to show that the parent compound can be described well by a local Heisenberg model. The follow

up experiments on a superconducting sample (below and above T_c) and insulating samples (below and above T_n [Neel Temperature]) provide a more detailed comparison and show more evidence that the alkali iron selenide system is rather different from either itinerant iron-pnictides or local copper-oxide systems.

Preface

Portions of this dissertation are derived from published work. The publication information of each work is listed with its corresponding chapter.

Chapter 3.1:

Miaoyin Wang, Huiqian Luo, Jun Zhao, Chenglin Zhang, Meng Wang, Karol Marty, Songxue Chi, Jeffrey W. Lynn, Astrid Schneidewind, Shiliang Li, Pengcheng Dai

Phys. Rev. B ***81****, 174524(2010)*

Chapter 3.2:

Miaoyin Wang, Huiqian Luo, Meng Wang, Songxue Chi, Jose A. Rodriguez-Rivera, Deepak Singh, Sung Chang, Jeffrey W. Lynn, Pengcheng Dai

Phys. Rev. B ***83****, 094516(2011)*

Chapter 4.1:

Miaoyin Wang, Chen Fang, Dao-Xin Yao, GuoTai Tan, Leland W. Harriger, Yu Song, Tucker Netherton, Chenglin Zhang, Meng Wang, Matthew B. Stone, Wei Tian, Jiangping Hu, Pengcheng Dai

Nature Communications ***2****, 580 (2011)*

Chapter 4.2:

Miaoyin Wang, Xingye Lu, R. A. Ewings, Leland W. Harriger, Yu Song, Scott V.

Carr, Chunhong Li, Rui Zhang, Pengcheng Dai

Phys. Rev. B ***87****, 064409 (2013)*

Chapter 4.3:

Miaoyin Wang, Chunhong Li, D. L. Abernathy, Yu Song, Scott V. Carr, Xingye Lu, Shiliang Li, Zahra Yamani, Jiangping Hu, Tao Xiang, Pengcheng Dai

Phys. Rev. B ***86****, 024502 (2012)*

Table of Contents

Chapter 1

Introduction

1.1 A general introduction to superconductors

1.1.1 Conventional superconductors

Superconductivity is a phenomenon of zero resistivity in materials when cooled below certain temperature. It was discovered in 1911, when Dutch physicist Onnes tested the validity of the Drude theory at very low temperatures [1]. According to the Drude theory, resistivity in a metal decreases as temperature decreases, and saturates to a finite resistance ρ_0 near base temperature. The Drude law was tested and confirmed in several materials before an astonishing result was obtained in mercury. At $\sim$4 Kelvin, mercury underwent a transition, and its resistivity dropped from a finite value to a non-measurable small value, which was later found to be zero (Figure 1.1). The discovery triggered a vast amount of research on superconductivity properties in many sorts of materials.

The concept of superconductivity was broadened in 1933 by Meissner and Ochesenfeld/s discovery on the expulsion of magnetic flux when a material entered a superconducting state [2]. Below certain critical magnetic fields, the magnetic flux will be completely excluded from the superconductor, producing a magnetic susceptibility χ= -1, making superconductors perfect diamagnets. It should be noted that the Meissner effect is thought to be independent of the zero resistivity. Although the zero resistivity can explain the repulsion of the magnetic field when the field is applied after the cooling of the sample below T_c, it cannot explain the fact that the magnetic field is still repulsed, even when it is applied before cooling (as shown in figure 1.2). Compared with the zero resistivity, the Meissner effect is the more favored way to demonstrate the superconducting property of a sample for two reasons. The first reason is simple: it is easier to measure susceptibility than resistivity, since no electrical leads need to be attached to the sample. The second reason is that the Meissner effect is a property of thermal equilibrium, based on the fact that the final state of a superconducting system does not depend on the history

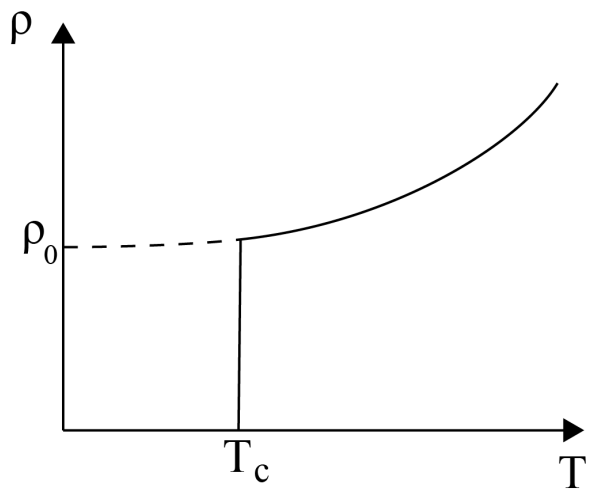

Figure 1.1: Schematic of the resistivity response to superconductivity. When the metal is cooled down near zero Kelvin, the resistivity, according to Drude theory, saturates at a finite value ρ_0 (dashed line). In superconductors, the resistivity will suddenly drop to zero at the superconducting transition temperature T_c.

of the sample. Resistivity, on the other hand, is a nonequilibrium effect. These two reasons make the Meissner effect an essential proof if one is to claim that a sample is superconducting. In all our experiments, we use susceptibility as the demonstration of the superconductivity and its volume fraction.

Although many materials were found to be superconducting soon after the first superconductor was discovered, and some phonological theories such as the London equation [3] and the Ginzburg-Landau model did explain some properties of superconductivity, its mechanism was not explained until the BCS theory in 1957 [4]. Before the BCS theory, the so-called isotope effect found the correlation between the mass of ions to the T_c, suggesting that superconductivity in metal might be related to phonons. BCS theory, established by Bardeen, Cooper, and Schrieffer, suggests that the Bose condensation of phonon-mediated electron pairs (named Cooper pairs) may generate superconductivity. The attraction potentials between electrons, no matter how small, will result in the formation of Cooper pairs. For electrons moving in a

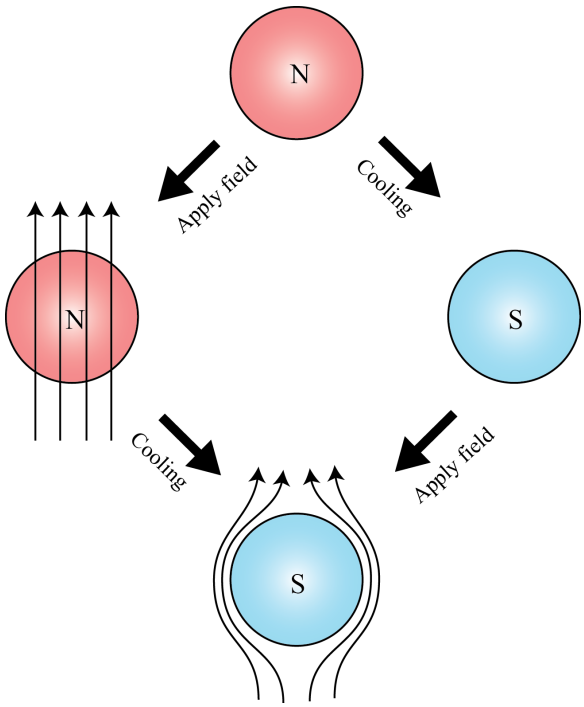

Figure 1.2: Schematic of the Meissner effect in superconductors. In the top panel, a sample starts with a temperature above T_c and zero magnetic field. In the bottom panel, the sample is already in a superconducting state, and the magneic field is expelled from the sample. This final state can be achieved either by applying the magnetic field first and then cooling below T_c (left panel) or by cooling first and then applying the magnetic field (right panel).

vacuum, the electron-electron Coulomb interactions are long-ranged repulsions. But in a metal, a passing electron can trigger displacement/vibration of positive ions (electron-phonon) and generated a local high positive charge area, which is attractive to other electrons with opposite spins (phonon-electron). The strong electron-phonon coupling holds two electrons together, and the two electrons form a ground state at an energy slightly lower than the Fermi surface. When thermal fluctuation is not strong enough to break the paring, the Cooper pairs become supercurrents that move with no resistance.

With the help of BCS theory, the conventional superconductors are now well understood, and their theoretical model has been established and proven correct.

But the success of the theory does not provide an unlimited boost of T_c in real materials, because the phonons cannot provide very strong coupling. Before 1986, it was generally believed that the highest T_c had a theoretical limit around 25−30K. As we look back from 2013, this belief is partially correct: the highest T_c found in BCS superconductors so far is 40K (MgB_2) [5]. On the other hand, the copper-oxide-based superconductors discovered in 1986 have T_c up to 140K [6, 7], much higher than any possible prediction of phonon-coupled BCS theory. These new types of superconducting materials have properties dramatically different from those of previous SC systems, and thus were denominated unconventional superconductors.

1.1.2 Unconventional superconductors

One of the limitations of conventional superconductors is their relatively low critical temperature T_c. As mentioned in the previous chapter, given the strength of the phonon coupling, it is generally believed that it is hard for T_c to exceed ∼30K. The first high-temperature superconductor with $T_c = 35$K was discovered in LBCO ($La_{5-x}Ba_xCu_5O_5$) [6], followed by the groundbreaking YBCO ($YBa_2Cu_3O_{7-\delta}$) with T_c 93K [8], a temperature higher than the boiling point of liquid nitrogen. The unusually high T_c and magnetism convinced physicists that these materials were substantially different from conventional superconductors. The highest T_c found in copper-oxide-based superconductors (and all superconductors) was 153 K, in $HgBa_2Ca_2Cu_3O_{8+\delta}$ under pressure 150 kbar [9].

Although the copper-oxide superconductors vary in elements, and their crystal structures are different, they have similarly structured planar copper-oxide building blocks and magnetic order and spin dynamics, suggesting a shared origin of superconductivity [10, 11]. The copper-oxide layers are believed to be responsible for superconductivity. Because of their strong local properties and weak inter-layer coupling, in many cases only their in-plane properties are considered and modeled.

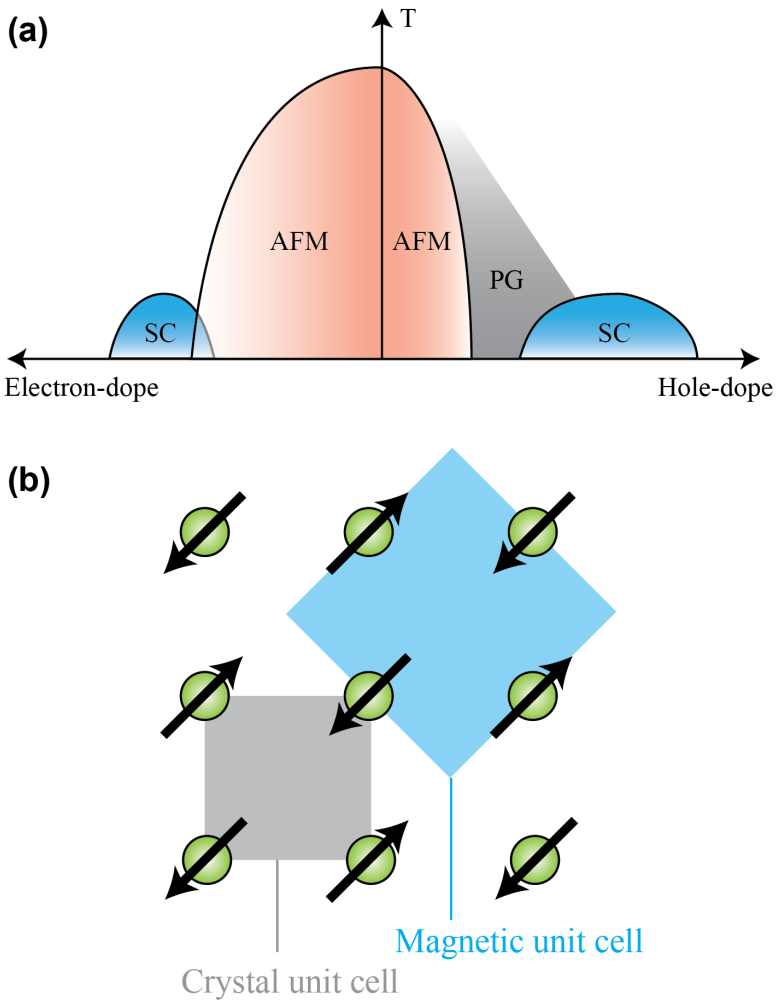

Figure 1.3: Schematic of (a) the phase diagram and (b) the magnetic structure of copper-oxide superconductors. The magnetic unit cell is marked with the cyan square, and the crystal unit cell is marked with the grey square.

Most of the cuprates become superconducting when they are electron- or hole-doped. The schematic of the cuprate phase diagram (figure 1.3(a)) shows the evolution of phases in cuprates, with charge carrier doping in the x-axis and temperature in the y-axis. At the center of the phase diagram are the un-doped parent compounds. These parent compounds are normally non-superconducting, with a well-defined long-range anti-ferromagnetic (AFM) order, the spins of which are located on the copper site. The typical magnetic structure of copper-oxides is shown

in figure 1.3(b). As can be seen from the phase diagram, the superconducting transition temperature T_c appears and gradually increases upon doping, then gradually decreases with further doping, forming a superconducting dome adjacent to the AFM dome. In the hole-doped case, the system first evolves gradually from a local, long-range-ordered Mott-insulating phase to a short-range-ordered spin-glass phase [12]. With more hole doping, the superconductivity dome appears and co-exists with the short range order, while the ordered moment is further suppressed. In the electron-doped case, the phase diagram is somewhat simpler [13, 14]: the AFM ordering is suppressed when lightly doped, similar to what happens in the hole-doped case. Other than entering a spin-glass state, the electron doping will bring the system directly from the AFM state to the SC state, with a regime in which the long range ordered AFM phase and the SC phase co-exist. It should be noted that, compared with hole-doped systems, less doping is needed to bring an electron-doped system into the superconducting dome. On the other hand, the optimal transition temperature T_c in hole-doped systems is normally higher than it is in electron-doped systems.

All the common features described above indicate that cuprates are substantially different from conventional BCS superconductors. The layered structure has an un-favored low symmetry for electron-phonon coupling. In conventional BCS superconductors, the existence of magnetism will destroy the Cooper pair and eliminate superconductivity; in unconventional superconductors, superconductivity can co-exist with the long-ranged AFM order, which could never happen if phonons were mediating the copper-pair.

After the great success of cuprates, physicists naturally wondered whether materials that do not contain copper would achieve similar or even higher T_c. The search continued for two decades, until the iron-based superconductors (IBS) were discovered [15, 16]. Although the T_c of IBS are not higher than that those of typical cuprates, the highest T_c still reaches $\sim$50K. Although they have a similar phase diagram, many fundamental properties of IBS are very different from those of cuprates. The discovery of two unconventional superconductor systems led physicists

to believe that unconventional superconductivity may exist in materials with different elements, crystal/magnetic structures, or transport properties, and to search with confidence for materials with higher T_c [17].

1.2 Iron-based superconductors

1.2.1 Family of iron-based superconductors

The iron-based superconductors (IBS) have many different systems that greatly enlarge the family of unconventional superconductors. The very first IBS system $LaFePO_{1-x}F_x$ was discovered by H. Hosono *et al.* in 2006 with $T_c \sim 4K$ [15], but it did not draw much attention until the same group substituted P by As and discovered a T_c of 30K in $LaFeAsO_{1-x}F_x$ in 2008 [16]. Before 2013, many IBS systems were discovered with different compositions and crystal structure classes. For convenience, different systems are denoted by the stoichiometric ratios of the chemical elements in their parent compounds. Under this notation, the major IBS systems are 1111, 122, 111, 11 and 245 (e.g. LaFeAsO, $BaFe_2As_2$, NaFeAs, FeTe and $Rb_2Fe_4Se_5$). Despite their different structures, all the IBS systems share a building block: iron-based square-planar sheets [18]. Similar to copper-oxide based superconductors, in which copper and oxygen form the superconducting layer, IBS systems have iron-based layers which are crucial to their unconventional superconductivity. The IBS classes listed above can be separated into two groups according to the element group of the atom that forms the superconducting layer with iron. The first group is the iron-pnictides, in which iron forms a zigzag layer with arsenic or phosphorous (Fe-As or Fe-P). The 1111, 111 and 122 classes belong to iron pnictides. They have similar magnetic structures despite their different crystal structures and symmetry groups. Compared with the other iron-pnictides, single crystals of 122 systems are easier to obtain and maintain, and they are usually larger. Chapter 3 focuses on one of these systems: electron-doped $BaFe_{2-x}Ni_xAs_2$. The second group is iron-chalcogenides, in which iron-selenium (Fe-Se) or iron-tellurium (Fe-Te) forms the superconducting layer; this group includes the 11 and 245 classes. Both the 11 and 245 classes present special properties. The 11 class only has one system: $Fe_{1+\delta}Te_{1-x}Se_x$. Unlike the iron-pnictides, it does not have any buffer layers between the Fe-(Te,Se) layers, and

the T_c is not only determined by Se doping level, but also related to the amount of extra iron in the compound. The 245 class is a relatively new member of iron-based superconductors (discovered in late 2010 [19]), and it is different from all the other classes of IBS in several respects. Chapter 4 deals with this material.

The discovery of iron-based superconductors is extremely important. Before 2008, copper-oxide-based superconductors were the only known kind of unconventional superconductors with relatively high T_c. A comparison of the IBS and cuprates reveals both great similarity and great difference. Table 3 [20] provides a decent comparison among conventional superconductors, cuprates, and IBS. Although both cuprates and IBS have layered structures and AFM-ordered parent compounds, the cuprate parent compounds are Mott-insulators, which are a result of strong local interaction, while the IBS parent compounds are magnetic bad metals, originating from long-range (non-local) magnetic correlations. Superconductivity was achieved in both cases by doping, but doping directly to the superconducting layers is allowed only in IBS, likely because they are more itinerant than cuprates. Iso-electronic doping also generates superconductivity in IBS, indicating that the structural parameters may tune the superconductivity. In superconducting samples, cuprates have an SC order parameter with a sign-changing d-wave symmetry, while the symmetry of the IBS has a sign-changing s-wave symmetry. In both the parent compounds and the superconductors of IBS systems, all five iron d-band electrons are partially occupied near the fermi-surface, which is quite different from cuprates in which a single-electron approach suffices.

Table 1.1: Properties of different classes of superconductors [20]

Property	Convensional superconductors	Copper oxides	Iron-based superconductors
T_c (maximum)	<30K	134K	56K
Correlation effects	None	Strong local electronic interaction	Long-range(non-local) magnetic correlation
Relation to magnetism	No magnetism	Magnetic insulating parent compounds	Megnetic metal parent compounds
Order parameter	One band single-sign s wave	One band sign-changing d wave	Five band sign-changing s wave(presumably)
Paring interaction	Electron-phonon	probably magnetic	probably magnetic
Dimensionality	Three dimensional	Two dimensional	Variable

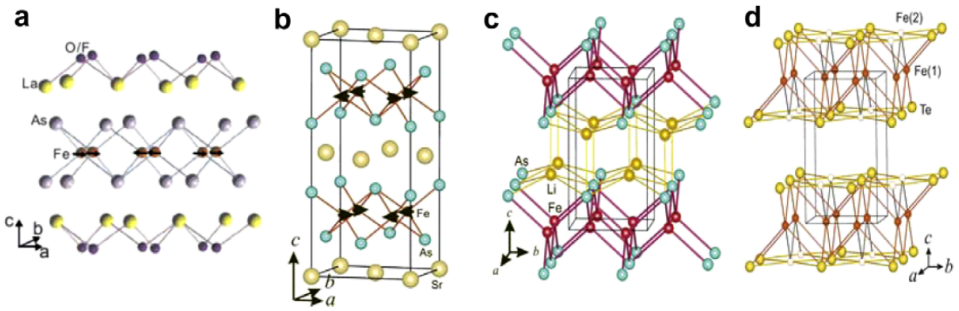

Figure 1.4: Crystal structures of four classes of iron-based superconductors: (a) LaFeAsO (b) $SrFe_2As_2$ (c) LiFeAs (d) $Fe_{1+x}Te$ (Ref. [18]).

1.2.2 Special case for alkaline iron selenide (245) systems

Before we continue detailing the properties of iron-based superconductors, it should be noted that the alkaline iron selenide materials are very different from the other classes (1111, 122, 111, and 11). This type of material has a unique crystal structure, and a unique magnetic structure with an unusually high structural/magnetic transition temperature; their phase diagrams and spin dynamics are also very different from those of other iron-based superconductor systems. Moreover, although the 245 has been known for two years, it is still unclear which phase of the chemical-separated phases is responsible for the superconductivity. On the basis of these facts, we discuss it separately in section 1.2.5.

1.2.3 Crystal and magnetic structures of parent compounds

In most IBS systems, superconductivity appears when the non-superconducting parent compounds are doped with charge carriers or isovalent chemical substitutions. Parent compounds represent the general properties of IBS, and are a good starting point for introducing the crystal structure and magnetic structure of IBS.

Crystal structure

Figure 1.4 shows the crystal structures of the typical 1111, 122, 111 and 11 systems [18]. In the 1111, 122 and 11 systems, every site was found to be fully occupied. In some 1111 systems, oxygen vacancies were created to generate a doping effect. For the 11 systems, there are two iron sites, and iron atoms partially occupy each site, while the Te/Se sites were considered fully occupied. The crystal structures of all IBS systems are tetragonal at room temperature [21–26], i.e. lattice constant a = b. When cooled to a certain temperature, most of the parent compounds in the 1111, 122, and 111 classes undergo a first-order tetragonal-to-orthorhombic structural transition, normally followed by a transition from non-magnetic ordering to AFM magnetic ordering at the same or a lower temperature. For $Fe_{1+x}Te$, the system distorts to a monoclinic structure below structural transition temperature T_s. The AFM Néel temperature T_N is identical to T_s in the 11 system. Table 4 presents the structural information from selected parent compounds of each type, including the tetragonal phase at higher temperatures and the orthorhombic/monoclinic phase at lower temperatures. Several facts about the crystal structures of these IBS systems are noted below:

(1) Although the lattice constant along the c-axis in the 122 system is almost twice of that in the 111 and 11 systems, the iron interlayer distance is still similar in all three systems.

(2) The lattice constants a and b are very close in the orthorhombic/monoclinic case, which means that the lattice distortion is very subtle. If we consider only iron atoms, the in-plane iron-iron distances are also similar in all systems, including the 245.

(3) As mentioned in (1), the 122 system has a double iron layer in one unit cell. In cuprate systems like YBCO, the double layer creates two different inter-layer distances, creating an acoustic and an optical branch along the c-direction in their spin wave. In the case of 122, the iron layers are at 0.25 c and 0.75 c, making the two

inter-layer distances exactly the same. There is therefore only one acoustic branch of the spin wave in the 122 system, and the spin dynamics of the 122 and 111 systems are similar [27].

Table 1.2: Structural information of IBS parent compounds

Name	Type	Temperature	a($\AA$)	b($\AA$)	c($\AA$)	Symmetry	Ref.
LaFeOAs	1111	5K	5.7099	5.6820	8.7265	Orthorhombic	[28–32]
LaFeOAs	1111	175K	4.0301	=a	8.7368	Tetragonal	
$BaFe_2As_2$	122	5K	5.61587	5.57125	12.9428	Orthorhombic	[33–35]
$BaFe_2As_2$	122	175K	3.957	=a	12.9685	Tetragonal	
LiFeAs	111	215K	3.7914	=a	6.3639	Tetragonal	[24, 25]
$Fe_{1.068}Te$	11	5K	3.83435	3.78407	6.2571	Monoclinic	[26, 36–39]
$Fe_{1.068}Te$	11	80K	3.81234	=a	6.2517	Tetragonal	

Much effort has been devoted to finding the correlation between structural parameters and T_c. Physicists noticed early on that the 1111 system had a longer inter-layer distance than the other systems. Since the 1111 system has a somewhat higher T_c than other systems (such compounds as $NdFeAsO_{0.89}F_{0.11}$ and $GdFeAsO_{0.85}$ exceed 50K), it was suggested that the interlayer distance might be correlated to T_c. At this point, the attempts to increase the interlayer distance did not result in higher T_c. After that, it was found that the As-Fe-As bond angle showed a strong correlation to T_c. It was then pointed out that the height of the Fe-As block might control T_c as well. Since the Fe-As block height and As-Fe-As angle are related parameters, there is no clear evidence to support one of them over the other. Although the experimental data display convincing correlations between T_c and these parameters, it is fairly obvious that T_c is also affected by non-structure factors such as carrier doping.

Magnetic Structure

Most IBS parent compounds have AFM-ordered ground states. The 1111, 122, and 111 types have identical collinear magnetic structures, and different ordered

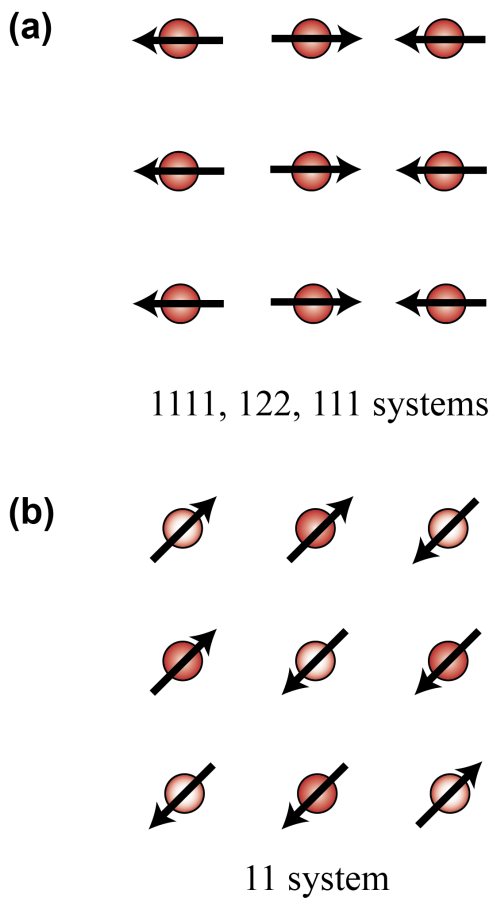

Figure 1.5: (a) shows the magnetic stucture of 1111, 122, 111 systems, and (b) shows the magnetic structure of 11 system.

moments. In the parent compounds of 122 and 11, the structure transitions are accompanied by magnetic transition. In doped 122 and most of the 1111 systems, the magnetic transition temperatures are close to, but lower than, the structural-transition temperatures. The proximity of the structural and magnetic transitions indicates the coupling between lattice and spins. The crystal distortion is thought to be driven by magnetisms, because lower symmetry allows the spins to order and thus relieve magnetic frustrations [40]. Orbital ordering is thought to be the other driving force, but there is no experimental evidence to support either picture.

The magnetic structures in each system are displayed in figure 1.5. For simplicity,

only iron atoms are shown. In the 1111 system, the rare-earth site also has FM/AFM ordering, but no evidence shows their correlation with superconductivity [41–44]. Along the c-axes, the systems in figure 1.5(a) (1111, 122, 111) are anti-ferromagnetically ordered, so only the in-plan magnetic structures are shown. The magnetic order at two iron sites are shown for the 11 system (fig. 1.5(b)).

Notations and Reciprocal Space

Both crystal structure and magnetic ordering create Bragg peaks in reciprocal space. As mentioned above, the system undergoes a very subtle structural transition that breaks the C4 rotational symmetry. Since the unit cell also changes on account of the broken symmetry, it is important to clarify the notation (coordinate system) in both real space and reciprocal space. The two-dimensional unit cell is shown in figure 1.6(a) under tetragonal notation and orthorhombic notation. Figure 1.6(b) shows the magnetic Bragg peak at L = 1, under both notations. In most cases, the choice of notation depends on the symmetry of the crystal structure. For example, the wave vector of the magnetic Bragg peak is usually written as $Q = (1, 0)_{Orthorhombic}$, because the magnetic Bragg peak exists only in the orthorhombic phase; in superconducting samples, neutron spin resonance at the same wave vector is usually written as $Q = (0.5, 0.5)_{Tetragonal}$, because the superconducting phase exists mostly under tetragonal symmetry. Sometimes only one of the notations is used to avoid confusion; for example, in chapter 4, the orthorhombic notation is used to make it easier to compare the 245 system with the 122 system.

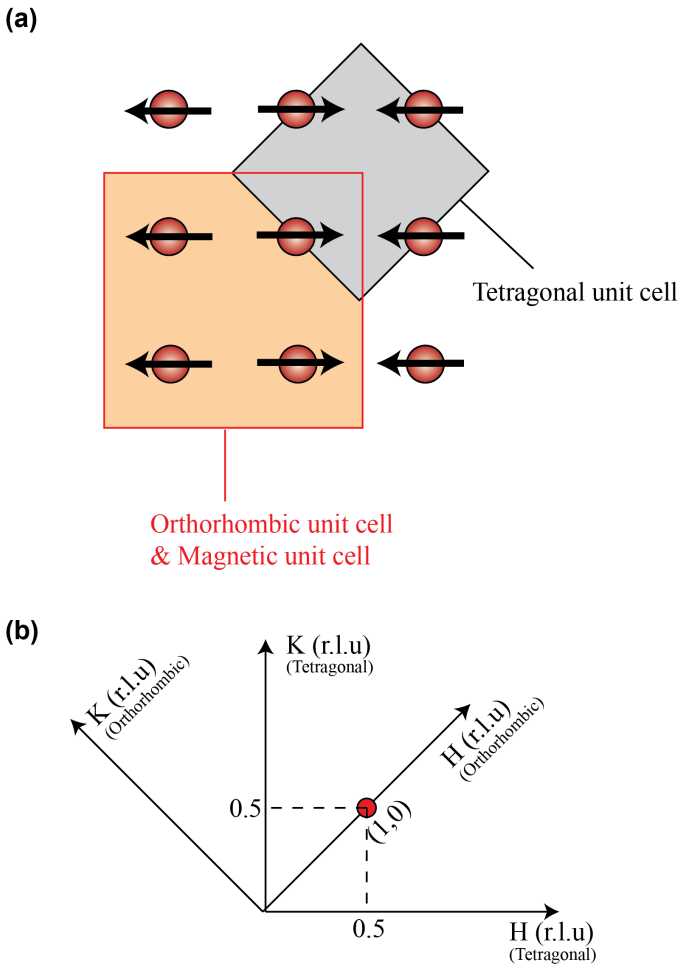

Figure 1.6: (a) The tetragonal unit cell above T_N and the orthorhombic unit cell below T_N. The magnetic unit cell is identical to the orthorhombic unit cell in 122 systems, while the c-axis doubled in 1111 and 111 system when entering the orthorhombic state. (b) Magnetic Bragg peak in reciprocal space under tetragonal [Q = (0.5,0.5)] and orthorhombic notation [Q = (1,0)].

1.2.4 Phase diagrams of IBS

Evolution of transition temperatures

Since the AFM order is found in both cuprates and IBS, we would expect the two systems to have similar phase diagrams. Early studies in $LaFeAsO_{0.92}F_{0.08}$ showed the absence of the AFM order in optimally doped samples [45], which has been confirmed

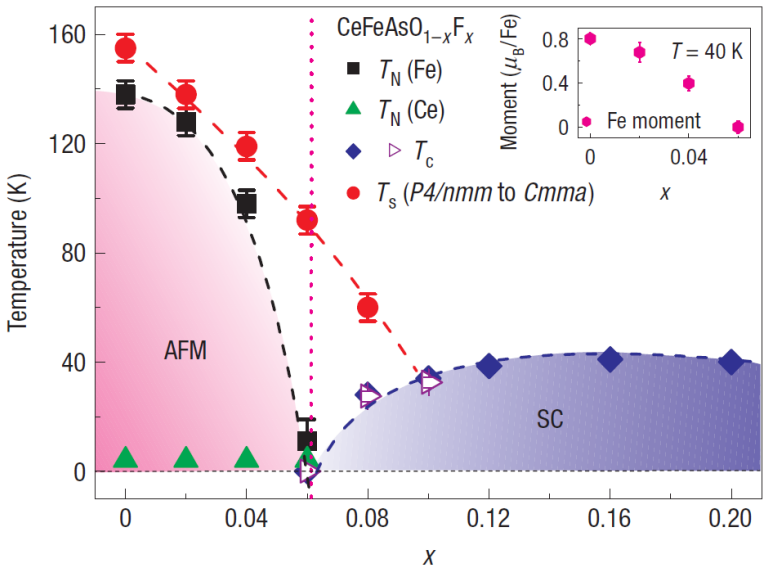

Figure 1.7: Phase diagram of $CeFeAsO_{1-x}F_x$ (Ref. [46]).

in most IBS systems. Figure 1.7 shows the phase diagram of $CeFeAsO_{1-x}F_x$ measured by neutron powder diffraction from Ref. [46]. In $CeFeAsO_{1-x}F_x$, both structural and magnetic transition temperatures decrease rapidly with electron doping, with an enlarged difference between T_N and T_s. Near the doping level where both transitions vanish, the superconducting phase appears. With more doping, the T_c reaches its highest point and then gradually decreases. The doping dependence of the 122 and 111 systems have similar features.

The suppression of the AFM order and the value of optimal T_c depends on many factors, one of the most important of which is the type of the doped element. IBS systems can be electron-doped, hole-doped or isovalent-doped. Unlike cuprates, in which the impurity in the copper-oxide layer would dramatically suppress superconductivity, atoms in the Fe-As layer can be partially or entirely substituted. Doping on the Fe-As layers can be either electron (Co, Ni on Fe) or isovalent (Ru on Fe, P on As), but attempts to hole-dope the iron site with, for example, Mn, do not result in superconductivity. Doping on buffer layers (out of the Fe-As planar) also generates superconductivity in the 1111 and 122 systems, including doping F on

the O site, doping P on the As site in 1111, and doping K/La on the Ba site in 122. Interestingly, the hole-doped systems have higher optimal T_c (∼40 K) overall than electron/isovalent doped systems (∼20K), which are also similar to cuprates, whose hole-doped systems have higher T_c (100K), while electron-doped systems have much lower T_c (∼20K).

Evolution of crystal and magnetic structures in 122 system

Here we select $BaFe_{2-x}Ni_xAs_2$ as an example to discuss the doping dependence of crystal and magnetic structures. The phase diagram of $BaFe_{2-x}Ni_xAs_2$ is shown in figure 1.8(a). Like the structure transition temperature, the orthorhombic lattice distortion and magnetic ordered moment decrease with doping. The order parameter of orthorhombic lattice distortion is defined as

$$\sigma = (a - b)/(a + b)$$

In the $BaFe_{2-x}Ni_xAs_2$ system, the SC phase appears before the complete suppression of the AFM phase. In lightly doped samples, the suppression of lattice distortion and ordered magnetic moment at base temperature is observed without any unusual features. Of the under-doped regime in which SC and AFM coexist in one sample, considering the competing nature of SC and AFM phase, it would be interesting to ask two questions: (1) whether there is any chemical separation between the two phases, and (2) how these two phases interact with each other in the same sample. These questions were answered by the early measurement in $BaFe_{2-x}Co_xAs_2$ [47, 48], which we then confirmed in $BaFe_{2-x}Ni_xAs_2$ [49](figure 1.8(b)). (This work is presented in chapter 3.1) In these measurements, the magnetic moment appears below T_N and increases as temperature decreases, as was expected. When cooled below T_c, the static moment began to drop, creating a kink at T_c. The observation of both T_N and T_c in the same AFM-order parameter rules out chemical separation of the two phases. Whether the SC and AFM phase are truly microscopically coexistent is still under

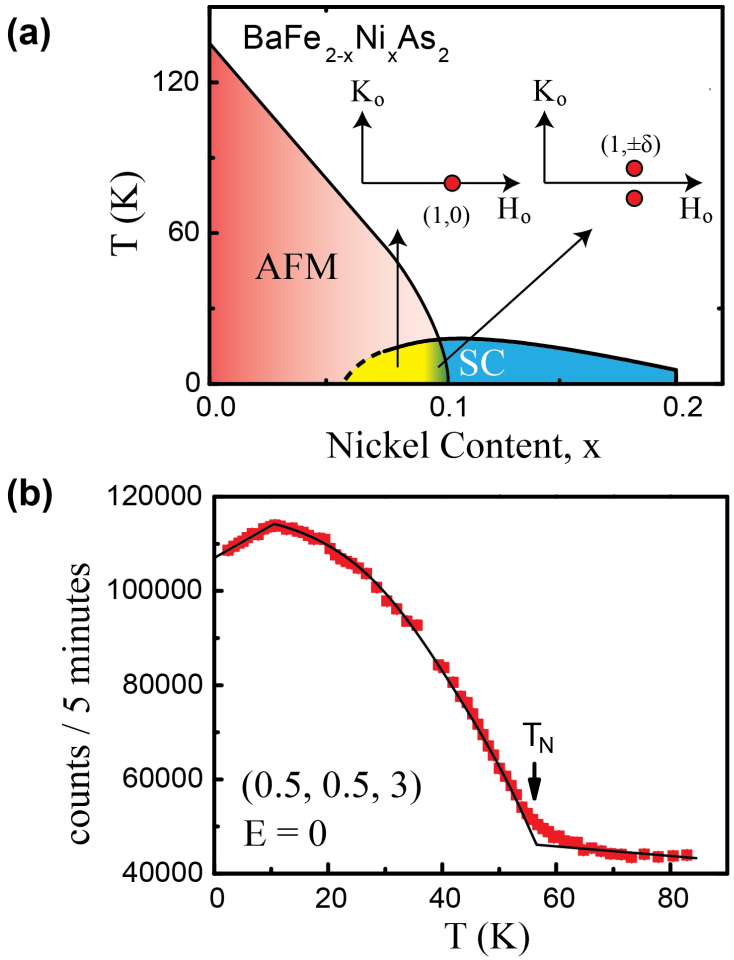

Figure 1.8: (a) Phase diagram of Ni-doped $BaFe_2As_2$ [49, 52]. In under-doped regime, superconductivity co-exists with short-range commensurate AF order (lower-left panel) and then gradually evolve to short-range incommensurage peaks at Q = (1$\pm\sigma$). (b) AF order parameter in under-doped $BaFe_{1.925}Ni_{0.075}As_2$.

debate, and this topic will also be discussed in chapter 3.2. The lattice distortion order parameter was found to behave similarly [50, 51]. Below T_c, lattice constants a and b begin to merge rather than separate, and reapproach the tetragonal phase as temperature decreases. The coupling between orthorhombicity and superconductivity is considered to be indirect, and to arise by megnetoelastic coupling.

Approaching the optimally-doped regime, both the structure distortion and magnetic

Bragg peak intensity become weak. Thanks to the large crystal size of the $BaFe_2As_2$ materials, the crystal and magnetic structure behavior of this regime can be carefully measured. Surprisingly, the long-ranged, commensurate AFM order was found to be replaced by the short-ranged, incommensurate AFM order, which begins to appear from Ni = 0.092 [52] and Co=0.13 [53]. Experimentally, this is characterized by the broadening of the full-width-half-maximum (FWHM) of magnetic Bragg peak and the splitting from Q = $(1, 0)_o$ to Q = $(1\pm\sigma, 0)_o$ of the peak center in reciprocal space (figure 1.8(a)). So far, it is still unclear whether the incommensurability is generated by itinerant features (mismatch of electron-hole pockets) or by local features (spin stripe order).

Evolution of spin excitations in 122 system

The experimental facts in both IBS and cuprates indicated that magnetism is intimately related to unconventional superconductivity. Neutron scattering, an excellent probe for measuring magnetic properties, has provided systematic measurements on the evolution of magnetic excitations in iron-based superconductors.

Although long-range AFM orders have been observed in IBS parent compounds, their magnetic excitations may differ from the spin waves in cuprates. In cuprates, the spin waves of parent compounds can be fitted perfectly with a local Heisenberg model, with the nearest exchange coupling J_1 and the next nearest J_2 (figure 1.9(a)). The observed J_1 is about 10 times greater than J_2, supporting the local picture of Mott-insulators. In IBS systems, the AFM order is thought to originate from electron-hole pocket excitations. Considering the itinerant nature of IBS, the magnetic excitations may differ in several respects from those in cuprates: (1) a damped signal may be observed, (2) isotropic exchange coupling along a and b directions may be needed, given the orthorhombic structure, and (3) the next next next nearest neighbour exchange coupling may be needed. In our previous work on $CaFe_2As_2$, we successfully used a local Heisenberg model to fit the observed spin wave with the damped

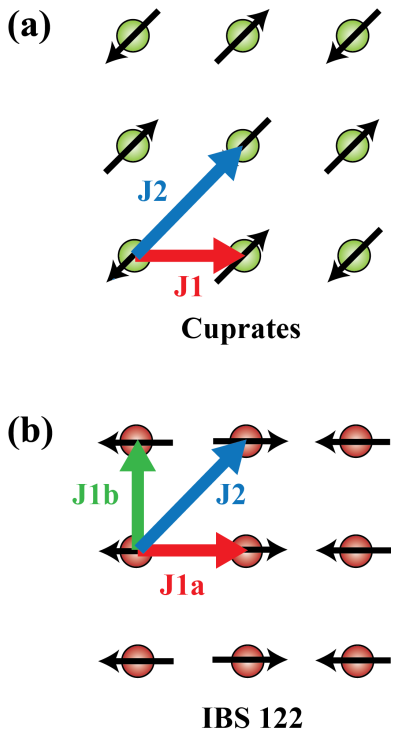

Figure 1.9: The exchange coupling of local Heisenberg model in cuprates and pnictides. (a) In cuprates, the nearest neighbour exchange coupling J_1 and the next nearest neighbour exchange coupling J_2 are used in the Heisenberg Hamiltonian. The fitted result shows that the J_1 is $\sim$10 times larger than J_2. (b) The exchange coupling used in $CaFe_2As_2$ and $BaFe_2As_2$ [54, 55]. Given the broken C4 symmetry, the nearest neighbour exchange coupling J_{1a} and J_{1b} is used, together with J_2. The fitted result shows that J_{1a}, J_{1b} and J_2 are comparable.

features [54]. It was found that, rather than isotropic exchange coupling J_1 and J_2, the anisotropic exchange coupling J_{1a} and J_{1b} was needed to describe the dispersion and local susceptibility (figure 1.9(b)). In the parent compound $Fe_{1.05}Te$, the next next nearest neighbour J_3 is found to be necessary [56]. Further investigation revealed that the excitation patterns in different IBS systems were quite different. Figure 1.10 summarizes the different typical low-energy excitation patterns in the $CaFe_2As_2$ [54], $BaFe_2As_2$ [55], $Fe_{1.05}Te$ [56] and $Rb_{0.78}Fe_{1.58}Se_2$ parent compounds [57]. All the above systems were fitted by a modified local Heisenberg model. On the other hand, high-energy excitation was discovered to remaine in optimally doped $BaFe_{1.9}Ni_{0.1}As_2$ [58]

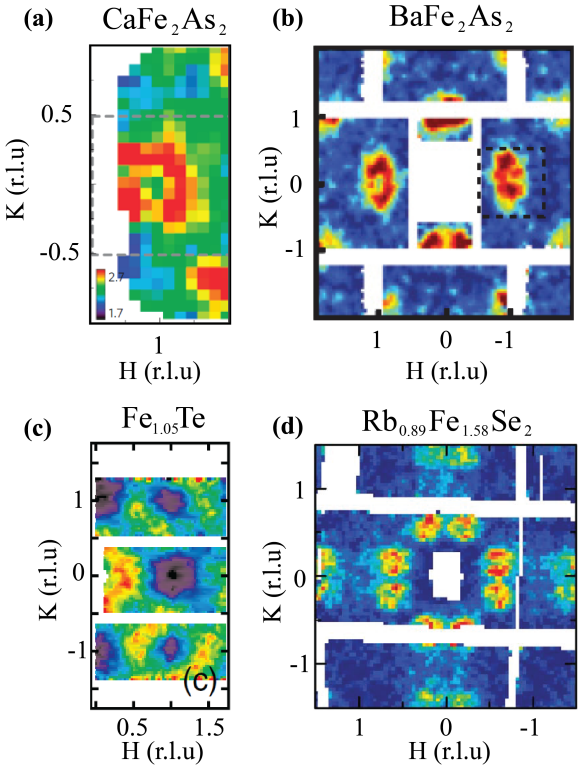

Figure 1.10: Selected magnetic excitation in $CaFe_2As_2$ [54], $BaFe_2As_2$ [55], $Fe_{1.05}Te$ [56] and $Rb_{0.78}Fe_{1.58}Se_2$ [59]. The $CaFe_2As_2$ was measured at MAPS time-of-flight spectroscopy, and the other samples were measured at ARCS time-of-flight spectroscopy. The measured spin wave is in [H,K] scattering plan at energies (a) E = 115±10 meV (b) E = 81±10 meV (c) E = 37±3 meV (d) E = 30±2 meV.

with unchanged intensity. These facts strongly suggest that, although IBS are more than purely itinerant systems. The local interactions play an essential role and may be important to superconductivity.

The evolution of spin excitation with electron- or hole-doping has been studied systematically in the Ba-122 system. In parent compound $BaFe_2As_2$, the pattern fits to a similar model as that of $CaFe_2As_2$ with a modified Q-dependent damping [55]. The low-energy excitation is found at $(\pm 1,0)$ $(0, \pm 1)_{Orthorhombic}$, and gradually disperses along transversal directions, reaching zone boundary $(1,1)_o$ at around 200 meV. When doped with electrons, the high-energy excitation merely changes, while

the low-energy excitation damps out near the under-doped regime, and disappears in the over-doped regime [58, 60]. In hole-doped $Ba_{1-x}K_xFe_2As_2$, the magnetic excitations evolve differently. In optimally doped $Ba_{0.7}K_{0.3}Fe_2As_2$, the low-energy excitation first elongates longitudinally below resonance energy, then begins to disperse transversally as that in the electron-doped case [60]. At higher energy, it disperses up to more than 100 meV along transversal direction, but the intensity of high-energy excitation was strongly suppressed. Such behavior is similar to the hour-glass excitation in hole-doped cuprates. In heavily doped KFe_2As_2, the high-energy excitation completely disappears, and low-energy excitation further evolves into two incommensurate peaks along the longitudinal direction [60](figure 1.10).

1.2.5 The introduction to alkali iron selenide (245) system

The first alkali iron selenide (245) system $K_yFe_{1.6+x}Se_2$ [19] was discovered in late 2010 with $T_c = 33$ K. More superconductors were discovered with almost the same T_c when K was replaced with other alkali metals (Rb, Cs) or alkali metals were partially substituted with Tl [61–64]. As the newest member of IBS family, the alkali iron selenides has certain novel properties that make it different from all other IBS systems.

Crystal and magnetic structure

Readers may have noticed that the chemical ratio of the 245 system is also written as 0.8:1.6:2. This is based on the fact that the 245 materials are isostructural with 122 when the alkaline earth metals (Ca, Sr, Ba) are replaced with alkali metals (K, Rb, Cs), and arsenic is replaced with selenium. Both the alkaline earth metal site and the iron site are partially occupied. The alkaline earth metal occupancy does not have any ordered structure or magnetic moment, while the vacancies on the iron site are long-range-ordered. The $\sqrt{5} \times \sqrt{5}$ order also generates a special structured magnetic

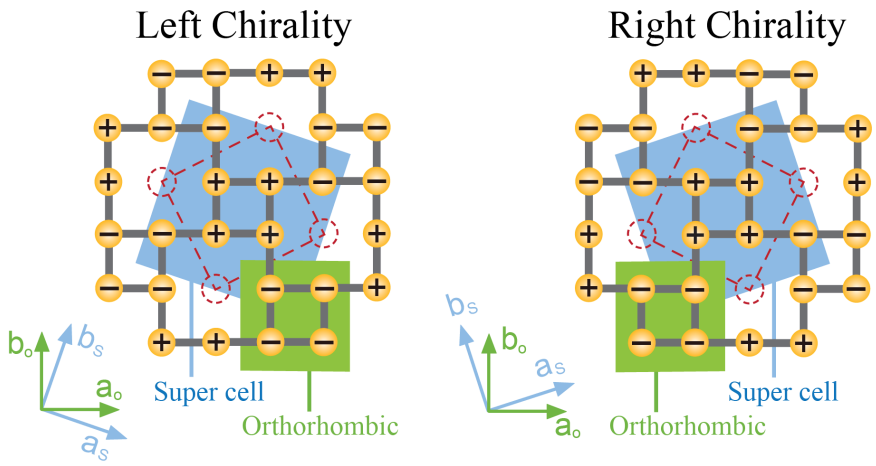

Figure 1.11: Crystal and magnetic structure of $A_{0.8-y}Fe_{1.6+x}Se_2$. The crystal unit cell is marked with a dark red dash, and the blue square represents the magnetic unit cell. To compare it with the other systems, the orthorhombic unit cell of the 122 systems is marked with a green square. The left and right panels are two chiralities equally distributed in the sample.

order at base temperature. Figure 1.11 shows the crystal structure and corresponding magnetic order in $K_{0.8-y}Fe_{1.6+x}Se_2$ [65, 66]. Despite the strange crystal and magnetic structure, the 245 systems (1) have a huge moment of $\sim 3.0 - 3.4\mu B$, which is the highest moment among all IBS systems; (2) have a Néel temperature of more than 550 K, much higher than typical IBS Néel temperatures (< 200K), and similar to those in cuprates; and (3) in the small samples, are insulators. All of the above features give a local picture of the 245 systems.

Phase diagram and arguments

The most controversial aspect of the 245 system is the phase diagrams. It is widely known that superconductivity arises when iron content is increased. Despite a gradually increasing T_c, however, the T_cs in the 245 systems, if they exist, are always about 33K. Moreover, the AFM Néel temperature remains almost the same throughout the phase diagrams (Figure 1.12) [67]. Normally this is a strong indication

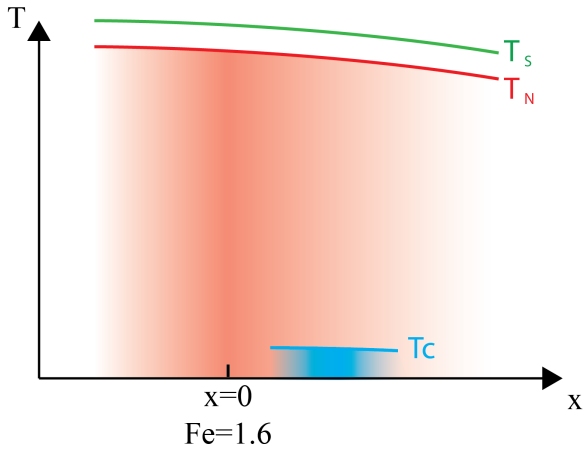

Figure 1.12: A schematic of the phase diagram of the 245 system. So far, different groups have plotted different phase diagrams, mostly because the iron content in the sample cannot be determined accurately. In general, samples with more iron content are more likely to be superconducting. As shown in the figure, the T_c appears suddenly with no gradual increase, and the long-range magnetic order remains almost the same.

of severe chemical separation. The real iron content that generates superconductivity is different in different research, and neutron scattering experiments have shown several minor phases besides the main 245 phase. Although many studies have been done on this sample, it remains unclear whether the doped 245 phase is responsible for superconductivity.

In this dissertation, the author's work on this system is introduced. The spin excitation of the parent compound was measured at base temperature and above T_N. Although the origin of the superconductivity in this sample has not yet been found, the 245 phase has been found to be truly local, and the electron-electron correlation in the sample to be weak, which differs from both strong-correlated Mott-insulators (cuprates) and itinerant SDW semiconductors (other IBS). This information may provide some clue as to whether the 245 phase is the real parent phase that evolves into a superconductor via doping.

1.3 Scope of the thesis

In this dissertation, we present the experimental data from five IBS samples in two different categories: three samples from the well-studied 122 system $BaFe_{2-x}Ni_xAs_2$, and two samples from the newly discovered 245 system $Rb_{0.8-y}Fe_{1.6+x}Se_2$. The measurements focus primarily on the spin dynamics and their relationship to superconductivity. The interplay between the long-range AFM order and superconductivity is also discussed. The ultimate goal of these measurements is to reveal the microscopic mechanisms of iron-based superconductors.

Chapter 2 discusses the experimental techniques used in this work. The techniques include two parts: crystal growth technique and neutron scattering techniques. In the section on crystal growth, flux method is used in the growth of $Ba(Fe,Ni)_2As_2$. In the neutron scattering techniques section, scattering principles and neutron scattering instruments are introduced.

In chapter 3, a series of studies conducted by the author on one of the most-studied IBS systems, $Ba(Fe,Ni)_2As_2$, is introduced. The chapter first focuses on the under-doped samples, since they are in the special regime of the phase diagram in which the AFM order and superconductivity co-exist. The co-existence is reflected by the suppression of the AFM ordered moment when system is cooled below T_c. With a magnetic field, the interplay between these two ground states has been probed through both magnetic Bragg peaks and magnetic excitations. We then study the magnetic excitation of the over-doped sample. Given the investigation's result throughout the phase diagrams, the evolution of the spin excitation upon doping will be discussed.

Chapter 4 will introduce the author ı́s work on the $A_{0.8-y}Fe_{1.6+x}Se_2$ (A=K,Rb,Cs) systems, which was discovered in late 2010. Although the $A_{0.8-y}Fe_{1.6+x}Se_2$ has a T_c of 30K and is isostructural with 122 pnictides, they have unique AFM order and phase diagram. We first measured the spin waves in non-superconducting $Rb_{0.89}Fe_{1.58}Se_2$ at base temperature, and fit them to a local exchange-coupling Heisenberg model. This is the first work to measure the spin wave of this material over the whole spectrum.

We have also carried out two follow-up works investigating the magnetic excitations in paramagnetic and SC states. In the first follow-up work, we measured the change of the spin waves when the non-superconducting sample was at the temperature $T_N \langle T \langle T_S$, and then at temperature $T \rangle T_S$. In the second follow-up work, we measured the magnetic excit of superconducting $Rb_{0.82}Fe_{1.68}Se_2$.

Chapter 5 is the last chapter of this dissertation, in which the work will be summarized and the future prospects discussed.

Chapter 2

Experimental Techniques

2.1 Preparation of single crystal

The samples used in this thesis were grown by the self-flux method in Dr. Pengcheng Dai's group at the Institute of Physics (IOP), Beijing, China [68, 69]. The self-flux method is used to grow samples of most iron-based superconductors. In the self-flux method, the components of the desired compound are dissolved in a liquid solvent. Given the nature of the target compound and the solvent, the temperature of the dissolution process is normally high, ranging from hundreds to more than one thousand °C. For the self-flux method, the element in solvent also exists in the final product, so it avoids contamination by not introducing any new elements into the growth process. The process of growing IBS crystals with the self-flux method involves the following steps:

(1) Preparing the starting materials
(2) Mixing the starting materials properly and loading them into a suitable container
(3) Vacuuming and sealing the container
(4) Heating the sealed sample by a specific procedure
(5) Opening the container and separating the single crystal from the flux.

In the growth of $BaFe_{1-x}Ni_xAs_2$, Fe-As is chosen as the flux. Fe and As powder in a mole ratio of 1:1 were used as the flux starting material. The starting material was then sintered in a quartz tube at 850 °C for 20 hours. After sintering, Barium was mixed with the resultant Fe-As power in one container, in a mole ratio of 1:N, where N ranges from 2 to 4. The sealing of the starting material was sketched in figure 2.1. To survive high temperatures, a ceramic container with a ceramic cap is used to directly hold the mixture. The ceramic tube was then placed inside the quartz tube, which was vacuumed and sealed to isolate the sample from air. The purpose of the sealing was to avoid oxidation of the sample. The mixed powder, in its container, was heated to 1150-1250 °C for more than five hours, then lowered to 1050 °C at a

rate 3 °C/h. The furnace was then cooled to room temperature. The mole ratio and the heating temperature changed with doping and furnace conditions.

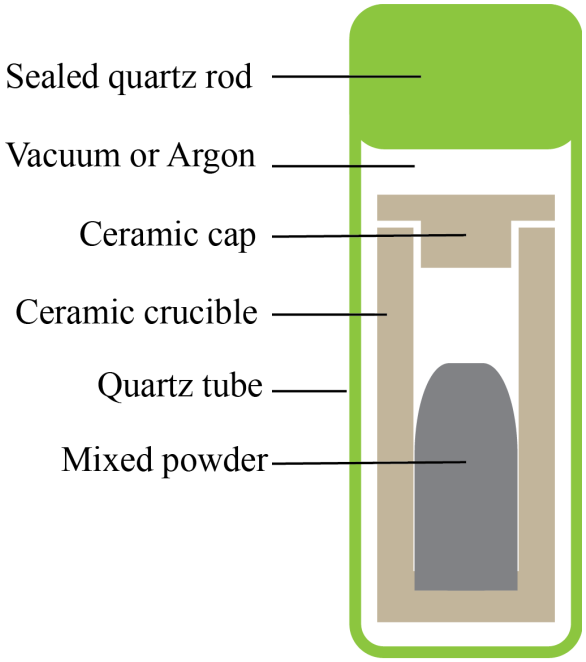

Figure 2.1: The container and sealing of the batch in the growth of $BaFe_{1-x}Ni_xAs_2$. The mixed powder (dark grey) together with its ceramic crucible (light grey) sealed in a quartz tube (green). Before sealing, the quartz tube was vacuumed or filled with argon gas to prevent contamination from oxygen or water.

2.2 Introduction to neutron scattering

2.2.1 A general introduction to neutron scattering

The scattering technique has been used to probe the properties of materials. Some of the neutron's properties are listed in table 2.1.

Table 2.1: Properties of the neutron

Mass	939.6 MeV/c^2
Charge	0
Spin	1/2
Magnetic Moment	1.04×10^3 μB

Compared to broadly used X-ray scattering techniques, neutron scattering techniques are normally more expensive, but they are very powerful in the measurement of magnetic materials thanks to the unique properties of neutrons: (1) zero charge, (2) 1/2 spin, and (3) dispersion.

Properties (1) and (2) determine how the neutrons interact with materials. The zero charge eliminates the coulomb interaction — one of strongest and most common interactions. The 1/2 spin makes the neutron an ideal probe for magnetic moments. In summary, the neutrons only interact with the nuclei and the magnetic moment; they do not interact with the electrons in the materials. The neutrons can therefore penetrate deep into the samples, making this technique ideal for bulk study. Property (3) gives neutron scattering technique an advantage over other probes used in condensed matter physics. The typical atomic spacing for crystals is $\sim$ 1 to 100 angstroms. In solids, the typical energy of the collective modes like phonons and spin waves ranges from $\sim$ 0.1 to 1000 meV. As a heavy particle (compared to photons and electrons), neutrons have dispersion of both wavelength and energy on the same order as the values listed above. This makes the inelastic neutron measurement an excellent choice for measuring the excitations in strong-correlated materials.

The properties listed above also have disadvantages. The weak interaction between the neutrons and the sample make a clean but very weak signal. Compared to experimental methods that can be performed with small samples, the sample mass is extremely important in neutron scattering experiments. The use of large samples creates certain problems as well, such as inhomogeneity or misalignment of domains/crystals. For high energy transfers (compared to E_i), the value difference between Q_i and Q_f makes it impossible to reach certain Q values, because of restrictions of geometry or limitations of instruments.

In neutron scattering experiments, samples are put into the neutron beam with a certain incident energy. In special cases, such as white beam measurement using time-of-flight spectrometers, the incident energy can have a distribution. In most cases, though, the incident energy is considered a fixed value, marked as E_i. After interacting with the sample, the scattered neutrons have energy E_f and an outgoing direction. Applying neutron dispersion and the direction of incoming/outgoing neutrons, the neutron momenta Q_i and Q_f can be determined. The energy transfer and momentum transfer can then be determined from momentum and energy conservation as shown below.

$$\vec{Q} = \vec{k}_f - \vec{k}_i$$
$$E = \mid E_f - E_i \mid = \frac{\hbar^2}{2m_n}(\vec{k}_f - \vec{k}_i)$$

2.2.2 Neutron cross sections

After interacting with the sample, the scattered neutrons will have an intensity distribution against the energy and angle. Using Fermi's golden rule, the distribution can be expressed as a differential scattering cross section [70, 71]:

$$\frac{d^2\sigma}{d\Omega_f E_f} = \frac{k_f}{k_i}\frac{m_n}{2\pi\hbar^2} \mid \langle \vec{k}_f\lambda_f \mid V \mid \vec{k}_i\lambda_i \rangle \mid^2 \delta(\hbar\omega + E_i - E_f)$$

The cross section is defined as the number of neutrons scattered per second into solid angle $d\Omega$ at θ,ρ with energy ranging from E_f to $E_f + dE_f$. Since the neutrons

have a weak interaction, it can be thought of as a perturbation, which is applicable to the Born approximation:

$$\langle \vec{k}_f \lambda_f \mid V \mid \vec{k}_i \lambda_i \rangle = \int d\vec{r} e^{i\vec{Q}\cdot\vec{r}_i} \langle \lambda_f \mid \sum_l e^{i\vec{Q}\cdot\vec{r}_i} \mid \lambda_i \rangle$$

As described in 2.2.1, neutrons only interact with nuclei or magnetic moments. For neutron-nuclei scattering, the interaction is short ranged given the size of the nuclei (∼1fm). The potential can then be characterized by scattering length b, with the form of

$$V\vec{Q} = \frac{m_n}{2\pi\hbar^2} b$$

which makes the cross section

$$\frac{d^2\sigma}{d\Omega_f E_f} = \frac{k_f}{k_i} \frac{m_n}{2\pi\hbar^2} \mid \langle \vec{k}_f \lambda_f \mid V \mid \vec{k}_i \lambda_i \rangle \mid^2 \delta(\hbar\omega + E_i - E_f)$$

In the case of elastic neutron scattering, the energy transfer is zero and only the signals from coherent cross sections are counted

$$\frac{d\sigma}{d\Omega} = N \frac{2\pi^2}{\nu_0} \sum_G \delta(\vec{Q} - \vec{G}) \mid F_N(\vec{G}) \mid^2$$

where F is the structure factor

$$F_N(\vec{G}) = \sum_j \vec{b}_j e^{i\vec{G}\vec{r}_j} e^{-W_j}$$

For inelastic scattering from structure (mostly phonon scattering), the cross section is

$$\frac{d^2\sigma}{d\Omega_f E_f} = \frac{k_f}{k_i} \frac{(2\pi)^3}{2\nu_0} \sum_{G,q} \delta(\vec{Q} - \vec{q} - \vec{G}) \sum_s \frac{1}{\omega_{qs}} [n_s(\omega) + 1] \delta(\omega - \omega_s) \mid F(\vec{Q}) \mid^2$$

where F corresponds to the dynamic structure factor

$$F_N(\vec{G}) = \sum_j \frac{\vec{b}_j}{\sqrt{m_j}} (\vec{Q} \cdot \vec{\xi}_j s) e^{i\vec{Q}\cdot\vec{d}_j} e^{-W_j}$$

2.2.3 Neutron instruments

The neutron scattering experiments in this dissertation were performed on triple-axis spectrometers (TAS) and neutron time-of-flight (TOF) spectrometers, the two classical spectrometers that use different types of neutron sources. Triple axis spectrometers use reactor-based neutron sources, which produce a white neutron beam continuously; time-of-flight spectrometers use accelerator-based neutron sources by which neutrons are chopped into a pulsing beam.

Figure 2.2 shows the schematic of the HB-3 triple axis spectrometer in the High Flux Isotope Reactor (HFIR) in the Oak Ridge National Laboratory (ORNL). Part of the work in chapter 3 was performed on this spectrometer. Since the incident beam has multiple energies, a single crystal is used to select a specific incident energy using Bragg′s law. This rotating single crystal is called a monochromator and is generally made of graphite, silicon, or copper. The scattered neutrons from the sample also have energy distribution, and another single crystal called an analyzer is used to define the neutron energy that is detected. The incident wave vector direction is controlled by rotating the sample and the scattered wave vector direction by rotating the arm that carries the analyzer and detector. The name "triple-axis" comes from the three rotating axes on the monochromator, sample, and analyzer.

Figure 2.3 shows the schematic of the Wide Angular-Range Chopper Spectrometers (ARCS) spectrometer at the Spallation Neutron Source (SNS) in ORNL. Two of the works in chapter 4 were performed on this spectrometer. The neutron sources of time-of-flight spectrometers are usually spallation neutron source, where the proton beam is used to bombard a heavy metal target to generate neutrons. By calculating the neutrons′ flight time over a certain distance, their energy is determined and a fermi chopper is used to define incident energy. The pulse nature of the neutron beam greatly aids the collection of scattered neutron signals because neutrons of all energies can be detected and determined by the time they take to arrive at the detectors. This means that detectors can be placed directly after the sample, and a

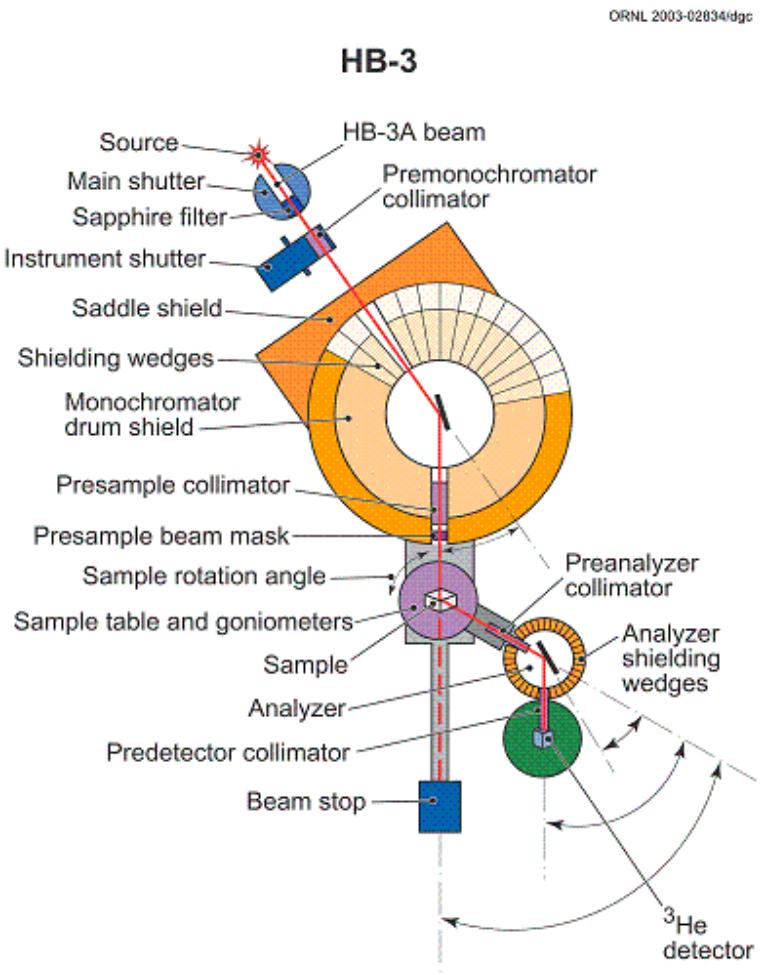

Figure 2.2: Schematic of HB-3 triple-axis spectrometer.

large-scale detector bank can be installed. The ARCS spectrometer has three detector banks measuring the angle range from -35 degrees to 135 degrees with an incident energy range from 20 meV to 1500 meV.

Both the TAS and the TOF spectrometers have advantages and drawbacks. The TAS, especially the cold neutron TAS, has relatively low incident energies, making it ideal for measuring low energy excitations ($\lesssim$50 meV) while the TOF is more suitable for measurement at higher energies. The wide energy/momentum coverage of the TOF makes it very powerful for mapping the excitation pattern, but less effective if the interested signal is near a certain wave vector. Chapter 3 focuses primarily on the magnetic resonances (¡20 meV) and how they change as temperature and magnetic

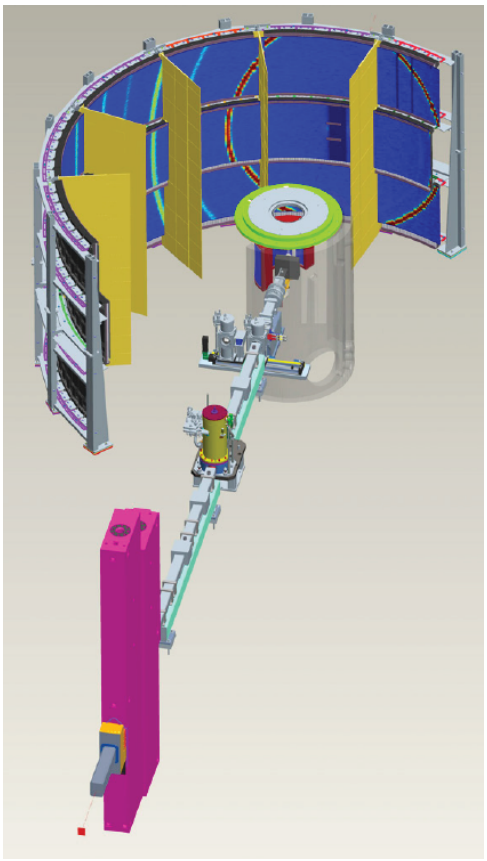

Figure 2.3: Schematic of ARCS time-of-flight spectroscopy.

field change, and the TAS is used for all of that chapter's experiments. In chapter 4, the TOS spectrometer is used to map the magnetic excitation of the entire Brillouin zone up to 300 meV.

Chapter 3

Research of electron-doped $\mathbf{BaFe_{2-x}Ni_xAs_2}$

3.1 Evolution of resonance mode in $BaFe_{2-x}Ni_xAs_2$

3.1.1 Introduction

Spin excitations have been postulated by several theories to play a crucial role in the electron pairing and superconductivity of these materials [72–76]. In one class of unconventional microscopic theories for superconductivity, electron pairing in iron arsenide superconductors is mediated by quasiparticle excitations between sign-reversed hole-like pockets around the Γ point and the electron-like Fermi pockets around the M point as shown in the inset of Figure 3.2(a) [77]. If this is indeed the case, spin excitations in the superconducting state should have a collective mode called the neutron spin resonance, whose energy is at or slightly less than the addition of the hole and electron superconducting gap energies: E=|δ(k+Q)+δ(k)|, where Q is the AF ordering wave vector connecting the hole and electron Fermi pockets at the Γ and M points, respectively [78–81].

Although early inelastic neutron scattering experiments have found the neutron spin resonance for different iron-based superconductors consistent with this picture [82–90], a surprising result has been that the mode in the optimally doped $BaFe_{1.9}Ni_{0.1}As_2$ (T_c = 20 K) has three-dimensional character as demonstrated by clear dispersion of the mode energy along the c-axis [82, 85]. These results are quite different from the two-dimensional nature of the resonance in copper oxide superconductors [13, 91–94]. If spin excitations are important for superconductivity in iron-arsenides, it would be interesting to systematically investigate the doping evolution of the resonance in $BaFe_{2-x}Ni_xAs_2$, and determine if the three-dimensional nature of the mode is a general phenomenon or specific only to the optimally doped materials. Furthermore, since spin waves in the AF-ordered parent compounds of (Ba,Sr,Ca)Fe_2As_2 have rather large anisotropy spin gaps at the AF zone center [95–100],whilespin excitations in the optimally electron-doped superconducting samples are generally gapless in the nonsuperconducting normal state [84, 89, 101, 102].It would be important to see how

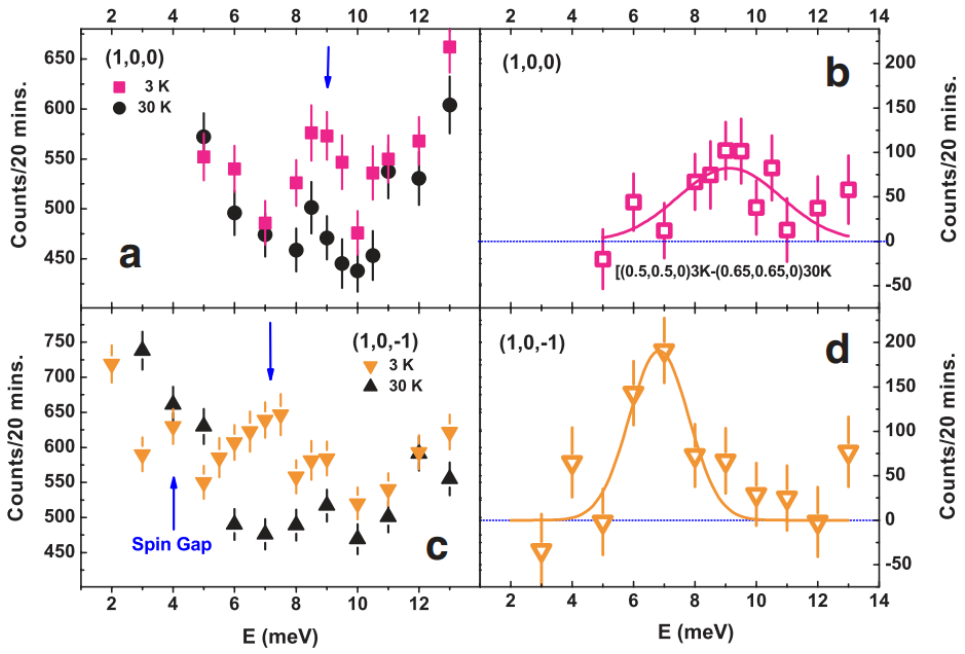

Figure 3.1: From Ref.[82]. The previous measurement in $BaFe_{1.9}Ni_{0.1}As_2$ showed neutron spin resonances energies at L = 0 and L = 1. (a)(c) Constant Q scan at Q = $(1,0,0)_o$ and Q = $(1,0,0)_o$. The black symbols are the neutron intensity above T_c, and the magenta/orange symbols are neutron intensity at the base temperature. (b)(d) shows the neutron spin resonance intensity by subtracting 30K data from 3K data.The resonance peaks at 7 meV when L = 0 and 5 meV when L = -1.

spin waves in the parent compounds evolve as electrons are doped into the FeAs planes.

This section presents inelastic neutron scattering studies of the low-energy spin excitations in electron-doped $BaFe_{2-x}Ni_xAs_2$ with $x = 0.075, 0.15$ [Fig. 3.2(a)]. In $BaFe_{1.925}Ni_{0.075}As_2$ [Fig. 3.2(a)], bulk superconductivity appears at $T_c = 12.3$ K [Fig. 3.2(b)] and the N*é*el temperature of the material is $T_N \sim 58$ K [Figs. 3.3(a) and 3.3(b)]. Our inelastic neutron scattering experiments show the presence of a three-dimensional neutron spin resonance with distinct energies at the AF wavevectors $Q = (0.5, 0.5, 0)$ and $(0.5, 0.5, 1)$, which is quite similar to that of the optimally doped $BaFe_{1.9}Ni_{0.1}As_2$ [101, 102]. The intensity gain of the mode below T_c is compensated by opening a pseudo (not complete) spin gap at lower energies and reduction in the

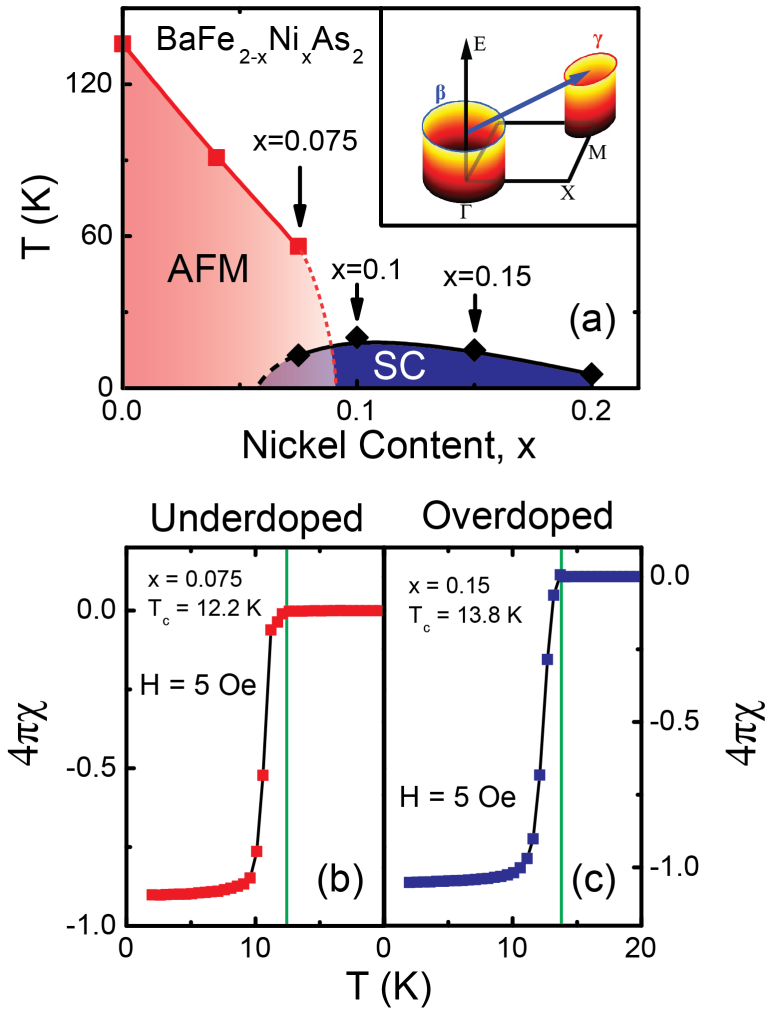

Figure 3.2: (a)The phase diagram of $BaFe_{2x}Ni_xAs_2$. The measured samples were marked on the phase diagram. The inset of panel (a) shows a schematic of electron-hole pocket excitation. (b)(c) Mangetic susceptilibity measurement of $BaFe_{1.925}Ni_{0.075}As_2$ and $BaFe_{1.85}Ni_{0.15}As_2$.

static AF order.

3.1.2 Experimental setups

We grew single crystals of $BaFe_{2-x}Ni_xAs_2$ with $x = 0.075, 0.15$ using the self-flux method [103]. Our neutron scattering experiments were carried out on the HB-3, HB-1 thermal triple-axis spectrometers at the high-flux-isotope reactor (HFIR), Oak Ridge National Laboratory [95]; the BT-7 thermal triple-axis spectrometer at the NIST Center for Neutron Research [102]; and the PANDA cold triple-axis spectrometer at the Forschungsneutronenquelle Heinz Maier-Leibnitz (FRM-II), TU München [101]. We defined the wave vector Q at (q_x, q_y, q_z) as $(H, K, L) = (q_x a/2\pi, q_y b/2\pi, q_z c/2\pi)$ reciprocal lattice units (rlu) using the tetragonal nuclear unit cell, where $a = 3.89$ Å, $b = 3.89$ Å, and $c = 12.77$ Å. We co-aligned about 6 grams for each of the $x = 0.075, 0.15$ samples of $BaFe_{2-x}Ni_xAs_2$ in the $[H, H, L]$ horizontal scattering plane (with mosaicity $\sim 3^\circ$ for each of the crystal assembly), and put our samples inside either a closed cycle refrigerator or a liquid He cryostat.

For thermal triple-axis measurements on HB-1, HB-3, and BT-7, we used pyrolytic graphite (PG) as monochromator and analyzer with typical collimations of open-40′-S-40′-120′. The final neutron energy was chosen to be either $E_f = 13.5$ meV or $E_f = 14.7$ meV with a PG filter before the analyzer. For cold triple-axis measurements on PANDA, we chose final neutron energy of $E_f = 5.0$ meV with a cooled Be filter in front of the analyzer. We used both horizontal and vertical focusing PG monochromator and analyzer with no collimators. We also used a $E_f = 13.5$ meV setup with a PG filter in one of the PANDA measurements. For $E_f = 5.0$ meV and $E_f = 13.5$ meV setups, the instrumental energy resolutions are about 0.5 meV and 1.2 meV, respectively.

3.1.3 AFM order parameter

We first describe our elastic and quasielastic neutron scattering results on the underdoped $BaFe_{1.925}Ni_{0.075}As_2$. Consistent with earlier results on underdoped $BaFe_{1.906}Co_{0.094}As_2$ [87] and $BaFe_{1.92}Co_{0.08}As_2$ [88]. The AF structure reported here,

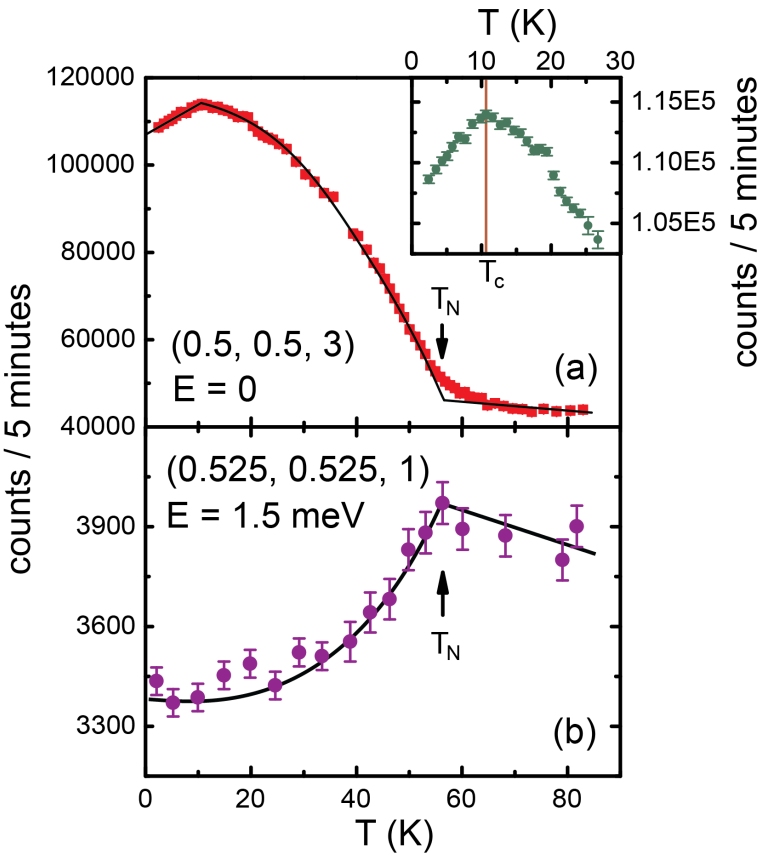

Figure 3.3: (a) Temperature dependence of the Q=(0.5, 0.5,3) magnetic Bragg peak in $BaFe_{1.925}Ni_{0.075}As2$, showing a clear anomaly at T_N and T_c. Inset shows an expanded view of the Q=(0.5, 0.5,3) magnetic Bragg peak near T_c. (b) Temperature dependence of the quasielastic scattering at E=1.5 meV and Q=(0.525,0.525,1) shows a clear anomaly at T_N=58 K.

$BaFe_{1.925}Ni_{0.075}As_2$ is identical to the undoped parent compound but with a Néel $T_N \approx 58$ K [Fig. 3.3(a)]. The temperature dependence of the quasielastic scattering at $Q = (0.525, 0.525, 1)$ and $E = 1.5$ meV shows a clear kink below ~ 58 K, thus confirming the Néel temperature of the system. The inset in Figure 3.3(b) shows the expanded temperature dependence of the AF Bragg peak intensity at $Q = (0.5, 0.5, 3)$. The scattering decreases with decreasing temperature at the onset of T_c, suggesting

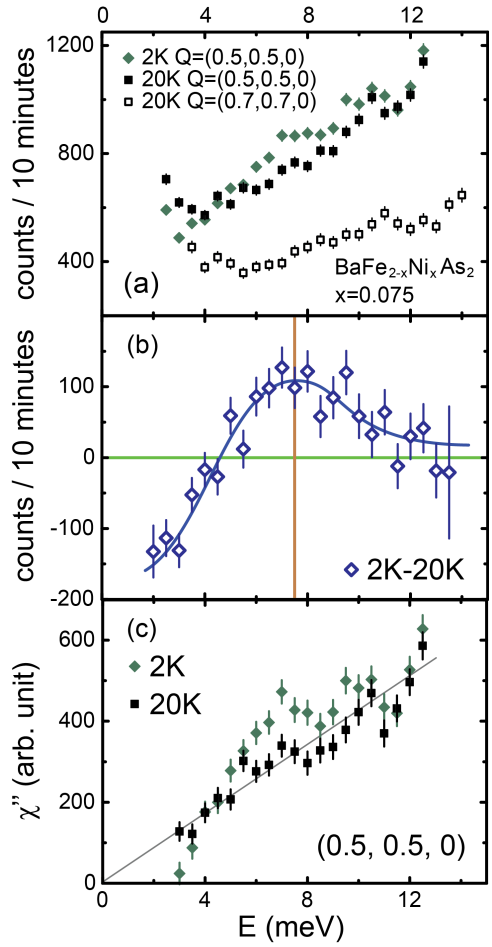

Figure 3.4: (a) Energy scans at Q=(0.5, 0.5,0) (signal) and Q=(0.7, 0.7,0) (background) positions above and below T_c for $BaFe_{1.925}Ni_{0.075}As_2$. (b) Temperature difference plot (2K - 20K) in $S(Q,\omega)$ shows a clear neutron spin resonance at E=7 meV below Tc. Solid line is a guide to the eye. (c) Estimation of the temperature dependence of $\chi"(Q,\omega)$ above and below Tc using the background determined both from constant-energy scans and from constant-Q scans at background position.

that the static moment competes with superconductivity similar to the Co-doped materials [87, 88].

3.1.4 Resonance mode in under-doped $BaFe_{1.925}Ni_{0.075}As_2$

To see if there is a neutron spin resonance mode in underdoped $BaFe_{1.925}Ni_{0.075}As_2$ and to compare its c-axis dispersion with optimally doped $BaFe_{1.9}Ni_{0.1}As_2$ [101], we carried out constant-Q scans at $Q = (0.5, 0.5, 0)$ and $(0.5, 0.5, 1)$ above and below the superconducting transition temperature T_c. Figure 3.4(a) shows the raw data collected on the HB-3 triple-axis spectrometer at the signal $Q = (0.5, 0.5, 0)$ and background $Q = (0.7, 0.7, 0)$ positions. There is clear intensity gain at $Q = (0.5, 0.5, 0)$ near $E = 7$ meV below T_c at the expense of spectral weight loss below $\sim$4 meV. The temperature difference spectrum between 2 K and 20 K in Fig. 3.4(b) confirms the presence of the mode at $E = 7$ meV below T_c and a reduction in spectral weight below 4 meV. The open squares in Fig. 3.4(a) show the energy dependence of the background scattering at $Q = (0.7, 0.7, 0)$.

Figure 3.4(c) shows our estimation of the energy dependence of the dynamic susceptibility $\chi''(Q, \omega)$ above and below T_c, obtained by subtracting the background and correcting for the Bose population factor using $\chi''(Q, \omega) = [1 - \exp(-\hbar\omega/k_B T)]S(Q, \omega)$, where $E = \hbar\omega$. While the normal state susceptibility appears to increase linearly with energy, superconductivity rearranges the spectrum, creating a (pseudo) spin gap below 4 meV (defined as a suppression of spin fluctuations) and a neutron spin resonance at $E = 7$ meV for in-phase spin fluctuations along the c-axis ($L = 0$).

To investigate the behavior for the out-of-phase spin fluctuations along the c-axis, we plot in Fig. 3.5(a) constant-Q scans at $Q = (0.5, 0.5, 1)$ above and below T_c. Figure 3.5(b) shows the temperature difference plot, and a comparison of Fig. 3.5(b) and Fig. 3.5(b) immediately reveals that the neutron spin resonance has moved from $E = 7$ meV at $Q = (0.5, 0.5, 0)$ to $E = 5$ meV at $Q = (0.5, 0.5, 1)$. Note in particular that for $Q = (0.5, 0.5, 0)$ there is essentially no change with temperature for the scattering at 5 meV (Fig. 3.4), which is where the maximum in intensity occurs at the $Q = (0.5, 0.5, 1)$ position. This is compelling evidence that the neutron spin

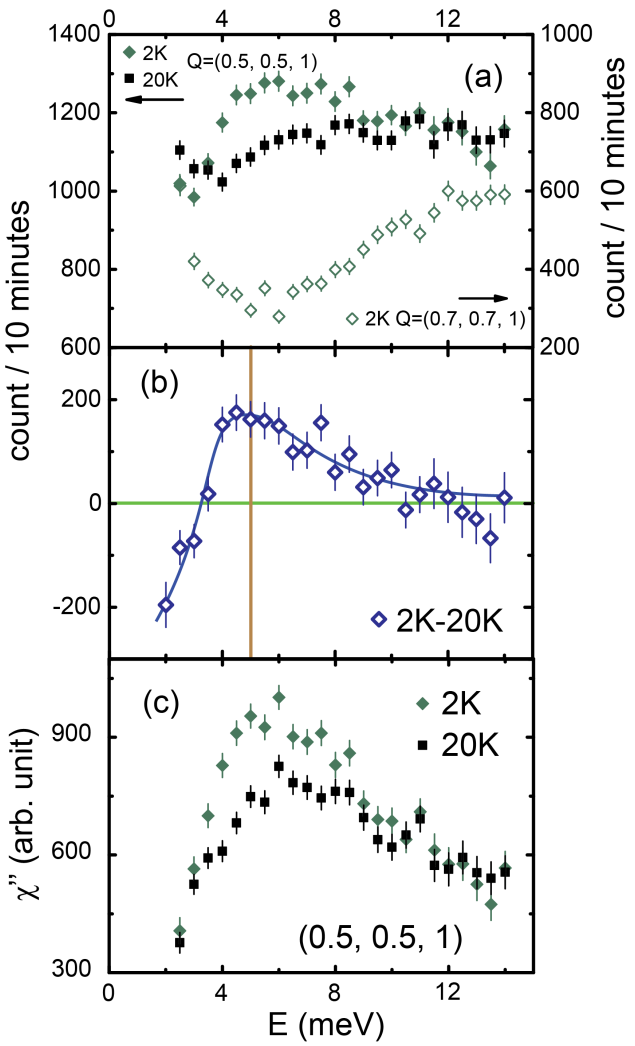

Figure 3.5: (a) Constant-Q scans at Q=(0.5, 0.5,1) above and below Tc for $BaFe_{1.925}Ni_{0.075}As_2$. The scattering shows clear asymmetric enhancement around E=5 meV below T_c. (b) Temperature difference plot reveals a neutron spin resonance at E=5 meV, clearly below the energy of the mode at Q=(0.5, 0.5,0) as shown in Fig. 2.

resonance is dispersive for both underdoped and optimally doped $BaFe_{2-x}Ni_xAs_2$. Figure 3.5(c) plots our estimated the energy dependence of $\chi''(Q,\omega)$ above and below T_c.

3.1.5 Resonance mode in $BaFe_{1.85}Ni_{0.15}As_2$

Having described our measurements on the underdoped $BaFe_{1.925}Ni_{0.075}As_2$, we now discuss inelastic neutron scattering experiments on the overdoped $BaFe_{1.85}Ni_{0.15}As_2$ [Fig. 3.2(c)], where the static AF order is completely suppressed. These measurements were carried out on the PANDA cold triple-axis spectrometer. Figure 3.6 summarizes the constant-Q scans at $Q = (0.5, 0.5, 0)$ and $(0.5, 0.5, 1)$ below and above T_c. Using $E_f = 5$ meV, we find in Figs. 3.6(b) and 3.6(d) that the neutron spin resonance occurs at $E = 6$ meV for $Q = (0.5, 0.5, 1)$. Since the effect of the Bose factor for temperatures between 4 K and 20 K is not so important for spin excitations with energies near 6 meV, the intensity gain at $Q = (0.5, 0.5, 1)$ below T_c in Fig. 3.6(d) must arise from the increased $\chi''(Q, \omega)$. Similar scans at $Q = (0.5, 0.5, 0)$ reveal clear scattering intensity enhancement above $E = 5$ meV [Figs. 3.6(a) and 3.6(c)]. However, kinematic constraints with the $E_f = 5$ meV spectrometer configuration did not allow a conclusive determination of the resonance energy. Figure 3.6(g) shows identical scans carried out with $E_f = 13.5$ meV. Inspection of Figs. 3.6(g) and 3.6(h) indicates that the resonance energy at $Q = (0.5, 0.5, 0)$ is now shifted to $E = 8$ meV. To estimate the spin gap values in the superconducting state of $BaFe_{1.85}Ni_{0.15}As_2$ at $Q = (0.5, 0.5, 0)$ and $(0.5, 0.5, 1)$, we plot in Figs. 3.6(e) and 3.6(f) $\chi''(Q, \omega)$ at temperatures above and below T_c, obtained by subtracting the backgrounds and correcting for the Bose population factor in Figs.3.6(a) and 3.6(b). Is is clear that spin excitation spectra have spin gaps in the superconducting state similar to previous work on optimally doped $BaFe_{1.85}Ni_{0.15}As_2$ [102].

3.1.6 Neutron spin resonance energy as a function of T_c

We summarize in Figure 3.7 the electron-doping dependence of the neutron spin resonance at $Q = (0.5, 0.5, 0)$ and $(0.5, 0.5, 1)$ as a function of T_c for both $BaFe_{2-x}Ni_xAs_2$ [101, 102, 104, 105] and $BaFe_{2-x}Co_xAs_2$ [84, 87–89]. For copper oxide high-T_c superconductors, one of the hallmarks of the resonance is that its

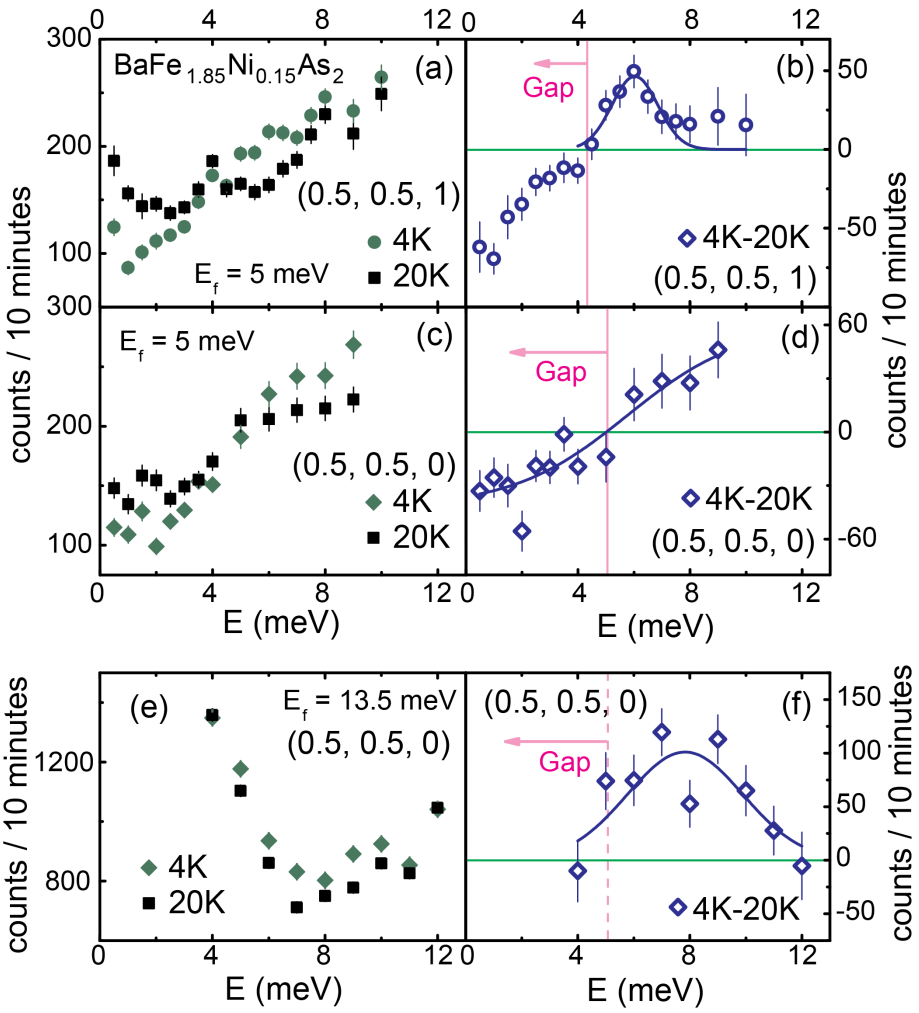

Figure 3.6: (a) Energy dependence of scattering at Q=(0.5, 0.5,0) above and below T_c. (b) Energy dependence of the scattering above and below T_c, now at Q=(0.5, 0.5,1). (c) Temperature difference plot between 4 and 20 K showing the intensity gain below Tc near E=8 meV. (d) Temperature difference data confirm the formation of the neutron spin resonance at E=6 meV. (e) Identical scan as that of (a) except we used E_f =13.5 meV. Superconductivity-induced neutron spin resonance can now be seen around E=8 meV. (f) Temperature difference plot confirms the presence of the resonance at E=8 meV.

energy is proportional to T_c over a very wide temperature range [13, 94]. Since $BaFe_{2-x}Ni_xAs_2$ has two resonances at distinctively different energies, its dispersion along the c-axis is related to the superconducting gap Δ_0 and its deviation δ via

$E(Q_z) \sim 2\Delta_0 - 2\delta\,|\sin(Q_z/2)|$ [101]. The observation of a linear relationship for both mode energies and T_c suggests that $\delta/\Delta_0 = [\omega(0.5, 0.5, 0) - \omega(0.5, 0.5, 1)]/\omega(0.5, 0.5, 0)$ is approximately 0.28 and weakly Ni-doping dependent. Therefore, the ratio of interplane ($J_\perp$) and intraplane ($J_\parallel$) AF coupling, $J_\perp/J_\parallel$, is weakly electron-doping dependent assuming that the values of Δ_0 and δ are proportional to $J_\parallel$ and $J_\perp$, respectively.

We now discuss the physical interpretation of the above results. In the theory of spin-fluctuation-mediated superconductivity [72–76], the electron pairing arises from sign-reversed S-wave interband scattering between hole pockets centered at the Γ point and electron pockets at the M points [inset in Fig. 3.2(a)] [79–81, 106]. One of the consequences of such electron-hole pocket excitations is to induce a resonance peak at the AF ordering wave vector $Q = (0.5, 0.5, 0)$ in the spin excitations spectrum. In the strictly two-dimensional model, the energy of the resonance is at (or slightly less than) the addition of hole (Δ_0^h) and electron (Δ_0^e) superconducting gap energies ($\Delta_0 = \Delta_0^h + \Delta_0^e$). Our previous finding of three-dimensionality of the resonance in optimally doped $BaFe_{1.9}Ni_{0.1}As_2$ [101, 102] suggests that the superconducting gap energy Δ_0 should be three-dimensional as well and sensitive on the Q values along the c-axis. The new results reported in the present paper on underdoped $BaFe_{1.925}Ni_{0.075}As_2$ and overdoped $BaFe_{1.85}Ni_{0.15}As_2$ confirm the earlier conclusion, and reveal that the three-dimensional nature of the superconducting gap is prevalent throughout the superconducting dome. If spin excitations are mediating the electron pairing for superconductivity, these results would suggest that the AF exchange coupling along the c-axis ($J_\perp$) contributes significantly to the electron pairing. Although the overall spin excitations as a function of increasing electron doping transform into quasi two-dimensional spin excitations rather rapidly as demonstrated by the disappearing anisotropic spin gaps at $Q = (0.5, 0.5, 0)$ and $(0.5, 0.5, 1)$ with increasing Ni-doping [104], the superconductivity-induced resonance retains its three-dimensional character even in the overdoped regime. This means that the superconducting electronic gaps

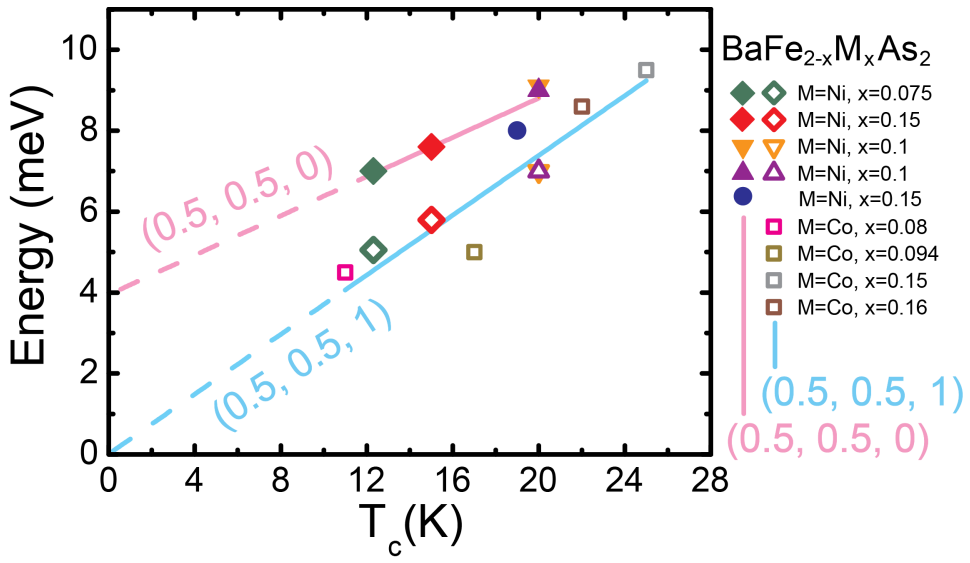

Figure 3.7: Summary of electron-doping dependence of the neutron spin resonance energies at Q=(0.5, 0.5,0) and (0.5,0.5,1) as a function of T_c.

in the iron-arsenic based materials are three-dimensional and quite different from that of the copper oxide superconductors.

3.1.7 Conclusions

In summary, we have determined the doping evolution of the low-energy spin excitations in $BaFe_{2-x}Ni_xAs_2$ for both underdoped and overdoped superconductors. In underdoped $BaFe_{1.925}Ni_{0.075}As_2$, we find that the appearance of bulk superconductivity is associated with the appearance of a weak three-dimensional neutron spin resonance. The spectral weight gain of the resonance below T_c is a rather small portion of the overall normal state magnetic scattering, and is compensated by reduction in static magnetic moment. Our Ni-doping dependent investigation of the spin gap and neutron spin resonance reveals that the three-dimensional nature of the mode found earlier for the optimally doped sample is a universal property of Ni-doped superconductors. These results in turn suggest that AF spin excitations between the layers are also important for the superconductivity of these materials.

3.2 Magnetic field effect in electron under-doped $BaFe_{1.92}Ni_{0.08}As_2$

3.2.1 Introduction

In the previous section, we observed that the occurrence of superconductivity in the under-doped regime is accompanied by a reduction in the static AF Bragg intensity and the appearance of a neutron spin resonance in the magnetic excitation spectra [87, 88, 107]. The coexistence of static AF order and superconductivity is believed to be compatible with electron pairing mediated by quasiparticle excitations between sign-reversed s-wave hole-like pockets around the Γ point and the electron-like Fermi pockets around the M point (s± pairing symmetry) [77–80, 108, 109]. In this pure itinerant picture, electrons that form the ordered moment also contribute to the superconducting condensation, and AF order and superconductivity thus coexist microscopically [108, 109]. If the static AF order in $BaFe_{2-x}(Co,Ni)_xAs_2$ also has local moment contributions [110, 111], the magnetically ordered phase can coexist more easily with superconductivity, but the ordered moment should not be affected by superconductivity [109].

One way to test the interplay between magnetism and superconductivity is to usethemagnetic field as a tuning parameter. If the static AF order in the underdoped $BaFe_{2-x}(Co,Ni)_xAs_2$ indeed coexists and competes with superconductivity [87, 88, 107, 112], application of a magnetic field that suppresses superconductivity should also enhance the static AF order, much like that of the electron-doped copper oxide superconductors [113, 114]. On the other hand, if the static AF order in $BaFe_{2-x}(Co,Ni)_xAs_2$ is chemically phase separated from the superconducting parts of the sample, application of a magnetic field should reduce the AF ordered moment, as has been found in chemically phase separated $Ba_{1-x}K_xFe_2As_2$ [115]. Neutrons cannot directly probe the microscopic nature of the coexisting state between static AF order and superconductivity [87, 88, 107], but neutron scattering experiments

in a magnetic field will allow a direct comparison on the effect of a field for the superconductivity and static AF order.

In previous neutron scattering experiments on optimally doped iron arsenide $BaFe_{0.9}Ni_{0.1}As_2$ [116], a c-axis aligned magnetic field up to 14.5-T has been found to suppress the intensity of the neutron spin resonance and shift it to a lower energy corresponding to the field-induced reduction in T_c. Althogh such a field also reduces the magnitude of the spin gap, it is not sufficient to induce static AF order [116]. As a consequence, it is not clear static AF order is a competing phase to superconductivity. In a separate neutron scattering on iron chalcogenide $FeTe_{0.5}Se_{0.5}$ superconductor [117], a 7-T magnetic field parallel to the a-b plane was foundto reduce the intensity of the resonance. Similar to the results on $BaFe_{0.9}Ni_{0.1}As_2$ [116],a 7-T field was also insufficient to induce the static AF order in the sample [117].

In this section, we report neutron scattering studies on the static AF order and spin excitations of underdoped $BaFe_{1.92}Ni_{0.08}As_2$ [$T_c = 17$ K] under the influence of an applied magnetic field. At zero field, previous neutron scattering experiments on similar samples have shown that the static AF ordered moment reduces at the onset of superconductivity, together with the appearance of a neutron spin resonance in the magnetic excitation spectra [87, 88, 107]. Upon application of a magnetic field in the FeAs-plane, the static AF order is enhanced below T_c, but is not affected in the temperature range below T_N and above T_c ($T_c < T < T_N$). The enhancement of the static AF order is accompanied by suppression of the superconducting T_c and the intensity of neutron spin resonance. These results are consistent with a competing static AF order and superconductivity, and suggest that the interplay between magnetism and superconductivity in iron arsenide superconductors is similar in many ways to that for copper oxide superconductors.

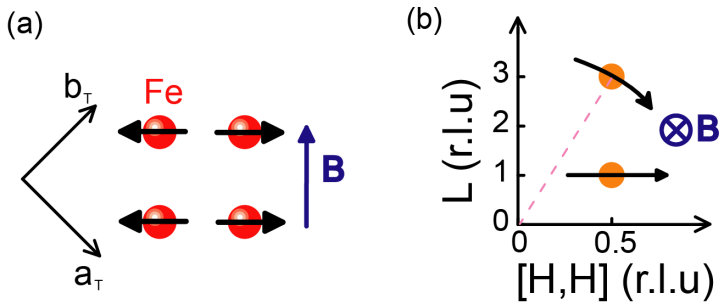

Figure 3.8: The antiferromagnetic spin structure of the undoped parent compound $BaFe_2As_2$ and the direction of applied field. (b) The reciprocal space probed in the present experiment and the direction of applied field.

3.2.2 Experimental setups

In previous experiments on underdoped $BaFe_{1.906}Co_{0.094}As_2$ (T_c = 15 K) [87], $BaFe_{1.92}Co_{0.08}As_2$ (T_c = 11 K) [88], and $BaFe_{2-x}Ni_xAs_2$ [107] superconductors, the static AF order was found to coexist with superconductivity and cooling below T_c's in these samples induced a weak neutron spin resonance in the magnetic excitations spectra at the expense of the AF Bragg peak intensity. For $BaFe_{1.92}Ni_{0.08}As_2$ with T_c = 17 K, the static AF order occurs below T_N = 44 K as shown in Fig. 3.9(a). To study the effect of an in-plane magnetic field on the static AF order and spin excitations, we have carried out neutron scattering experiments on the BT-7 thermal and SPINS cold triple-axis spectrometers [107] and on MACS cold neutron spectrometer [118] at the NIST Center for Neutron Research.

We defined the wave vector Q at (q_x, q_y, q_z) as $(H, K, L) = (q_x a/2\pi, q_y b/2\pi, q_z c/2\pi)$ reciprocal lattice units (rlu) using the tetragonal nuclear unit cell, where a = 3.89 Å, b = 3.89 Å, and c = 12.77 Å. We co-aligned about 5 grams of single crystal $BaFe_{1.92}Co_{0.08}As_2$ in the $[H, H, L]$ horizontal scattering plane (with mosaicity ∼3°), and put our samples inside either a liquid He cryostat or a 12-T vertical field magnet. For thermal triple-axis measurements on BT-7, we used pyrolytic graphite (PG) as monochromator and analyzer with typical collimations of open-40′-S-40′-120′ and the 15-T superconducting magnet system. The final neutron energy was chosen to be

$E_f = 13.5$ meV with a PG filter before the analyzer. For cold neutron SPINS and MACS measurements, we chose final neutron energy of $E_f = 5.0$ meV with cold Be filters to eliminate $\lambda/2$ scattering. Figure 3.8(a) shows the spin structure of the parent compound, and Figure 3.8(b) illustrates the reciprocal space probed in the experiments.

3.2.3 Inhancement of AF order under a magnetic field

We first discuss our neutron scattering results on $BaFe_{1.92}Ni_{0.08}As_2$ in elastic channel. The solid diamonds in Fig. 3.9(a) shows the temperature dependence of the magnetic scattering at $Q = (0.5, 0.5, 3)$. Consistent with earlier results on underdoped FeAs-based superconductors [87, 88, 107], $BaFe_{1.92}Ni_{0.08}As_2$ orders antiferromagnetically below a Néel temperature of $T_N = 44$ K, and the magnetic Bragg intensity decreases below the onset of the superconducting T_c.

To see if the static AF order in $BaFe_{1.92}Ni_{0.08}As_2$ can be enhanced by application of a magnetic field, we carried detailed temperature dependent measurements at the AF Bragg peak position $Q = (0.5, 0.5, 3)$ with and without a 10-T magnetic field applied along the $[1, -1, 0]$ direction [Fig. 3.9(a)]. While a 10-T in-plane magnetic field has no observable effect on the Néel temperature and magnetic scattering above 20 K, it clearly enhances the magnetic scattering for temperatures below T_c compared to that of the zero field data. Figures 3.9(c) and 3.9(d) show the rocking curves of the field-on field-off difference plots at 5 K and 20 K, respectively. While a 10-T magnetic field has no influence on the static AF order at 20 K [Fig. 3.9(d)], it induces additional magnetic scattering at $(0.5, 0.5, 3)$ below T_c [Fig. 3.9(c)].

3.2.4 Suppression of spin resonance intensity under a magnetic field

To determine if the enhanced static AF order in Fig. 3.9(a) under a magnetic field is compensated by a reduction in the intensity of the resonance and low-energy

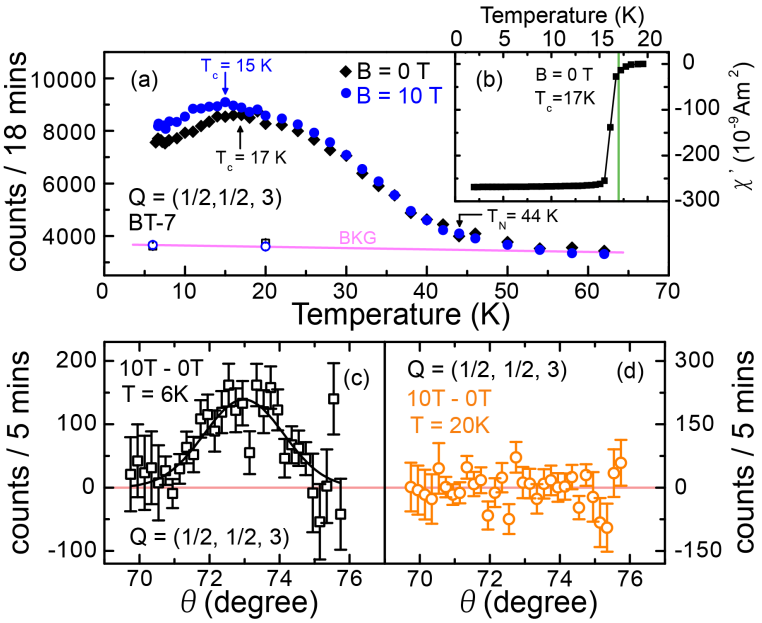

Figure 3.9: (a) Temperature dependence of the AF Bragg peak at (0.5,0.5,3) at zero field and at the 10-T in-plane field. The data were taken on BT-7 and showed TN = 44 K. The background scattering has no temperature or field dependencet (b) Temperature dependence of the Meissner and shielding signals on thin slabs of $BaFe_{1.92}Ni_{0.08}As_2$. (c) The field-on subtract field-off rocking-curve scan through the (0.5,0.5,3) AF Bragg peak at 6 K. (d) Identical rocking-curve scans at 20 K, clearly indicating that the applied field has no observable effect on the static AF order below T_N and above T_c.

spin excitations, we carried out inelastic neutron scattering measurements under the influence of a magnetic field. Figure 3.10(a) shows constant-Q scans carried out below and above T_c in zero and 11-T in-plane field at $Q = (-0.5, -0.5, 1)$. At zero field, the scan at 4.5 K shows a clear resonance peak near 6 meV. Upon application of a 11-T in-plane field, the intensity of the mode is reduced [Fig. 3.10(a)]. The zero and 11-T field difference plot at 4.5 K in Figure 3.10(b) shows a peak centered at 6 meV. Therefore, while a 14-T field applied along the c-axis can suppress the intensity and reduce the energy of the resonance, a 11-T field applied in the FeAs-plane only reduces the intensity of the resonance and does not affect the energy of the mode. This can be naturally explained by the vortex lattice effects in superconductors. A c-axis aligned

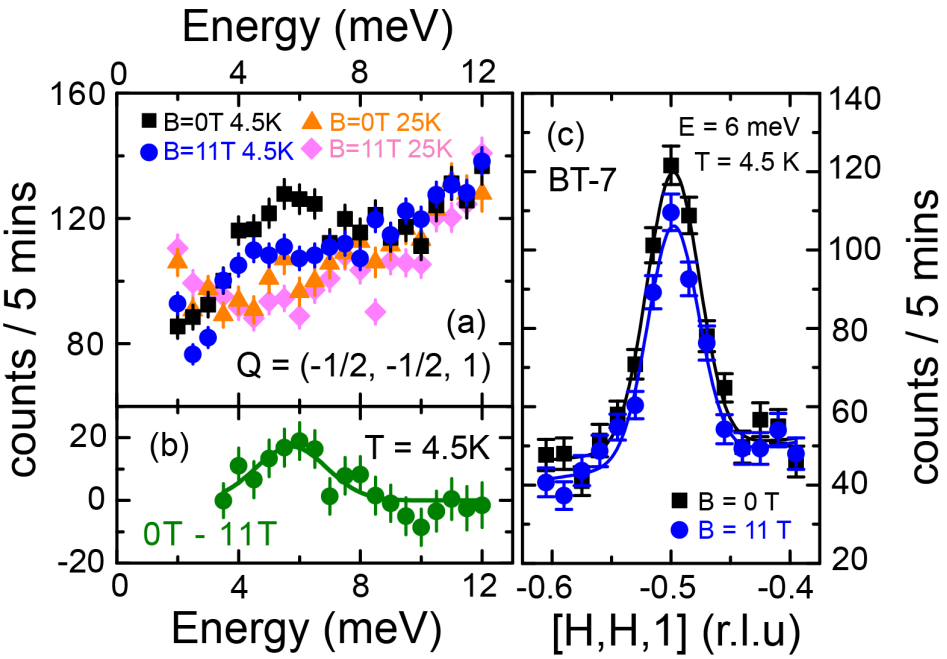

Figure 3.10: (a) Constant-Q scans at Q = (0.5,0.5,1) below and above T_c at zero field and at the 11-T in-plane field. (b) The field-offfield-on difference plot at T = 4.5 K shows that the magnetic scattering near the resonance energy is affected most by the applied field. (c) Constant-energy scans at the resonance energy for the zero and the 11-T fields. The field-induced reduction in magnetic scattering occurs at the AF wave vector Q = (0.5,0.5,1).

magnetic field can suppress superconductivity much more efficiently than an in-plane field because the former induces supercurrent in the FeAs-plane, while vortex lattices in an in-plane field are present in-between the superconducting FeAs-planes. Figure 3.10(c) shows constant-energy scans in the superconducting state with and without the applied magnetic field. The effect of an applied field is to suppress magnetic scattering centered at the AF wave vector near the resonance energy.

Figure 3.11 shows the temperature dependence of the resonance at zero and 11 Tesla. At zero field, the intensity of the mode increases gradually below $T_c = 17$ K [Fig. 3.11(a)]. Under the influence of a 11-T field in the FeAs-plane, the resonance intensity starts to increase below about 15 K [Fig. 3.11(b)]. The reduced T_c in the in-plane field for the resonance is consistent with the reduction in the AF Bragg

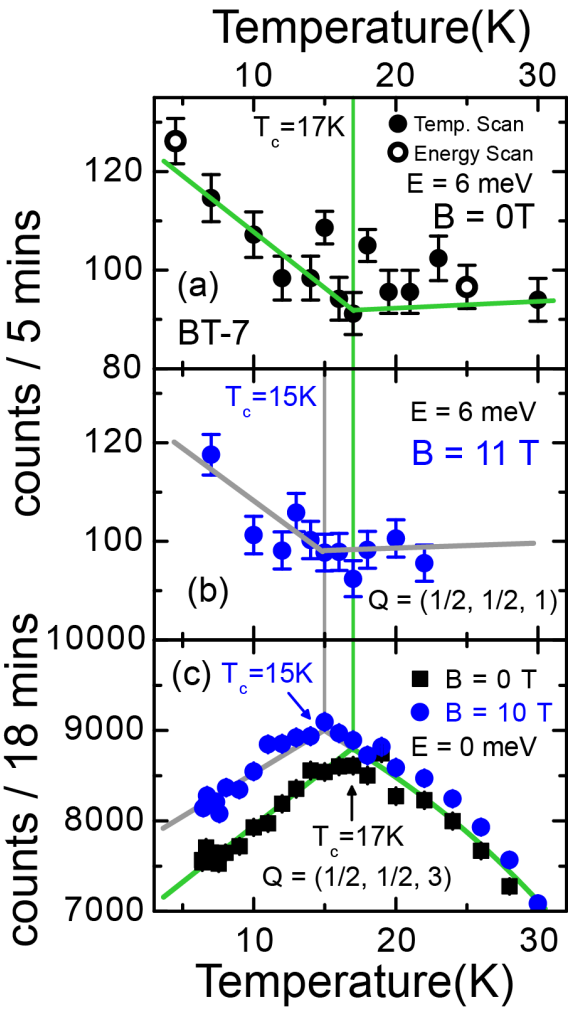

Figure 3.11: (a) Temperature dependence of the E = 6meV scattering in zero field at Q = (0.5,0.5,1) for $BaFe_{1.92}Ni_{0.08}As_2$. The scattering increases in intensity below the T_c of 17 K. (b) Identical temperature dependence of the E = 6 meV scattering under the 11-T field. The field-induced T_c has now shifted to 15 K. (c) Expanded plot of the elastic magnetic scattering in zero field and in the 11-T field. The data confirm the shift in T_c with a nonzero field.

intensity as shown in Fig. 3.11(c). These results are also consistent with the expected T_c reduction from the transport measurements for similar T_c Co-doped materials [119]. If we assume that the resonance is a direct probe for measuring electron pairing and superconductivity in iron arsenide superconductors, the observation of the elastic magnetic intensity gain at the expense of the resonance provides direct

evidence that the static AF order in underdoped $BaFe_{1.92}Ni_{0.08}As_2$ is competing with superconductivity.

3.2.5 Discussion and conclusions

We now discuss the implications of our results and compare them with that of the magnetic field effect in copper oxide superconductors. For the single layer hole-doped cuprate $La_{2-x}Sr_xCuO_4$ near doping of = 0.125, application of a magnetic field can enhance the static long-range AF order [120–122]. These results were initially interpreted as due to antiferromagnetism within the vortex cores of the superconductors under the field [122], but has since been understood as due to proximity to the quantum critical point separating a purely superconducting phase from a superconducting/antiferromagnetism coexisting phase [123, 124]. For the bilayer hole-doped cuprate $YBa_2Cu_3O_{6+x}$, while the initial neutron scattering experiments have shown that a field can suppress the intensity of the resonance [125], the enhanced static order under a field has only recently been observed in underdoped $YBa_2Cu_3O_{6.45}$ [126] and is not a universal phenomenon [127]. In the case of electron-doped cuprates, the enhanced static AF order under a field [113] is compensated by suppressing the intensity of the resonance [114].

The observation of a field-induced enhancement of the static AF order at the expense of the resonance in underdoped iron arsenide superconductor $BaFe_{1.92}Ni_{0.08}As_2$ is similar to the field-induced effects on the static AF order and resonance in some of the cuprate superconductors [120–122, 124, 126], particularly the electron-doped materials [113, 114]. Although our results indicate a competing static AF order with superconductivity, it is still unclear whether the static AF order in $BaFe_{1.92}Ni_{0.08}As_2$ microscopically coexists with superconductivity as theoretically envisioned [108, 109]. In previous muon spin rotation (μSR) experiments on underdoped $BaFe_{2-x}Co_xAs_2$ with coexisting static AF and superconducting phases, the local magnetic field detected by muons does not show a noticeable reduction below T_c [128]. Since muons

are local probes, this result suggests that the static AF moment of the system does not decrease below T_c. Therefore, the coexisting AF and superconducting phases might be mesoscopic, where superconductivity and AF order are intertwined in a very short length scale and live in separate regions. The relevant length parameter for superconducting regions is the superconducting coherence length, which is on the order of 20 Å [119]. On the other hand, the propagation of the field from the static Fe moment to the muon site is due to dipolar interaction, which is much shorter than the penetration depth and dies away in about 20 Å [129]. If the width of the superconducting rivers is smaller than the propagation range of the dipolar field, then the muons in the river regions can still feel the static internal field from the AF ordered background. In this scenario, application of a magnetic field that suppresses the superconducting parts of the sample enhances the static AF phase through volume fraction change (thus the reduction in the AF Bragg peak intensity) without changing the static ordered moment (no change in local field seen by μSR).

In summary, we have determined the effects of an in-plane magnetic field on the static AF order and spin excitations of the underdoped $BaFe_{1.92}Ni_{0.08}As_2$ superconductor. At zero field, the system orders antiferromagnetically below about 44 K. While application of a magnetic field in the FeAs-plane has no observable effect on static AF order below T_N and above T_c, it clearly enhances the zero-field static AF order at the expense of the neutron spin resonance. Our results provide direct evidence that the static AF order is a competing phase to superconductivity. However, the present neutron scattering data cannot conclusively determine if the static AF order in $BaFe_{1.92}Ni_{0.08}As_2$ is microscopically or mesoscopically coexisting with superconductivity.

Chapter 4

Magnetic Excitations in alkali iron selenide $\mathbf{Rb}_y\mathbf{Fe}_{1.6+x}\mathbf{Se}_2$

In this chapter, we used neutron time-of-flight spectrometers to investigate the magnetic excitations in $Rb_{0.8+y}Fe_{1.6+x}Se_2$ samples in three different phases. In insulating $Rb_{0.89}Fe_{1.58}Se_2$, the spin wave spectrum was measured by inelastic neutron scattering. We showed that the spin waves can be well described by a local Heisenberg Hamiltonian, and compared the fitted superexhange couplings with those in other IBS systems. A similar insulating sample with higher quality was heated above T_N to entet the paramagnetic phase, and strong suppression of susceptibility near high energy was discovered. The superconducting compound $Rb_{0.82}Fe_{1.68}Se_2$ was measured with an extra magnetic signal near Q=(1,0). The experiments in the insulating samples (below and above T_N) and superconducting samples (below and above T_c) provided a detailed comparison and showed evidence that the 245 system is rather different from either itinerant iron-pnictides or local copper-oxide systems.

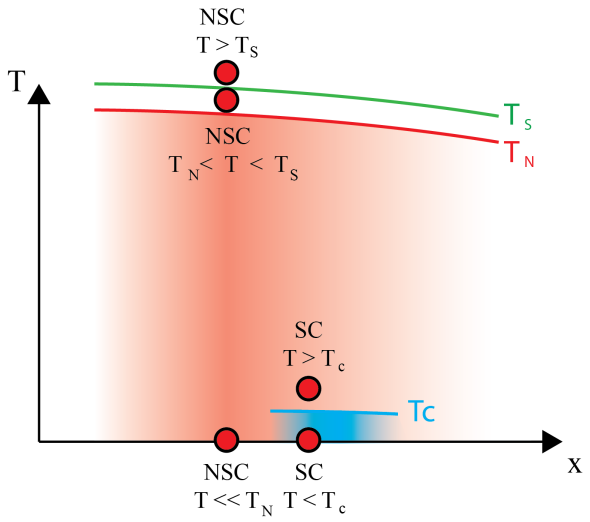

Figure 4.1: Schematic of phase diagram of $Rb_{0.8+y}Fe_{1.6+x}Se_2$. The measurements done in chapter 4 was marked as red circle. The insulating was measured below T_N, below T_S and above T_S. The superconducting sample was measured below T_c and above T_c.

4.1 Spin waves in anti-ferromagentically ordered insulating phase

4.1.1 Introduction

In the $BaFe_{2-x}Ni_xAs_2$ studied in the previous chapter, the electron band structure are composed of hole and electron Fermi pockets near the Γ (0,0) and M(1,0) / M(0,1) points, respectively [17], and sign-reversed quasiparticle excitations between the hole and electron pockets can induce s± wave superconductivity, giving rise to a neutron spin resonance at the in-plane antiferromagnetic (AF) wave vector $Q = (1, 0)$[28, 80, 83, 106, 130]. These results suggest that the s± wave electron pairing mechanism is a leading candidate for the microscopic origin of superconductivity in all iron-based superconductors [17]. However, superconductivity in the alkaline iron selenide $A_yFe_{1.6+x}Se_2$ (A = K, Rb, Cs) superconductors[61, 62, 131–133] may have a different origin from the sign-reversed s± wave electron-pairing mechanism[134–137]. Although $A_yFe_{1.6+x}Se_2$ are isostructural with the metallic AF iron pnictides such as (Ba,Ca,Sr)Fe_2As_2[130], they are insulators near x = 0[62, 132, 133] and form a $\sqrt{5} \times \sqrt{5}$ block AF structure with an Fe vacancy order (Fig. 4.2a) completely different from the iron pnictides[57, 65, 67, 138–140]. If sign reversed electron-hole pocket excitations between $\Gamma(0, 0)$ and $M(1, 0)/M(0, 1)$ points are necessary for superconductivity, superconductivity in alkaline iron selenides should have a different microscopic origin since angle-resolved photoemission experiments on these materials reveal only electron Fermi surfaces at $M(1, 0)/(0, 1)$ points and no hole Fermi pockets at $\Gamma(0, 0)$ point [134–136]. On the other hand, if AF spin excitations are responsible for superconductivity in Fe-based superconductors [141], one would expect that spin waves in the parent compounds of different classes of Fe-based superconductors have a similar energy scale despite dramatically different transport and magnetic properties. Previous work on spin waves of (Ba,Ca,Sr)Fe_2As_2 [54, 55, 142] and $Fe_{1.05}Te$ [90] suggests that the overall magnetic spectra can only be described by

considering both the local and itinerant electrons, and the next nearest neighbor (NNN) exchange couplings in these materials are similar. Since the insulating $A\mathrm{Fe}_{1.6+x}\mathrm{Se}_2$ has completely different magnetic structure, Néel temperatures, and static ordered moments (Fig. 4.2) from those of (Ba,Ca,Sr)$\mathrm{Fe}_2\mathrm{As}_2$ and $\mathrm{Fe}_{1.05}\mathrm{Te}$ [130], it is important to determine if spin waves in this material have an overall energy scale similar to other iron-based materials.

In this section, we use the inelastic neutron scattering to map out spin waves in the insulating $\mathrm{Rb}_{0.89}\mathrm{Fe}_{1.58}\mathrm{Se}_2$. We find that although $\mathrm{Rb}_{0.89}\mathrm{Fe}_{1.58}\mathrm{Se}_2$ has a Néel temperature ($T_N = 475$ K) much higher than that of the iron pnictides ($T_N \leq 220$ K) [130], spin waves for both classes of materials have similar zone boundary energies [54, 55, 142]. However, while itinerant electrons must be considered in order to understand spin wave properties in the AF iron pnictides [54, 55, 142], a local moment Heisenberg Hamiltonian can effectively describe the entire spin wave spectra of the AF $\mathrm{Rb}_{0.89}\mathrm{Fe}_{1.58}\mathrm{Se}_2$. A comparison of the Heisenberg Hamiltonian fitted effective exchange couplings in $\mathrm{Rb}_{0.89}\mathrm{Fe}_{1.58}\mathrm{Se}_2$, (Ba,Ca,Sr)$\mathrm{Fe}_2\mathrm{As}_2$ [54, 55, 142], and iron chalcogenide $\mathrm{Fe}_{1.05}\mathrm{Te}$ [90] reveals that their NNN exchange couplings are similar. Therefore, the NNN magnetic interactions in the AF alkaline iron selenides, iron arsenides, and iron tellurides are robust against the change of electronic band structures, must mainly stem from the superexchange interactions mediated by As/Se(Te), and may play a key role in the magnetism of Fe-based superconductors.

4.1.2 Experimental setups

Our single crystals of $\mathrm{Rb}_y\mathrm{Fe}_{1.6+x}\mathrm{Se}_2$ were grown using flux method. High-purity Fe, Se and Rb were mixed in appropriate stoichiometry and placed inside an alumina crucible. The crucible was sealed in Ar-filled silica ampoule. The mixture was heated to 950 °C for 5 h followed by 5 °C per hr cooling down to 900 °C, and then furnace cooling down to room temperature. The actual crystal composition of $\mathrm{Rb}_{0.89}\mathrm{Fe}_{1.58}\mathrm{Se}_2$ was determined inductively coupled plasma analysis.

Our neutron scattering experiments were carried out on the ARCS chopper spectrometer at the Spallation Neutron Source, Oak Ridge National Laboratory. We co-aligned 2.7 g of single crystals grown by self-flux (with mosaic of $\sim 6^{\circ}$). The incident beam energies were $E_i = 80, 140, 250, 440$ meV, and mostly with E_i parallel to the c-axis. Spin-wave intensities were normalized to absolute units using a vanadium standard (with 30% error). We define the wave vector Q at (q_x, q_y, q_z) as $(H_o; K_o; L_o) = (q_x a_o/2\pi; q_y a_o/2\pi; q_z c_o/2\pi)$ rlu, where $a_o = 5.65$ and $c_o = 14.46$ Å are the orthorhombic cell lattice parameters.

Before carrying out inelastic neutron scattering studies of spin waves in the insulating $Rb_{0.89}Fe_{1.58}Se_2$, we used polarized neutron diffraction measurements to confirm the previously proposed Fe_4 block AF checkerboard structure (Fig. 4.2(a)) [57, 65]. Since the ferromagnetic (FM) Fe_4 block in the $\sqrt{5} \times \sqrt{5}$ superlattice unit cell can have either left or right chirality (Figs. 4.2(a) and 4.2(b)), one expects to observe four AF Bragg peaks stemming from each of the chiralities. Figure 1c shows the expected AF peaks from the left chirality in reciprocal space using the orthorhombic unit cell similar to that of iron pnictides [54, 55, 142], where they occur at $(H_o, K_o, L_o) = (0.2 + m, 0.6 + n, L_o); (-0.2 + m, -0.6 + n; L_o); (0.6 + m, -0.2 + n, L_o); (-0.6 + m, 0.2 + n, L_o$ $(m, n = \pm 2, \pm 4, \cdots$, and $L_o = \pm 1, \pm 3, \cdots)$. Considering both chiralities for the AF order, there are eight Bragg peaks at wave vectors $(H_o, K_o, L_o) = (\pm 0.2 + m, \pm 0.6 + n, L_o)$ and $(H_o, K_o, L_o) = (\pm 0.6 + m, \pm 0.2 + n, L_o)$ from the block AF checkerboard structure (Fig. 4.2(d)), where the odd values of L_o indicate AF coupling along the c-axis direction [57, 65, 67, 140]. Therefore, acoustic spin waves in the AF ordered phase of $Rb_{0.89}Fe_{1.58}Se_2$ should stem from these eight Bragg peaks.

4.1.3 Spin wave measurement result

We first determine the overall energy bandwidth of $Rb_{0.89}Fe_{1.58}Se_2$ and the effective c-axis coupling. Figure 4.3(a) shows the background subtracted scattering projected

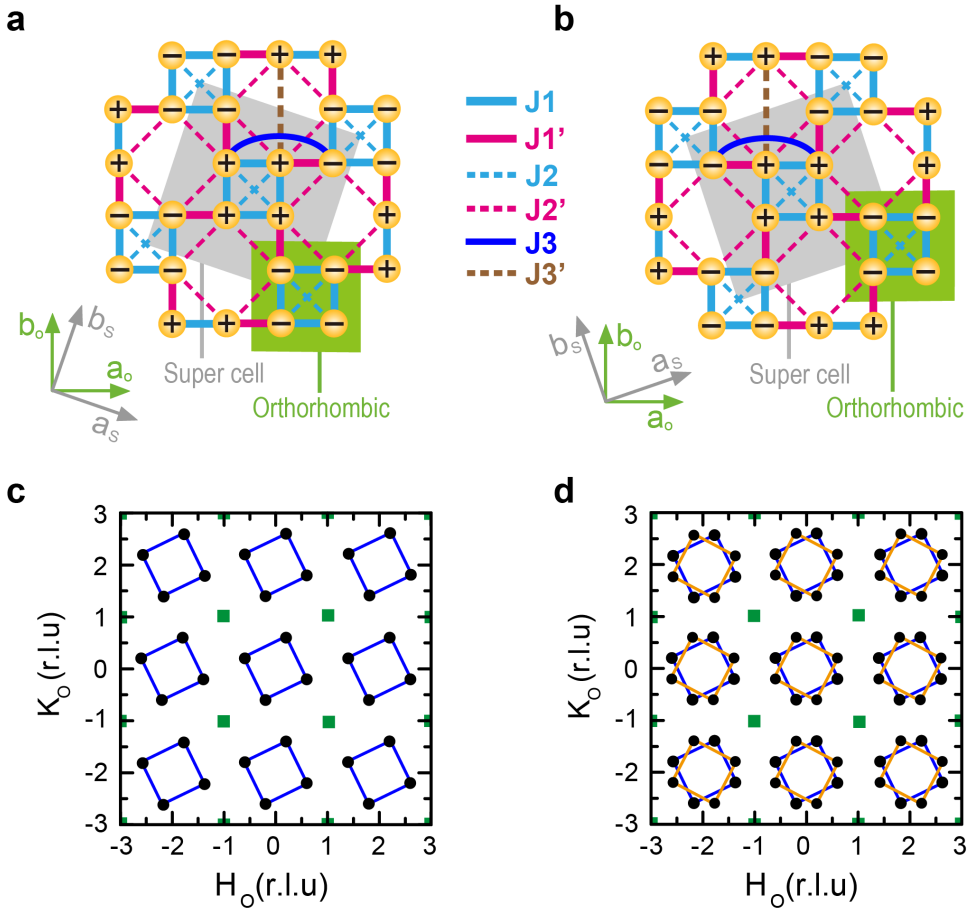

Figure 4.2: The AF spin structures of $Rb_{0.89}Fe_{1.58}Se_2$ are shown for (a) left and (b) right chirality. The $\sqrt{5} \times \sqrt{5}$ superlattice structure is marked as grey. The orthorhombic lattice cell is shaded green. The effective nearest neighbour, next nearest neighbour, next-next nearest neighbour exchange couplings are marked as J1 / J1′ , J2 / J2′ , and J3 / J3′, respectively. (c) The [H_o, K_o] reciprocal space with the expected AF Bragg peaks from the left chirality. The green squares show nuclear Bragg peak positions. (d) Bragg peaks for both chiralities.

in the wave vector ($Q = [-1.5, K_o]$) and energy plane. One can see three clear plumes of scattering arising from the in-plane AF zone centers $Q = (0, -2), (0, 0)$, and (0,2) rlu. With increasing energy, spin waves are gapped at energies between 75 and 95 meV (the bottom panel of Fig. 4.3(a)) and between 150 and 170 meV (the top panel of Fig. 4.3(a)). The zone boundary spin wave energies are around 220 meV

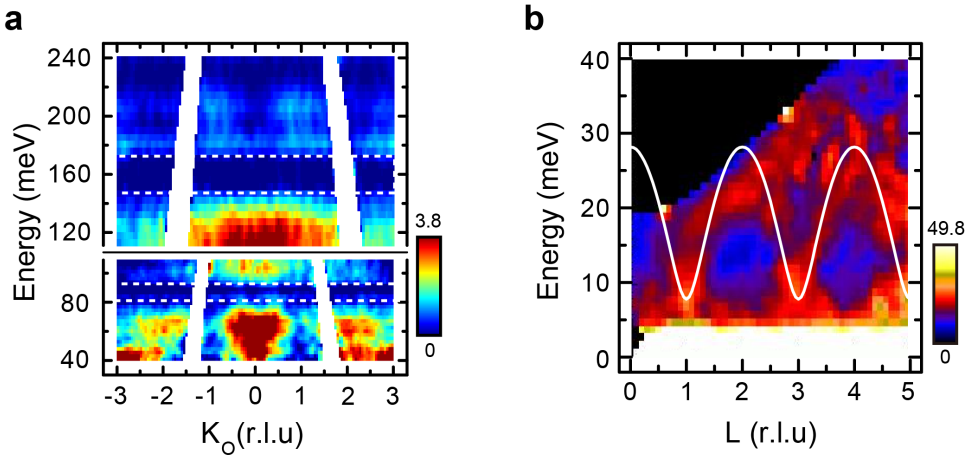

Figure 4.3: (a) Spin waves projected onto the K_o - E plane with H_o integration from 1 to 2. The scattering were measured with Ei = 440, 250 meV for top and bottom panels, respectively. (b) c -axis spin wave dispersion projected on the L E plane with H_o integration from 0.5 to 0.7 and K_o integration from 0 to 0.4.

(the top panel of Fig. 4.3(a)). Therefore, in spite of the large differences in Néel temperatures and AF structures of $Rb_{0.76}Fe_{1.6}Se_2$ (T_N = 475 K) [57, 65, 67, 140], (Ba,Ca,Sr)Fe_2As_2 ($T_N \leq$ 220 K) [54, 55, 142], and $Fe_{1.05}Te$ ($T_N \approx$ 70 K) [90], their zone boundary spin wave energies are rather similar. To estimate the AF coupling strength along the c-axis, we show in Fig. 4.3(b) spin waves projected in the wave vector $Q = [0.6, 0.2, L_o]$ and energy space. One can see clear dispersive spin waves stemming from AF positions $L_o = 1, 3, 5$ that reach the zone boundary energy near 30 meV.

To see the evolution of spin waves with increasing energy, we show in Fig. 4.4 the two-dimensional constant-energy (E) images of spin waves in the $[H_o, K_o]$ plane for various incident beam energies (E_i). From their c-axis dispersion (Fig. 4.3(b)), we know that spin waves in $Rb_{0.89}Fe_{1.58}Se_2$ are three-dimensional similar to that in (Ba,Ca,Sr)Fe_2As_2 [54, 55, 142] and center at AF wave vectors $Q_{AF} = (H_o, K_o, L_o) = (\pm 0.2 + m, \pm 0.6 + n, L)/(\pm 0.6 + m, \pm 0.2 + n, L)$ with $L_o = \pm 1, \pm 3, \cdots$ rlu. For an energy transfer of $E = 10 \pm 2$ meV (above the anisotropy gap of $E = 8$ meV), spin

waves are peaked at the expected eight AF Bragg positions Q_{AF} around $Q = (0, 0, \pm 1)$ rlu as shown in Fig. 2a. Upon increasing energies to $E = 26 \pm 2$ (Fig. 4.4(b)) and 30 ± 2 meV (Fig. 4.4(c)), spin waves from the two chiralities centered around the Q_{AF} positions become apparent and increase in size with increasing energy. The two spin wave rings from the left and right AF chiralities (Figs. 1a-1d) meet near $E = 45 \pm 3$ meV (Fig. 4.4(d)). At $E = 55 \pm 3$ meV, the overlapping spin waves from both AF chiralities still form rings around the Q_{AF} positions (Fig. 4.4(e)). Spin waves have evolved into broad rings centered around $(H_o, K_o, L_o) = (\pm m, \pm n, L_o)$ at $E = 70 \pm 3$ meV as shown in Fig. 4.3(a), just before disappearing into the $75 \leq E \leq 95$ meV spin gap. Upon re-emerging from the spin gap at an energy transfer of 110 ± 10 meV, spin waves form transversely elongated ellipses centered at the wave vectors $Q = (\pm 1, 0)/(0, \pm 1)$ (Fig. 4.4(g)), identical to the AF ordering wave vector of (Ba,Ca,Sr)Fe_2As_2 [54, 55, 142]. Finally, at $E = 200 \pm 20$ meV, an energy well above the $150 \leq E \leq 170$ meV spin gap, spin waves move into wave vectors $Q = (\pm 1, \pm 1)$ (Fig. 4.4(h)), almost identical to the zone boundary spin waves for $BaFe_2As_2$ [55] and $Fe_{1.05}Te$ [90].

4.1.4 Fitting of the spin wave using Heisenberg Hamiltonian

We use a local moment Heisenberg Hamiltonian with the effective nearest (NN or J_1, J_1'), next nearest (NNN or J_2, J_2'), and next next nearest neighbor (NNNN or J_3,J_3') magnetic exchange couplings (Fig. 4.2(a)) to fit the observed spin-wave spectra [143–147]. To account for the ∼8 meV low-energy spin gap, we add a spin anisotropy term J_s to align spins along the c-axis. There are 8 spins in each magnetic unit cell (Figs. 4.2(a) and 4.2(b)), therefore we should have four doubly-degenerate spin wave bands in the Brillouin zone. From Figs. 4.3 and 4.4, we see that spin waves exist in three separate energy ranges: the lowest branch starts from ∼9 meV to ∼70 meV, second from ∼80 meV to ∼140 meV, and the third branch from ∼180 meV to ∼230 meV. The high quality of the spin-wave data allows us to place quantitative constraints on

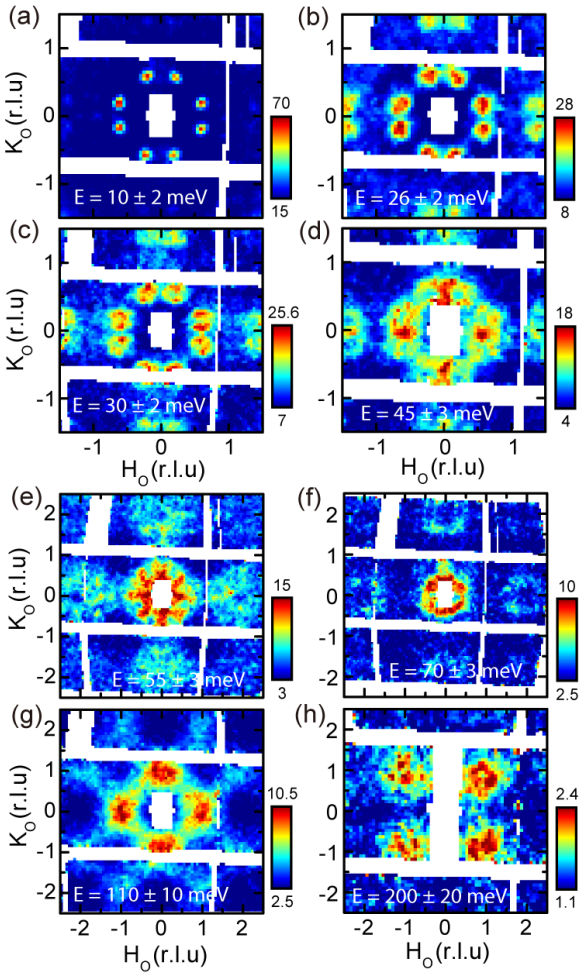

Figure 4.4: Spin wave excitations in the [H_o, K_o] scattering plane at energies (a) E = 10 ± 2; (b) E = 26 ± 2; (c) E = 30 ± 2; (d) E = 45 ± 3; (e) E = 55 ± 3; (f) E = 70 ± 3; (g) E = 110 ± 10; and (h) E = 200 ± 20 meV. (ac), (df),(g,h) were obtained with Ei = 80, 140, 250, and 440 meV, respectively, along the c -axis. The vertical colour bars indicate intensity scale in mbarns per sr per meV per f.u.

effective exchange couplings in the Heisenberg Hamiltonian. While the low-energy spin waves between ∼9 meV to ∼70 meV are acoustic modes arising mostly from AF interactions of the FM blocked spins, the two other branches of excitations are optical spin waves associated with exchange interactions of iron spins within the FM blocks [144–147]. We have attempted, but failed, to fit the entire spin wave spectra using only the effective NN and NNN exchange coupling Heisenberg Hamiltonian.

For spin-wave fits that include the NNNN exchange coupling J_3, we find that the low energy spin wave band (acoustic band) depends mainly on J_1',J_2', J_3, and J_c (the effective c-axis exchange coupling), but not J_1 and J_2. The second band depends on the J_2 heavily and the top band is mainly determined by J_1.

For simplicity, we consider each FM block with 4 aligned spins as a net spin S_{eff}. They interact with each other antiferromagnetically (via J_{eff}) to form a cuprates-like AF spin structure. There is one spin-wave band for this effective block-spin Heisenberg model, which has an analytical form for spin-wave dispersion. By comparing the J_{eff} Heisenberg Hamiltonian with those of the J_1-J_1'-J_2-J_2'-J_3-J_3' model, we find that spin waves in the first band can be approximately described by the J_{eff} Heisenberg Hamiltonian, where $J_{eff}S_{eff} = (J_1' + 2J_2' + 2J_3)S/4$ is $\sim$17 meV. This suggests that the low energy band is mainly determined by J_1',J_2', J_3, and J_c. Physically, the lowest energy band corresponds to the block spin waves where the 4 spins fluctuate in phase and resemble a single spin. Only at high energies, the relative motions within the blocks can be excited, which correspond to the two high energy optical modes. Thus the high energy bands are basically determined by the intra-block couplings J_1 and J_2.

To quantitatively determine the spin-wave dispersion, we determined the measured dispersion from a series of high symmetry scans through the (H_o, H_o, L_o) and $(H_o, 1/2H_o - 1/2, L)$ directions, where L_o was integrated to improve counting statistics. Figures 4.5 (a-c) summarize the dispersion of spin waves along the marked directions on the right panels. For the low-energy acoustic mode, we find a spin anisotropy gap below 8 meV and counter propagating spin waves for energies above 30 meV (Fig. 4.5(c)). The two high-energy optical spin-wave modes are essentially dispersionless. The blue and pink solid lines show Heisenberg Hamiltonian fits to the dispersion curves with and without J_3. The final fitted effective magnetic exchange couplings for spin-wave dispersions are $SJ_1 = -36 \pm 2$, $SJ_1' = 15 \pm 8$, $SJ_2 = 12 \pm 2$, $SJ_2' = 16 \pm 5$, $SJ_3 = 9 \pm 5$, $J_3' = 0$, $SJ_c = 1.4 \pm 0.2$, and $SJ_s = 0.44 \pm 0.1$ meV. Figure 4.5(d) shows the energy dependence of the observed local susceptibility [148]

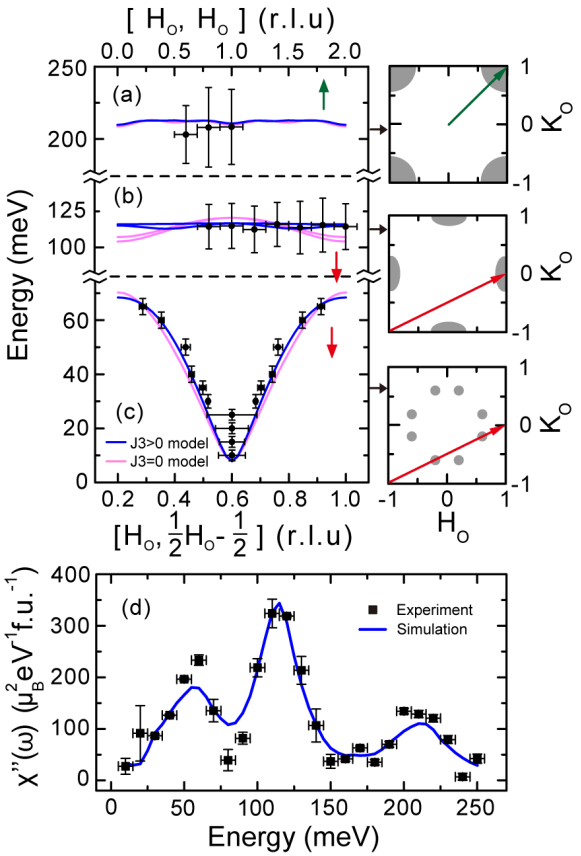

Figure 4.5: Spin wave dispersions of $Rb_{0.89}Fe_{1.58}Se_2$ and fits using the Heisenberg Hamiltonian. Spin wave dispersions obtained by cutting along high symmetry directions marked in the right panels for (a) highest energy optical-energy band; (b) medium-energy optical energy band; and (c) acoustic spin wave mode. The blue solid lines show fi ts with J 3 ¿ 0, while the pink solid lines are fi ts with J 3 = 0. (d) The energy dependence of the local susceptibility and our model calculation of the local susceptibility. The vertical error bars indicate the statistical errors of one standard deviation.

and our calculation using the fitted parameters. We see that the calculated local susceptibility agrees quite well with the data. To further compare the data in Fig. 4.4 with calculated spin waves using fitted effective exchange couplings, we show in Figure 4.6 the two-dimensional spin-wave projections in the $[H_o, K_o]$ plane convoluted with instrumental resolution. The calculated spin-wave spectra capture all essential features in the data.

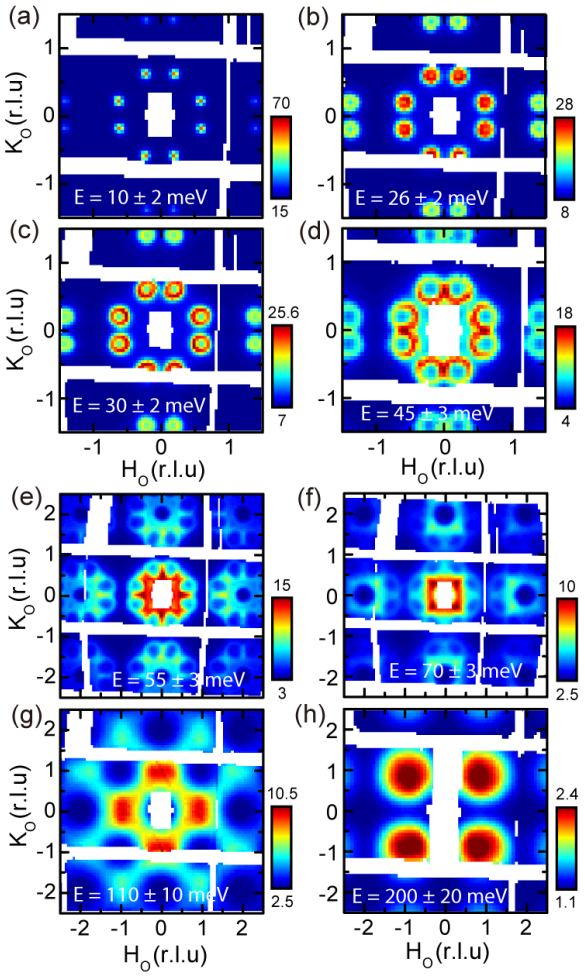

Figure 4.6: Calculated energy dependence of the spin waves. The wave vector dependence of the spin waves in the [H_o, K_o] scattering in absolute units for energies same as Fig. 4.4.

4.1.5 Conclusions

For a Heisenberg model with spin S, the total moment sum rule stipulates $M_0 = (g\mu_B)^2 S(S+1)$ [149]. For irons in the $3d^6$ electronic state, the maximum possible moment is $gS = 4$ μ_B/Fe for $g = 2$, giving $M_0 = 24$ μ_B^2/Fe. Based on the absolute spin wave intensity measurements in Fig. 4.5(d), the sum of the fluctuating moments within the Brillouin zone below ~250 meV is $\langle m^2 \rangle \approx 16 \pm 3$ μ_B^2/Fe. If we assume that the ordered moment is on the order of ~3 μ_B/Fe [65, 67, 140], we see that the

total moment sum rule is exhausted for magnetic scattering at energies below 250 meV. Therefore, spin waves in insulating $Rb_{0.76}Fe_{1.63}Se_2$ can be regarded as a classic local moment system where a Heisenberg Hamiltonian is an appropriate description of spin-wave spectra. For comparison, we note that the sum of the fluctuating local moments throughout the Brillouin zone for AF metallic $BaFe_2As_2$ [55] and superconducting $BaFe_{1.9}Ni_{0.1}As_2$ [107] are $\langle m^2 \rangle = 3.17 \pm 0.16$ and 3.2 ± 0.16 μ_B^2 per Fe(Ni), respectively (M. S. Liu *et al.*, Unpublished results). Since $\langle m^2 \rangle$ for iron pnictides are much less than that of the insulating alkaline iron selenides, there must be significant hybridization of Fe $3d$ with pnictide p orbitals and among themselves in iron pnictides, which leads to a metallic state where the Hund's coupling is less important than in the atomic limit [75]. This is consistent with the fact that a pure Heisenberg Hamiltonian cannot describe the entire spin wave spectra in AF iron pnictides[54, 55, 142] and iron chalcogenide $Fe_{1.05}Te$ [90].

It is instructive to compare the effective magnetic exchange couplings in different AF parent compounds of iron-based superconductors. First, comparing $Rb_{0.89}Fe_{1.58}Se_2$ with $Fe_{1.05}Te$ [90], we note that although their static AF orders have completely different structures, these two iron chalcogenides are very similar in terms of the values of their effective exchange couplings. Both of them have: Firstly, large FM J_1 (or J_{1a}). Secondly, large anisotropy between the two NN couplings $J_1(J_{1a})$ and J_1' (or J_{1b}). Thirdly, AF NNN couplings and small anisotropy between two NNN couplings J_2(or, J_{2a}) and J_2' (or J_{2b}). Finally, significant AF NNNN couplings J_3. Therefore, the presence of the iron vacancy ordering in $Rb_{0.89}Fe_{1.58}Se_2$ reduces magnetic frustration and stabilizes the block AF structure, but does not change the local magnetic exchange couplings strengths as compared to $Fe_{1.05}Te$ even though the $5p$ orbitals of Te should be larger than the $4p$ orbitals of Se.

Second, comparing $Rb_{0.89}Fe_{1.58}Se_2$ to iron-pnictides, we find that there are important differences as well as essential common features: the differences include the large differences in the sum of the fluctuating local moments $\langle m^2 \rangle$ and the NN exchange couplings. However, the NNN exchange couplings are rather similar

in spite of their insulating and metallic ground states. To summarize, while the NN exchange couplings vary significantly according to the spin configurations between the corresponding two NN sites in the magnetically ordered states of alkaline iron selenides, iron tellurides, and iron pnictides, the AF NNN exchange coupling remains almost uniform for these materials. This is consistent with the idea that the NNN coupling J_2 is mainly determined by a local superexchange mechanism mediated by As or Se/Te [150]. Therefore, regardless of their metallic or insulating ground states, different AF structures and Néel temperatures, spin waves in all parent compounds of Fe-based superconductors have a similar energy scale with a common NNN magnetic coupling controlled by the local superexchange interactions. Since superconductivity in Fe-based materials arises from electron or hole-doping of their AF parent compounds, the similarities in the magnetic properties of parent compounds suggest that the microscopic origin of superconductivity for doped superconductors should be similar as well.

To summarize, while the NN exchange couplings vary significantly according to the spin configurations between the corresponding two NN sites in the magnetically ordered states of alkaline iron selenides, iron tellurides, and iron pnictides, the AF NNN exchange coupling remains almost uniform for these materials. This is consistent with the idea that the NNN coupling J_2 is mainly determined by a local superexchange mechanism mediated by As or Se/Te [150]. Therefore, regardless of their metallic or insulating ground states, different AF structures and Néel temperatures, spin waves in all parent compounds of Fe-based superconductors have a similar energy scale with a common NNN magnetic coupling controlled by the local superexchange interactions. Since superconductivity in Fe-based materials arises from electron- or hole-doping of their AF parent compounds, the similarities in the magnetic properties of parent compounds suggest that the microscopic origin of superconductivity for doped superconductors should be similar as well.

4.2 Mangetic excitation in paramagnetic phase

4.2.1 Introduction

In the previous section, we showed that spin waves in insulating $Rb_{0.89}Fe_{1.58}Se_2$ can be accurately described by a local moment Heisenberg Hamiltonian [59]. For comparison, we note that there are still debates concerning whether a local moment Heisenberg Hamiltonian can appropriately model spin waves in iron pnictides [54, 55, 99, 151–155]. Moreover, recent spin wave measurements on iron chalcogenide $Fe_{1.1}Te$, which has a bicolinear AF structure and a Néel temperature of $T_N = 67$ K [90, 156–158], suggest that the effective spin per Fe changes from $S \approx 1$ in the AF state to $S \approx 3/2$ in the paramagnetic state, much different from the expectation of a conventional Heisenberg antiferromagnet [159]. On the other hand, temperature dependent paramagnetic scattering measurements in metallic AF $BaFe_2As_2$ reveal that high-energy ($E > 100$ meV) spin waves and the effective spin per Fe are essentially unchanged for temperatures up to $2.1T_N$ [160]. Given such diverse results in the parent compounds of iron-based superconductors, it is important to study the evolution of spin waves in a well-defined local moment Heisenberg system expected to be close to a Mott transition [161].

The semi-metallic nature of iron pnictides superconductors suggests that collinear AF order in the parent compounds such as $BaFe_2As_2$ [162] and $SrFe_2As_2$ [163] is the spin-density-wave type originating from the nesting of itinerant electrons between the hole and electron Fermi surfaces at Γ and M points in the Brillouin zone, respectively [164]. The insulating nature of the $A_yFe_{1.6+x}Se_2$ parent compounds provide an opportunity to test whether the system is indeed a Mott insulator similar to the insulating copper oxides, an AF semiconductor, or an insulator with coexisting itinerant and localized electronic states controlled by the Hunds rule coupling. The electron-electron correlation can be determined by measuring the spin wave pattern at energies higher than AF ordering temperature. In this experiment, we select parent

compound $Rb_{0.8}Fe_{1.6}Se_2$ to investigate the spin excitations in paramagnetic state. It should be noted that this sample is not the one we used in the previous experiment. The sample used this time was much bigger and had higher quality.

We report inelastic neutron scattering studies of paramagnetic spin excitations in AF $Rb_{0.8}Fe_{1.6}Se_2$. In the low-temperature insulating state, $Rb_{0.8}Fe_{1.6}Se_2$ form a $\sqrt{5} \times \sqrt{5}$ block AF structure with a large iron ordered moment and iron vacancy order, as described in the previous section [57, 65, 66]. Its spin waves have three branches, and can be well described by a local moment Heisenberg Hamiltonian [165]. On warming to 508 K above $T_N = 500$ K, the static AF order disappears but the lattice distortion induced by the iron vacancy order persists. Here, paramagnetic spin excitations at low-energies ($E \leq 30$ meV) form Lorentzian-like quasielastic peaks centered at the block AF wave vectors, whereas paramagnetic spin excitations at energies near optical spin waves are damped out. Upon further warming to $T = 1.05T_s = 1.11T_N = 553$ K, the $\sqrt{5} \times \sqrt{5}$ iron vacancy induced lattice distortion vanishes and the system becomes tetragonal with disordered iron vacancies [57]. The low-energy (< 30 meV) paramagnetic spin excitations are only weakly correlated at the AF ordering wave vectors for iron pnictides. Therefore, temperature dependence of spin waves in insulating $Rb_{0.89}Fe_{1.58}Se_2$ behaves like a local moment Heisenberg antiferromagnet, much different from that of metallic $Fe_{1.1}Te$ [159] and $BaFe_2As_2$ [160]. These results indicate that insulating $Rb_{0.8}Fe_{1.6}Se_2$ has less electron correlations and is not a copper-oxide-like Mott insulator.

4.2.2 Experimental setup

Our experiments were carried out at the MAPS time-of-flight inelastic neutron scattering spectrometer at ISIS, Rutherford-Appleton Laboratory, UK as described previously [55]. We grew single crystals of $Rb_{0.8}Fe_{1.6}Se_2$ using flux method [165]. It should be noted that this sample is not the one we used in the previous experiment [165]. The sample used this time was much bigger and had higher

quality. Similar to previous experiment, We define the wave vector Q at (q_x, q_y, q_z) as $(H_o; K_o; L_o) = (q_x a_o/2\pi; q_y a_o/2\pi; q_z c_o/2\pi)$ rlu, where $a_o = 5.65$ and $c_o = 14.46$ Å are the orthorhombic cell lattice parameters (green shaded area), for easy comparison with spin waves in $BaFe_2As_2$ [55, 160]. Considering both left and right chiralities from the AF order, there are eight Bragg peaks at wave vectors $(H_o, K_o, L_o) = (\pm 0.2 + m, \pm 0.6 + n, L_o)$ and $(H_o, K_o, L_o) = (\pm 0.6 + m, \pm 0.2 + n, L_o)$ from the block AF structure, where $m, n = \pm 2, \pm 4, \cdots$, and $L_o = \pm 1, \pm 3, \cdots$ (Fig. 4.7(b)). We coaligned ∼5 grams of single crystals of $Rb_{0.8}Fe_{1.6}Se_2$ (with mosaic $< 3°$) and loaded them inside a high temperature furnace. The temperature dependent AF Bragg peak and superlattice reflection associated with the $\sqrt{5} \times \sqrt{5}$ iron vacancy order disappear at $T_N = 500$ K and $T_s = 524$ K, respectively (Fig. 4.7(a)). This indicates the vanishing magnetic and structure orders consistent with earlier results on other $A_y Fe_{1.6+x} Se_2$ [57, 66, 166].

4.2.3 Evolution of spin excitations at different temperature

Figure 4.7(a) shows the evolution of the acoustic spin waves with increasing temperature along the $[H_o, -0.5 - 0.5H_o]$ direction as shown in the dashed line of Fig. 4.7(b). At 300 K, there are well-defined spin waves stemming from the block AF ordered wave vectors (the upper panel, Fig. 4.7(a)). Upon warming up to $T = 1.02T_N = 508$ K, paramagnetic spin excitations become much less well defined but still appear at the AF ordered wave vectors (the middle panel, Fig. 4.7(a)). Finally, on warming up to $T = 1.06T_s = 553$ K, paramagnetic spin excitations become featureless with no evidence for spin correlations at the AF ordering wave vectors (the bottom panel, Fig. 4.7(a)).

Figure 4.8 summarizes wave vector and temperature dependence of the low-energy acoustic spin excitations in the $[H_o, K_o]$ plane from 300 K to 553 K. At $T = 0.6T_N = 300$ K, spin waves are similar to the earlier results at 10 K [165], having a spin anisotropy gap at $E = 6 \pm 1$ meV and dispersing outward with increasing

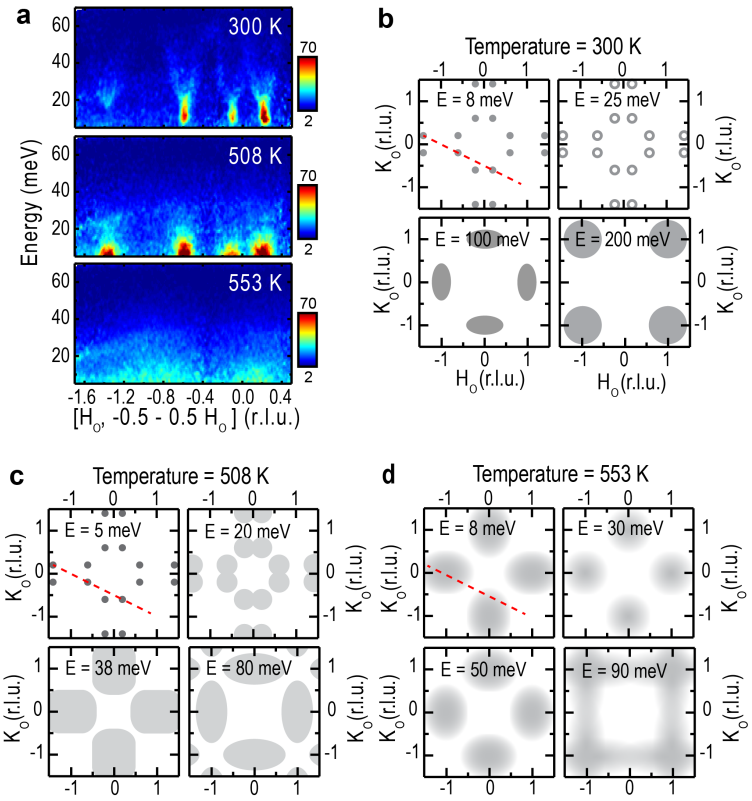

Figure 4.7: (a) Spin wave energy versus wave vector projected along the direction of the red-dashed lines in panels (b), (c), and (d) (along [H_o, 0.50.5H_o]) at T = 300, 508, and 553 K, respectively. The well-defined acoustic spin wave plumes are heavily damped at 508 K just above T_N and essentially disappear at 553 K just above T_s. (b)(c)(d) Schematics of paramagnetic spin excitations at 300 K, 508 K, 553 K, respectively.

energy (Figs. 4.8(a),(d),(g),(j),(m)). In the AF ordered state, spin waves stem from the $\sqrt{5} \times \sqrt{5}$ in-plane wave vectors and c-axis wave vectors of $L = 1, 3, 5$ [165].

On warming to $T = 1.02T_N$, paramagnetic spin excitations become quasi two-dimensional with no c-axis modulations. The spin anisotropy gap disappears and paramagnetic spin excitations move away from the $\sqrt{5} \times \sqrt{5}$ AF ordering positions for energies above $E = 30$ meV (Figs. 4.8(b),(e),(h),(k),(n)). Upon further warming to above T_s at $T = 1.06T_s$, paramagnetic spin excitations become very broad in

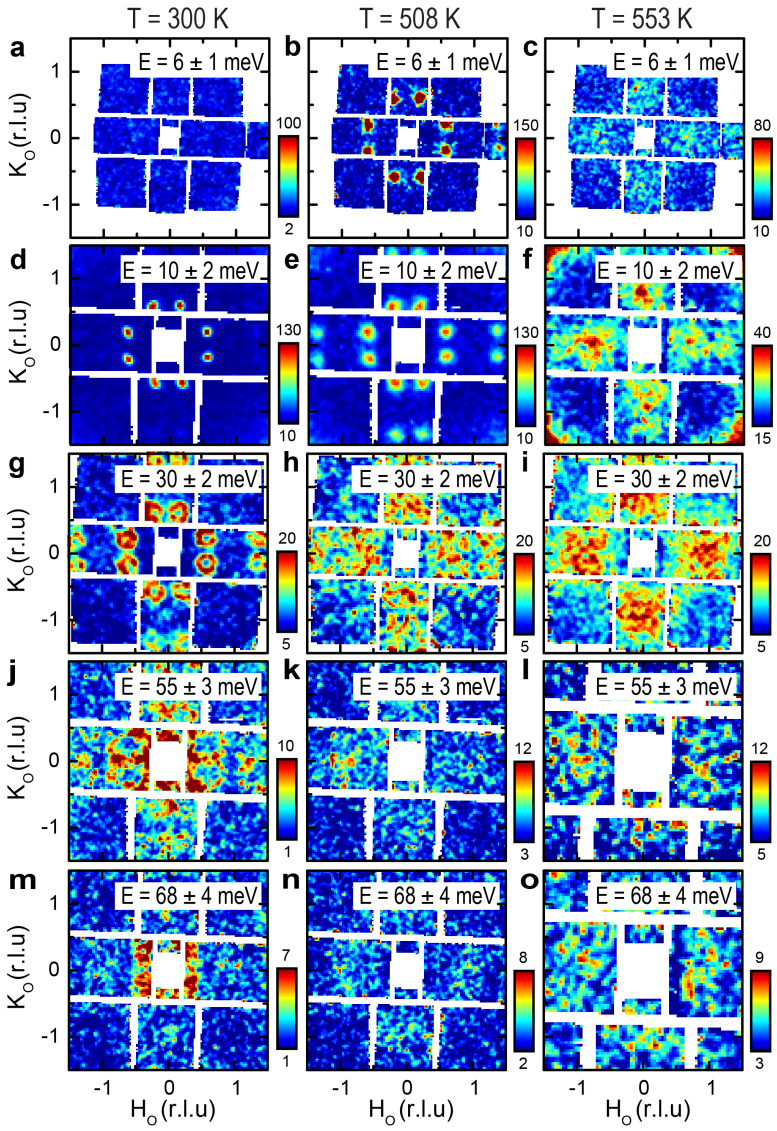

Figure 4.8: Spin wave and paramagnetic spin excitations in the [Ho,Ko] scattering plane at energies [(a),(b),(c)] E = 6 ± 1, obtained with E_i = 35 meV, corresponding to spin waves with L = 1.01 in (a), [(d), (e), (f)] E = 10 ± 2, [(g), (h), (i)] E = 30 ± 2 meV, taken with Ei = 80 meV, [(j), (k), (l)] E = 55 ± 3, [(m), (n), (o)] E = 68 ± 4 meV. Data in panels (j), (k), (m), and (n) are obtained with Ei = 140 meV, while data in panels (l) and (o) are taken with E_i = 250 meV. The left, middle, right column is data at 300 K, 508 K, 553 K.

momentum space and move to the AF wave vector of $BaFe_2As_2$ instead of the block AF structure (Figs. 4.8(c),(f),(i),(l),(o)).

Figure 4.9 shows the temperature dependence of the optical spin excitations. For the low-energy optical spin excitations at $E = 85 \pm 10$ meV, warming from 300 K (Fig. 4.9(a)) to 508 K (Fig. 4.9(b)) and 553 K (Fig. 4.9(c)) reduces the magnetic scattering intensity. This can be seen from the broadening of spin waves centered near $(\pm 1, 0)/(0, \pm 1)$ positions at 300 K to paramagnetic scattering essentially all wave vectors at 553 K. At $E = 110 \pm 10$ meV, well-defined spin waves at 300 K (Fig. 4.9(d)) completely disappear at 508 K (Fig. 4.9(e)) and 553 K (Fig. 4.9(f)). At 165 ± 15 meV, there is no observable magnetic scattering at 300 K (Fig. 4.9(g)), 508 K (Fig. 4.9(h)), and 553 K (Fig. 4.9(i)). Finally, spin waves centered near $(\pm 1, \pm 1)$ positions at $E = 195 \pm 15$ meV also vanish on warming from 300 K (Fig. 4.9(j)) to 508 K (Fig. 4.9(k)) and 553 K (Fig. 4.9(l)). Based on data in Figures 4.8 and 4.9, we construct in Figs. 4.7(b),(c),(d) the evolution of spin waves to paramagnetic spin excitations in insulating $Rb_{0.8}Fe_{1.6}Se_2$. Comparing the result with dispersions of paramagnetic excitations in $BaFe_2As_2$ [55, 160], where high-energy spin excitations near the zone boundary are weakly temperature dependent for temperatures up to $2.1T_N$, we see that paramagnetic scattering in $Rb_{0.8}Fe_{1.6}Se_2$ behave much like a conventional local moment Heisenberg antiferromagnet, forming Lorentzian-like quasielastic peaks centered at $E = 0$ [167].

4.2.4 Temperature dependence of integrated magnetic moments

To quantitatively determine the integrated magnetic moments and compare the outcome with those in $Fe_{1.1}Te$ [159] and $BaFe_2As_2$ [160], we plot in Fig. 4.10 temperature dependence of the local dynamic susceptibility for $Rb_{0.8}Fe_{1.6}Se_2$ [58]. For a local moment system with spin S, the total moment sum rule requires $M_0 = (g\mu_B)^2 S(S+1)$ when magnetic scattering is integrated over all energies and wave vectors [149]. For iron in the $3d^6$ electronic state, the maximum possible moment is $gS = 4\ \mu_B$/Fe assuming $g = 2$, thus giving $M_0 = 24\ \mu_B^2$/Fe. In previous work [165],

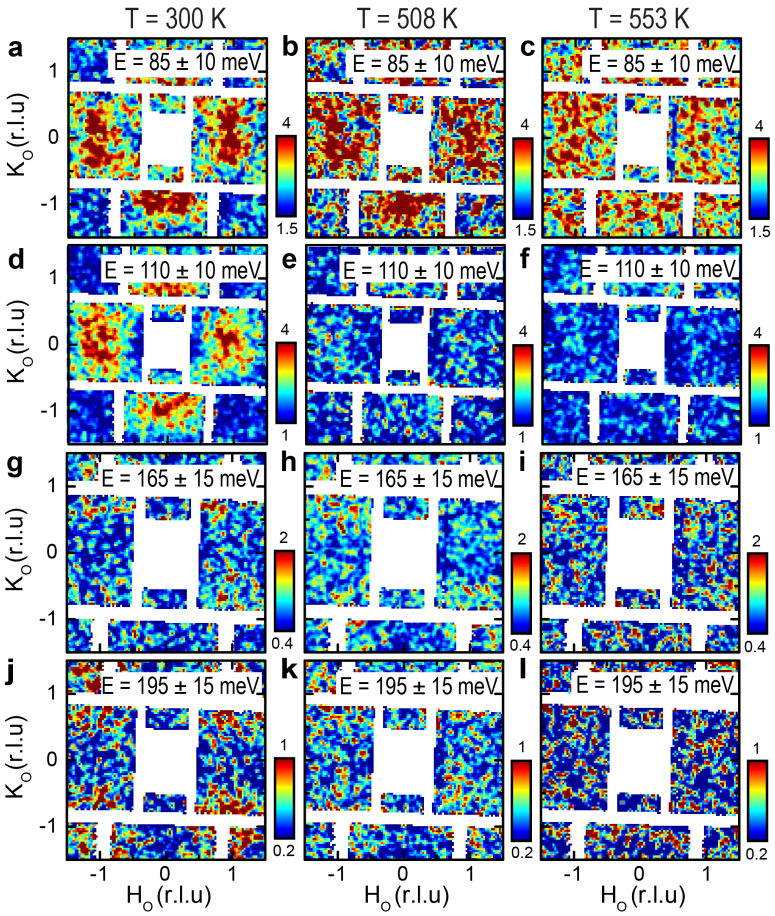

Figure 4.9: Spin excitations in the [H_o,K_o] scattering plane at energies [(a), (b), (c)] E = 85 ± 10, [(d), (e), (f)] E = 110 ± 10, [(g), (h), (i)] E = 165 ± 15, and [(j), (k), (l)] E = 195 ± 15 meV. The data in panels (a)(f) and (g)(l) are obtained with incident neutron beam energies Ei = 250 and 440 meV, respectively, along the c axis. The left, middle, and right columns are identical spectra at 300 K, 508 K, and 553 K, respectively.

we estimated that the total moment sum rule is exhausted for $Rb_{0.89}Fe_{1.58}Se_2$ below ∼250 meV. The energy dependence of the local susceptibility becomes progressively weaker on warming from 300 K to 508 K and 553 K.

Figure 4.10(b) shows temperature dependence of the ordered moment (open diamonds) [57, 66, 166] and integrated local susceptibility at three temperatures investigated (solid circles). Consistent with earlier results [165], we find that the

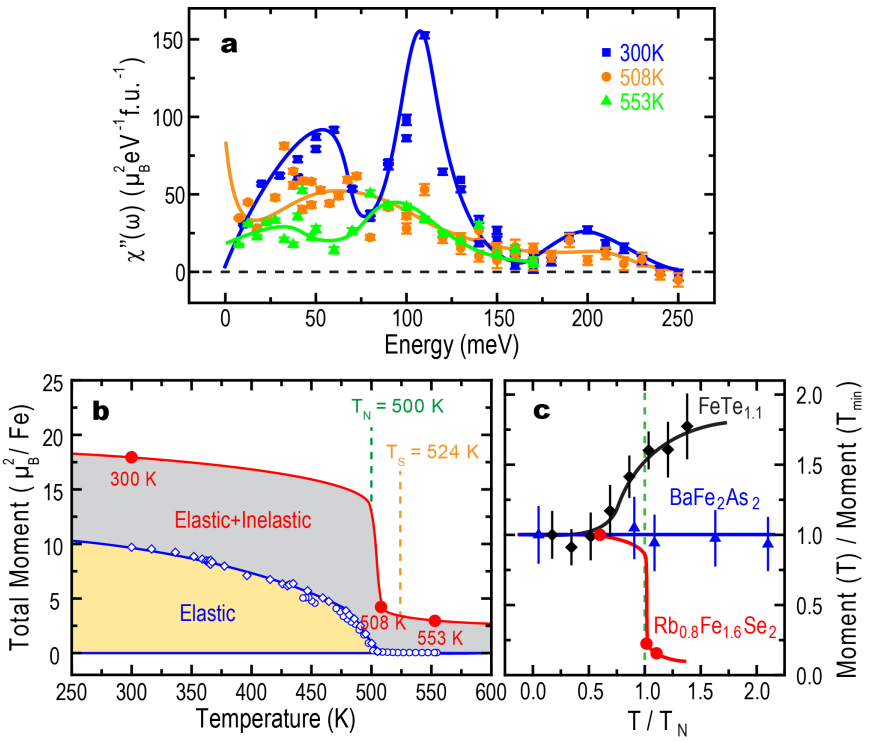

Figure 4.10: (a) The energy dependence of the local susceptibility at 300, 508, and 553 K. The solid lines are guides to the eye. (b) Temperature dependence of the energy integrated local susceptibility including both the static magnetic order parameter and contribution from spin excitations, obtained by numerically summing up the data in panel (a). (c) Normalized total fluctuating moments M(T)/M(T_min) versus T/T_N for $Fe_{1.1}Te$ [159], $BaFe_2As_2$ [160] and $Rb_{0.8}Fe_{1.6}Se_2$. The errors bars for $Rb_{0.8}Fe_{1.6}Se_2$ are smaller than the size of the symbol.

total moment sum rule is almost exhausted for $Rb_{0.8}Fe_{1.6}Se_2$ at 300 K, corresponding to a full moment of $gS = 4\ \mu_B$/Fe with $S = 2$. On warming to 508 K and 553 K, the total integrated moment drops dramatically, reflecting the fact that our unpolarized neutron scattering experiment can only probe correlated magnetic excitations and are not sensitive to wave vector independent paramagnetic scattering.

For comparison, we note that the integrated magnetic spectral weight of $Fe_{1.1}Te$ was found to increase from the AF state to the paramagnetic state [159], while the total integrated moment of $BaFe_2As_2$ remains essentially unchanged from $T = 0.05T_N$ to $T = 2.1T_N$ [160]. To illustrate this point, we plot in Figure 4.10(c) the normalized

total fluctuating moment ($M(T)/M(T_{min}$ K), where $M(T_{min}$ K) is integrated local moment in the lowest temperature of the AF ordered state) as a function of T/T_N for $Fe_{1.1}Te$ [159], $BaFe_2As_2$ [160], and $Rb_{0.8}Fe_{1.6}Se_2$. It is clear that temperature dependence of the fluctuating moment in $Rb_{0.8}Fe_{1.6}Se_2$ behaves differently from the other iron-based materials.

4.2.5 Conclusions

Compared with iron pnictide $BaFe_2As_2$ and iron chalcogenide $Fe_{1.1}Te$, insulating $Rb_{0.8}Fe_{1.6}Se_2$ appears to be a classic local moment Heisenberg antiferromagnet. The lack of correlated high-energy paramagnetic spin excitations in $Rb_{0.8}Fe_{1.6}Se_2$ suggests that electron correlation effects are smaller in $Rb_{0.8}Fe_{1.6}Se_2$, in contrast with iron pnictides [160] and iron chalcogenide [159]. This is also different from prototypical Mott insulators such as parent compounds of copper oxide superconductors, where paramagnetic spin excitations above 100 meV are not expected to be different from spin waves below T_N [168]. Our data thus suggests that insulating $A_yFe_{1.6+x}Se_2$ is not a copper-oxide-like Mott insulator. Alternatively, if insulating $A_yFe_{1.6+x}Se_2$ is a semiconductor with an energy gap of $\sim$500 meV opened below the $\sqrt{5} \times \sqrt{5}$ AF but not below the iron vacancy ordering temperature [169], one would expect spin excitations to change dramatically from below to above T_N but not significantly across T_s. Although paramagnetic spin excitations in the iron vacancy ordered state ($T = 508$ K) do appear at the $\sqrt{5} \times \sqrt{5}$ AF wave vectors for $E < 20$ meV, higher energy acoustic and optical spin excitations are heavily damped and are sensitive to the magnetic but not to the iron vacancy order. This is consistent with the idea that insulating $Rb_{0.8}Fe_{1.6}Se_2$ is an AF semiconductor [169].

Finally, if magnetism in $Rb_{0.8}Fe_{1.6}Se_2$ arises from a combination of itinerant electrons and local moments due to Hund's rule coupling similar to other iron-based materials [170–172], its paramagnetic spin excitations should behave similarly as well. Since paramagnetic spin excitations in iron chalcogenide and pnictides [159, 160] are

clearly different from those of $Rb_{0.8}Fe_{1.6}Se_2$, our data adds to the debate on why superconductivity in $A_yFe_{1.6+x}Se_2$ always appears near the $\sqrt{5} \times \sqrt{5}$ AF insulating phase [57, 66, 166], and which material is the true parent compound of $A_yFe_{1.6+x}Se_2$ superconductors [173, 174].

4.3 Spin resonance and magnetic excitations in superconducting phase

4.3.1 Background and motivation

In the previous two sections, the experiments in the AF insulating compound of alkali iron selenide $Rb_yFe_{1.6+x}Se_2$ were introduced. In this section, we select a superconducting sample $Rb_{0.82}Fe_{1.68}Se_2$ to investigate the magnetic excitations and their correlation with T_c.

In iron-pinctides, inelastic neutron scattering experiments on single crystals have found a resonance at $Q = (\pi, 0)$ in the spin excitations spectra [84, 89, 101, 175], thus providing further evidence that superconductivity is due to sign-reversed quasiparticle excitations between the hole and electron pockets [80, 106]. In the case of alkaline iron selenide superconductors $A_yFe_{1.6+x}Se_2$ (A = K, Rb, Cs) [61, 62, 131, 132], their parent compounds are insulators near $x = 0$ [62, 132] and form a $\sqrt{5}\times\sqrt{5}$ block AF structure with an Fe vacancy order [57, 65, 66, 138, 140] completely different from the collinear AF structure of the iron pnictides [28]. Furthermore, angle-resolved photoemission (ARPES) experiments on SC $A_yFe_{1.6+x}Se_2$ revealed only electron Fermi surfaces at the $M(\pi, 0)/M(0, \pi)$ points and no hole Fermi surface near $\Gamma(0, 0)$ [134–136]. Therefore, there is no Fermi surface nesting between $\Gamma(0, 0)$ and $M(\pi, 0)/M(0, \pi)$ points which can give AF spin excitations at $Q = (\pi, 0)$ (Fig. 4.11) [137]. Instead, the nesting properties between the $M(\pi, 0)/M(0, \pi)$ electron pockets with d-wave symmetry can produce a broad plateau like maximum around $Q = (\pi, \pi)$ that is bordered by two peaks at $Q \approx (\pi, 0.625\pi)$ and $Q \approx (0.625\pi, \pi)$ [176]. Although the recent discovery of the neutron spin resonance in SC $Rb_yFe_{1.6+x}Se_2$ at wave vector $Q = (\pm\pi, \pm 0.5\pi)$ [or $Q = (\pm 0.5\pi, \pm\pi)$] (Fig. 4.11(a)) [177, 178] is consistent with this picture [176], it remains unknown whether there are also spin excitations near wave vectors $Q = (\pi, 0)$ not associated with the Fermi surface nesting.

In this article, we use neutron scattering to map out the low-energy spin excitations in SC $Rb_{0.82}Fe_{1.68}Se_2$ (T_c = 32 K). In addition to confirming the neutron spin resonance at $Q = (\pm\pi, \pm 0.5\pi)$ [177, 178], we find clear evidence for incommensurate spin excitations near wave vector $Q = (\pi, 0)$ that are absent in insulating $Rb_{0.89}Fe_{1.58}Se_2$ (Fig. 1(b)) [165]. With increasing energy, the incommensurate spin excitions disperse inward to $Q = (\pi, 0)$ and disappear above $E = 30$ meV (Figs. 2,3). A comparison of spin excitations in the SC $Rb_{0.82}Fe_{1.68}Se_2$ with spin waves in the insulating $Rb_{0.89}Fe_{1.58}Se_2$ [165] reveals that the intensity gain of the $Q = (\pi, 0)$ excitations is at the expense of spin waves associated with the $\sqrt{5} \times \sqrt{5}$ AF phase (Figs. 4.12, 4.13). Since electron-hole pocket excitations are impossible between $\Gamma(0, 0)$ and $M(\pi, 0)/M(0, \pi)$ points [134–136], our results suggest the presence of local moments [179]. Moreover, the dispersion of the $Q = (\pi, 0)$ excitations is similar to that of copper oxide superconductors [180, 181] and insulating cobalt oxide [182], thus suggesting the possible presence of dynamic stripes [183].

4.3.2 Experiment details

We have performed inelastic neutron scattering experiments on the ARCS chopper spectrometer at the Spallation Neutron Source, Oak Ridge National Laboratory using identical conditions as previous work on spin waves in insulating $Rb_{0.89}Fe_{1.58}Se_2$ [165]. Figures 1a and 1b show the block AF structure and the positions of the AF peaks in reciprocal space, respectively [165]. We define the wave vector Q at (q_x, q_y, q_z) as $(H_o, K_o, L_o) = (q_x a_o/2\pi, q_y a_o/2\pi, q_z c_o/2\pi)$ rlu, where $a_o = 5.48$ and $c_o = 14.69$ Å are the orthorhombic cell lattice parameters similar to iron pnictides [55]. In this notation, the neutron spin resonance [177, 178] occurs at $Q = (\pm 1, \pm 0.5)$ [or $Q = (\pm\pi, \pm 0.5\pi)$] (Fig. 4.11(b)), while the $\Gamma \leftrightarrow M$ Fermi surface nesting gives scattering at $Q = (\pm 1, 0)$ rlu (Figs. 4.11(a)).

We co-aligned ∼6 grams of SC single crystals $Rb_{0.82}Fe_{1.68}Se_2$ grown by the self-flux method (with mosaic of ∼6°) [165], where the chemical composition was determined

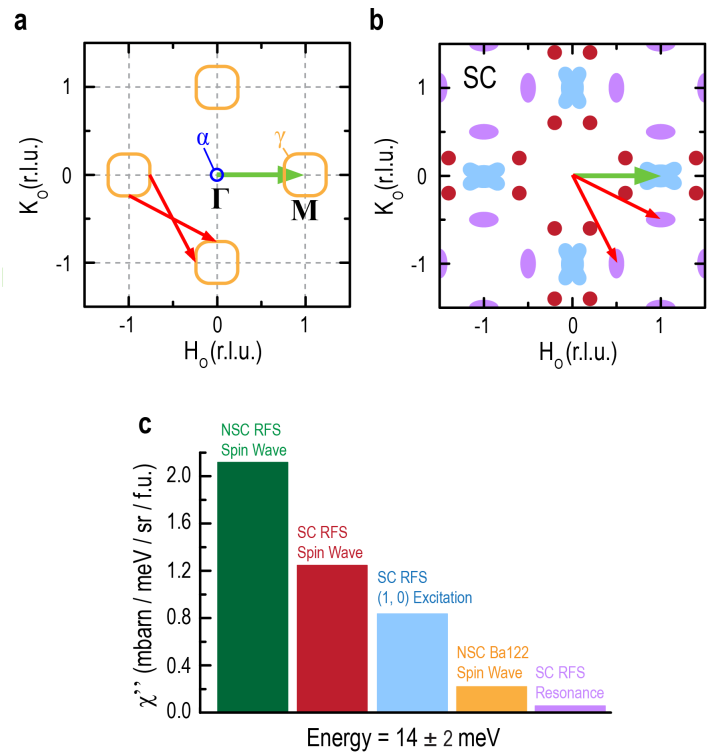

Figure 4.11: (a) Schematics of the Fermi surfaces of the SC $A_yFe_{1.6+x}Se_2$. There are four large electron pockets at Q = (±1,0)/(0,±1) and a small electron pocket at (0,0). The neutron spin resonance should originate from the electron-electron pocket excitations. The green arrow indicates the Γ - M transition. (b) Positions of observed spin excitations in the SC $Rb_{0.82}Fe_{1.68}Se_2$, where spin waves from the block AF phase, neutron spin resonance, and (π,0) excitations are marked as red solid circles, purple ellipses, and light-blue cross shapes, respectively. (c) Integrated intensity comparison of several samples at E = 14 ± 2meV.

by inductively-coupled plasma analysis. To ensure that the neutron spin resonance at $Q = (-1, 0.5)$ and $E = 14$ meV [177, 178] does not fall into the detector gaps on ARCS, we rotated the co-aligned samples counter-clockwise by ∼27 degrees. The incident beam energies were $E_i = 35, 80$ meV with E_i parallel to the c-axis. The scattering was normalized to absolute units using a vanadium standard [165].

4.3.3 Magnetic excitation near Q = (1,0)

From earlier work on $A_yFe_{1.6+x}Se_2$ [57, 65, 66, 140], we know that superconductivity coexists with the block AF order. Therefore, one should expect spin waves in SC $Rb_{0.82}Fe_{1.68}Se_2$ from the block AF phase [165]. Figure 4.12 summarizes the two-dimensional constant-energy (E) images of spin excitations in the $[H_o, K_o]$ plane for insulating and SC $Rb_yFe_{1.6+x}Se_2$. Since the subtle changes in the insulating and SC samples [57, 65, 66, 140] are not expected to much affect phonons in these materials, we assume that the new dispersive features in $Rb_{0.82}Fe_{1.68}Se_2$ are spin excitations associated with the SC phase. Figures 4.12(a)(c)(e)(g) show images of spin waves at energies $E = 8 \pm 2$, 12 ± 2, 20 ± 2, and 26 ± 2 meV, respectively, for insulating $Rb_{0.89}Fe_{1.58}Se_2$ [165]. They are centered at the expected AF wave vectors with no observable features at $Q = (1, \pm 0.5)$ and $Q = (1, 0)$ [165].

Figures 4.12(b)(d)(f)(h) plot images of the identical constant-energy cuts for SC $Rb_{0.82}Fe_{1.68}Se_2$ at $T = 6$ K. In addition to the usual spin waves from the block AF structure, we find new features near $Q = (\pm 1, 0)$ and $Q = (0, \pm 1)$. At $E = 8 \pm 2$ meV, there are four incommensurate peaks centered at $Q \approx (-1 \pm 0.14, \pm 0.1)$ (Fig. 4.12(b)). Upon increasing energies to $E = 12 \pm 2$ (Fig. 4.12(d)) and 20 ± 2 meV (Fig. 4.12(f)), the excitations become approximately centered at $Q = (\pm 1, 0)$. Finally at $E = 26 \pm 2$ meV, they disappear at $Q = (\pm 1, 0)$ and spin waves in the SC $Rb_{0.82}Fe_{1.68}Se_2$ and insulating $Rb_{0.89}Fe_{1.58}Se_2$ become indistinguishable (Figs. 2g and 2h).

Figures 4.13(a)-(d) show the expanded view of the spin excitations near $Q = (-1, 0)$ at different energies. At $E = 8 \pm 2$ meV, we see four distinct peaks (Fig. 4.13(a)). At $E = 12 \pm 2$ meV, the excitations become cross-like near $Q = (-1, 0)$ and one can also see the resonance centered at $Q = (-1, \pm 0.5)$ (Fig. 4.13(b)) [177, 178]. For $E = 16 \pm 2$ meV, the excitations are well centered at $Q = (-1, 0)$ (Fig. 4.13(c)). Finally at $E = 26 \pm 2$ meV, we find only spin waves from the block AF phase centered around the expected AF positions (Fig. 4.13(d)).

To see how the excitations near $Q = (1, 0)$ respond to superconductivity and

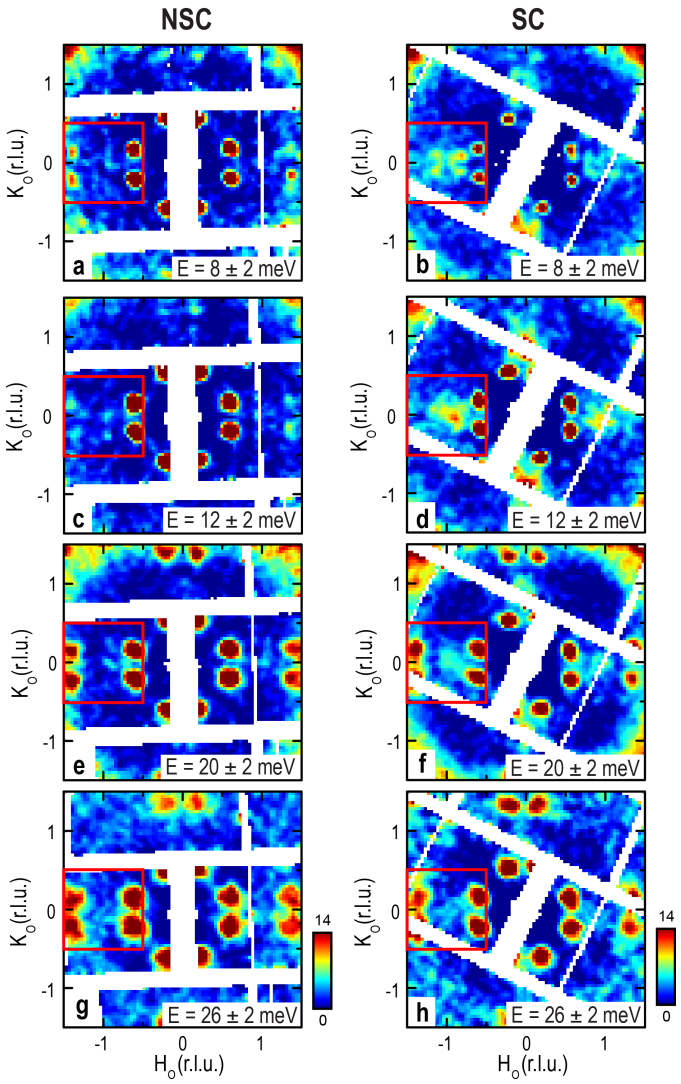

Figure 4.12: Wave-vector dependence of spinwave excitations at different energies for the NSC $Rb_{0.89}Fe_{1.58}Se_2$ at 10 K obtained with incident neutron energy of Ei = 80 meV. (b,d,f,h) Identical images for the SC $Rb_{0.82}Fe_{1.68}Se_2$ at 6 K. The red squares are the Brillouin zone for iron pnictides.

determine whether they are related to spin waves from the block AF phase, we show in Fig. 4.14 constant-energy cuts for the $Q = (1, 0)$ excitations and block AF spin waves at different temperatures. The neutron scattering cross section $S(Q, E)$ is related to the imaginary part of the dynamic susceptibility $\chi''(Q, \omega)$ by correcting for the Bose population factor via $S(Q, E) = 1/(1-\exp(-E/(k_B T)))\chi''(Q, E)$, where k_B is the Boltzmann's constant. Figures 4.14(a)(c)(c) show constant-energy cuts along

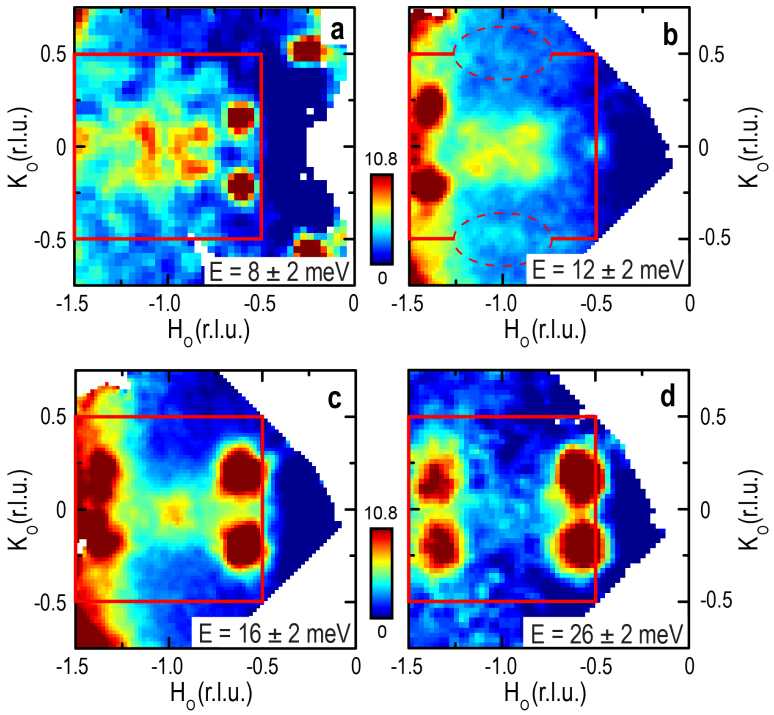

Figure 4.13: Expanded view of the excitations near Q = (1,0). The data in (b,c) are collected with $E_i = 35$ meV, while (a,d) are taken with $E_i = 80$ meV. The dashed ellipses in (b) mark positions of the resonance.

the K_o direction for different temperatures at $E = 8 \pm 2$, 12 ± 2, and 16 ± 2 meV, respectively. While $\chi''(Q,\omega)$ at the probed energies show no appreciable changes across T_c, it decreases on warming to $T = 250$ K, consistent with spin excitations.

For comparison, we find that $\chi''(Q,\omega)$ of the spin waves from the block AF phase are temperature independent between 10 K and 250 K. This is expected since spin waves are bosons and should follow the Bose factor below T_N. To see if superconductivity has any effect on spin waves of the block AF phase, we show in Figs. 4.14(b)(d)(f) $\chi''(Q,\omega)$ for SC $Rb_{0.82}Fe_{1.68}Se_2$ and insulating $Rb_{0.89}Fe_{1.58}Se_2$. While the spin wave intensity at $E = 10 \pm 2$ and 20 ± 2 meV in the superconductor are lower than that of the insulator, it becomes similar at $E = 34 \pm 2$ meV. To quantitatively determine the differences between the intensity gain near $Q = (-1, 0)$ with intensity loss of the AF spin waves in superconductor compared with that of

the insulator, we plot in Fig. 4.14(g) the intensity ratio of SC and insulating samples (SC/NSC) as black squares (yellow area in Fig. 4.14(h)) and orange circles (yellow plus green areas in 4.14(h)), respectively. We see that the spin wave intensity loss below ∼30 meV is approximately compensated by an intensity gain from excitations around $(-1, 0)$.

Finally, to confirm the neutron spin resonance near $E = 14$ meV at $Q = (-1, 0.5)$ in our SC $Rb_{0.82}Fe_{1.68}Se_2$ [177, 178], we carried out constant-Q and constant-energy cuts to the data in Fig. 4.15(b) below and above T_c. Figure 4.15(a) shows the $S(Q, E)$ for integrated wave vectors $Q = (-0.5 \pm 0.1, 1 \pm 0.1)$ at 6 K and 35 K. The temperature difference plot (6 K−35 K) in Fig. 4.15(b) has a clear peak at $E = 14$ meV, thus confirming the resonance below T_c [177, 178]. Figures 4.15(c) and 6e show constant-energy cuts along the two different high symmetry directions (see insets) below and above T_c. The temperature difference plots show well-defined peaks at the expected wave vector [177, 178]. Figure 1e compares the strength of the spin waves from the block AF structure in insulating and SC samples, the $(1, 0)$ spin excitations, the resonance, and spin waves of $BaFe_2As_2$ [55] near $E = 14$ meV.

4.3.4 Conclusions

The discovery of spin excitations near the (π,0)wave vector and their dispersion in the SC $Rb_{0.82}Fe_{1.68}Se_2$ has several important implications. First, since ARPES experiments reveal that SC $A_yFe_{1.6+x}Se_2$ have no hole-like Fermi surface at (0,0) [134–136], the (π,0) spin excitations cannot arise from quasiparticle excitations between Γ and M points and most likely come from localized magnetic moments [179]. Taking into account that the SC $Rb_{0.82}Fe_{1.68}Se_2$ also has a neutron spin resonance most likely arising from Fermi surface nesting and itinerant electrons [177, 178] these results suggest that localized moments and itinerant electrons may both exist in the magnetism of alkaline iron selenide superconductors. Second, the observation of low-energy incommensurate spin excitations and its inverse dispersion are reminiscent

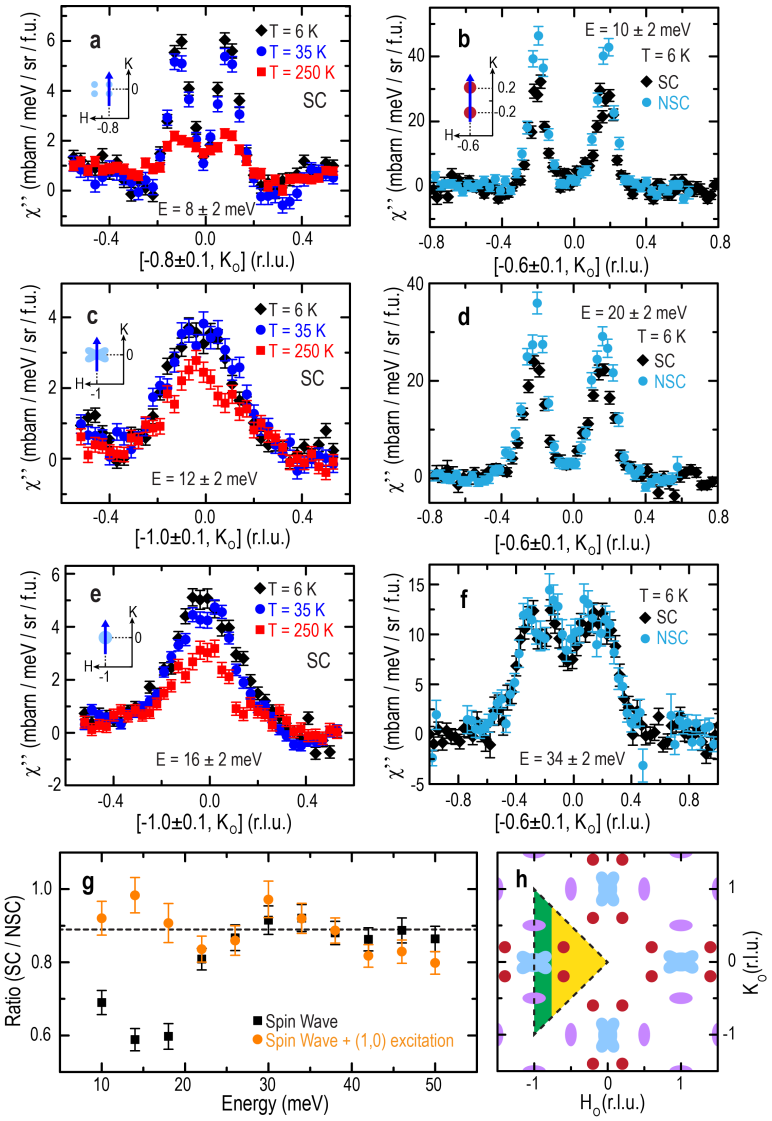

Figure 4.14: Cuts of χ"(Q,ω) along (a) the [0.8 ± 0.1,K], (c,e) [1 ± 0.1,K] directions for the Q = (1,0) excitations at different temperatures. (b,d,f) Comparison of the low-temperature spin wave intensities for SC and insulating samples using the same cuts along the [0.6 ± 0.1,K] direction. The spin wave intensity of the SC sample are lower at (b) E = 12 ± 2 and (d) 20 ±2 meV but become similar as that of the insulating sample at (f) E = 34 ± 2meV. (g) The black squares are the ratio of spin-wave intensity in the yellow area for SC and insulating samples. The orange circles are the ratio of excitations in (h) yellow area + green area for SC and insulating samples.

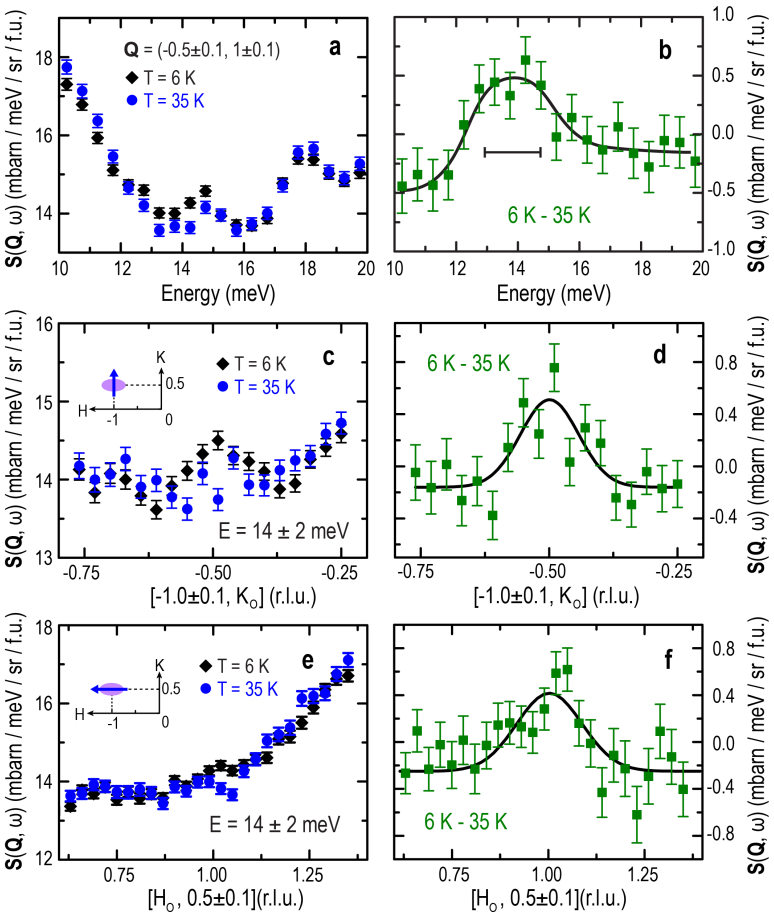

Figure 4.15: (a) Energy cut at the resonance position by integrating Q = (0.5 ± 0.1,1 ± 0.1). (b) $6K - 35K$ data shows a resonance at E = 14 meV with solid curve guides to the eye. The horizontal bar is the estimated instrumental energy resolution. (c,e) Constantenergy cuts along the [H,1 ± 0.1] and [0.5 ± 0.1,K] directions, respectively. (d,f) $6{-}35K$data confirm the resonance peak at (1,0.5) with a width FWHM = 0.13 ± 0.04 along the H direction and FWHM = 0.20 ± 0.05 along the K direction. The black curves are Gaussian fits to the peaks in (d,f).

of the spin excitations for copper oxide superconductors [180, 181] and insulating $La_{2x}Sr_xCoO_4$ [182]. This suggests that the (π,0) spin excitations stem from strongly correlated electronic physics and may be associated with dynamic stripes [183]. Third, the reduction in the low-energy spin wave intensity for the block AF phase in the SC $Rb_{0.82}Fe_{1.68}Se_2$ and the concurrent appearance of the incommensurate spin excitations near Q = (π,0) indicate that spin excitations in Q = (π,0) excitation are compensated by spin waves in the AF block phase.

Since neutron is a bulk probe, we cannot conclusively determine whether the phase from which the (π,0) spin excitations arise is superconducting or not. Additionally, neutron resonance was observed in later experiments in $K_yFe_{1.6+x}Se_2$ without any excitations near Q=(π,0) [184, 185]. So we only point out that the phase give rise to (π,0) does appear in one of the superconducting compound and might be a transition phase between non-SC and optimal SC, which might be related to superconductivity.

In summary, we have discovered that the SC $Rb_{0.82}Fe_{1.68}Se_2$ has spin excitations near the (π,0) wave vector that are disallowed in the Fermi surface nesting picture. The intensity gain near (π,0) in the SC sample is at the expense of spin-wave intensity reduction of the insulating phase. These results suggest the presence of local moments in the SC $Rb_{0.82}Fe_{1.68}Se_2$.

Chapter 5

Summary

In summary, we have carried out the neutron scattering experiments on two different types of superconductors: the MFe_2As_2 (M = Ca, Sr, Ba) (122) system and the $A_xFe_{1.6+x}Se_2$ (A = K, Rb, Cs) (245) system. In the measurements of $BaFe_{2-x}Ni_xAs_2$, we investigated the low-energy excitation especially the neutron spin resonance modes. The result revealed the correlation between resonance energy E_R and superconducting transition temperature T_c. The magnetic field was discovered to enhance the static AF order and suppress the spin resonance at the same time. The newly discovered $Rb_xFe_{1.6+x}Se_2$ was also measured using time-of-flight spectroscopy. The magnetic excitations in the AF state, the paramagnetic state and the superconducting state were measured to generate a systematic plot of this system. It was discovered that the local electrons may play an essential role in this type of material.

Interestingly, although the latter system (245) was discovered in 2010, two and half years later than the earlier one (122), the research efforts on 245 materials already faded compare to the still on-going experiments in the 122 materials. This is partly because of the great difficulty to determine the chemical phase that is responsible to the superconductivity. However, there are some new efforts that shed light on the research of the classical yet still young 122 system.

One of the efforts is to take advantage of the sample size and try to measure some extremely weak signals. The signal of magnetic order in lightly under-doped $BaFe_2As_2$ is hundreds of times smaller than that in its parent compound. In this regime, the suppression of the orthorhombic phase happens together with the commensurate-incommensurate evolution of the magnetic Bragg peak. Our recent experiments showed that even in the optimally doped sample, the magnetic signal remains with an un-changed transition temperature still higher than T_c [186]. This type of measurement takes a very long time even on large samples (e.g. typical elastic neutron experiments will count for several seconds per point, while recent experiments on weak signals count for tens of minutes per point). However, they do reveal some extremely important features of IBS superconductors.

Another trend is to measure the single crystal using new control parameters. A new kind of uniaxial pressure device was used to de-twin the single crystals in the orthorhombic phase. By applying uniaxial pressure and cooling down below T_s, the shorter axis b of each domain will align along the direction of the pressure. In the case of neutron scattering, it was discovered that the uni-axial pressure may increase the Néel temperature T_N. More interesting results would come from those experiments in superconductors in the tetragonal phase, where the uniaxial pressure acts as a trigger of symmetry breaking and may affect the magnetic excitations in superconductors.

Besides neutron scattering techniques, the newly developed Resonant Inelastic X-ray Scattering (RIXS) techniques also have the ability to probe the magnetic excitations in materials. Recent experiments in copper-oxide superconductors and iron-pnictides both reveal clear dispersing spin excitation up to hundreds of meV. Although the resolution of the RIXS is not as good as neutrons, it has no sample-size requirement, and its different cross section provides an alternative way to investigate the high-energy excitations, which may reveal some unexpected result that cannot be obtained by neutron scattering.

So far, tremendous amounts of work, experimental, numerical and theoretical, have been put into unconventional superconductivity, but its microscopic origin

remains unclear. The improvement of the experimental methods, the increasing computational power, as well as the discovery of new samples will help people to have better understanding of this phenomenon.

Bibliography

[1] H. K. Onnes. Commun. Phys. Lab. Univ. Leiden **12**: 120(1911). 2

[2] W. Meissner, R. Ochsenfeld. Naturwissenschaften **21**, 44: 787788(1933). 2

[3] F. London. Physical Review **74**, 5: 562573(1948). 3

[4] J. Bardeen, L. N. Cooper, J. R. Schrieffer. Physical Review B **108**, 1175: 162164.(1957). 3

[5] S. L. Budko, G. Lapertot,C. Petrovic,C. E. Cunningham,N. Anderson,P. C. Canfield. Physical Review Letters **86**, (9): 1877(2001). 5

[6] J. G. Bednorz, K. A. Muller. Z.Phys. B-Condens. Mat. **64**, 189 (1986). 5

[7] A. SCHILLING, M. CANTONI, J. D. GUO & H. R. OTT. Nature **363**, 56 - 58 (1993). 5

[8] M. K. Wu, J. R. Ashburn, and C. J. Torng, P. H. Hor, R. L. Meng, L. Gao, Z. J. Huang, Y. Q. Wang, C. W. Chu. Phys. Rev. Lett. **58**, 908910 (1987). 5

[9] C. W. Chu, L. Gao, F. Chen, Z. J. Huang, R. L. Meng, Y. Y. Xue. Nature **365**, 323 - 325 (1993). 5

[10] M. A. Kastner, R. J. Birgeneau, G. Shirane *et al.* Rev. Mod. Phys. **70**,897(1998). 5

[11] D. Vaknin *et al.* Phys. Rev. Lett. **58**,2802(1987). 5

[12] H. Kimura, K. Hirota, H. Matushita, K. Yamada *et al.* Phys. Rev. B, **59**,6517(1999). 7

[13] S. D. Wilson *et al.* Phys. Rev. Lett. **96**, 157001(2006). 7, 38, 47

[14] P. Dai, S. Li. Wuli, **35**, 10(2006). 7

[15] Yoichi Kamihara, Hidenori Hiramatsu, Masahiro Hirano, Ryuto Kawamura, Hiroshi Yanagi, Toshio Kamiya, Hideo Hosono. J. Am. Chem. Soc. **128**, (31): 1001210013(2006). 7, 9

[16] Y. Kamihara, T. Watanabe, M. Hirano, and H. Hosono. J. Am. Chem. Soc. **130**, 3296 (2008). 7, 9

[17] I. I. Mazin. Nature (London) **464**, 183 (2010). 8, 61

[18] J. W. Lynn, Pengcheng Dai. Physica C **469**, 469-476 (2009). 9, 11, 12

[19] J. G. Guo *et al.* Phys. Rev. B **82**, 180520(R) (2010). 10, 23

[20] Igor I. Mazin. Nature, **464**, 7286(2010). 10

[21] B.I. Zimmer, W. Jeitschko, J.H. Albering, R. Glaum, M. Reehuis. J. Alloys Compd. **229** (238) (1995). 12

[22] R. Pottgen, D. Johrendt. Z. Naturforsch **63** (1135) (2008).

[23] M. Pfisterer, G. Nagorsen. Z. Naturforsch. B **35**, (703) (1980).

[24] Joshua H. Tapp, Zhongjia Tang, Bing Lv, Kalyan Sasmal, Bernd Lorenz, Paul C.W. Chu. Arnold M. Guloy, Phys. Rev. B **78**, (060505R) (2008). 13

[25] Michael J. Pitcher, Dinah R. Parker, Paul Adamson. Chem. Commun. 5918(2008). 13

[26] D. Fruchart, P. Convert, P. Wolfers, R. Madar, J.P. Senateur, R. Fruchart. Mater. Res. Bull. **10**, 169(1975). 12, 13

[27] Chenglin Zhang *et al.* Unpublished. 13

[28] C. de la Cruz, Q. Huang, J. W. Lynn, J. Li, W. Ratcliff II, J. L. Zarestky, H. A. Mook, G. F. Chen, J. L. Luo, N. L. Wang, and P. Dai. Nature (London) **453**, 899 (2008). 13, 61, 83

[29] C.H. Lee, A. Iyo, H. Eisaki, H. Kito, M.T. Fernandez-Diaz, T. Ito, K. Kihou, H. Matsuhata, M. Braden, K. Yamada. J. Phys. Soc. Jpn. **77**, (083704) (2008).

[30] M.A. McGuire, A.D. Christianson *et al.* Phys. Rev. B **78**, 094517(2008).

[31] Q. Huang, J. Zhao, J.W. Lynn, G.F. Chen, J.L. Lou, N.L. Wang, P. Dai. Phys. Rev. B **78**, 054529(2008).

[32] M. Ishikado, R. Kajimoto, S. Shamoto, M. Arai, A. Iyo, K. Miyazawa, P. M. Shirage, H. Kito, H. Eisaki, S.-W. Kim, H. Hosono, T. Guidi, R. Bewley, S.M. Bennington. arxiv:/0809.5128v2. 13

[33] Q. Huang, Y. Qiu, W. Bao, J.W. Lynn, M.A. Green, Y.C. Gasparovic, T. Wu, G. Wu, X.H. Chen. Phys. Rev. Lett. **101**, 257003 (2008). 13

[34] M. Kofu, Y. Qiu, Wei Bao, S.-H. Lee, S. Chang, T. Wu, G. Wu, X.H. Chen. New J. Phys. **11**, 055001(2009).

[35] Y. Su, P. Link, A. Schneidewind, Th. Wolf, P. Adelmann, Y. Xiao, M. Meve, R. Mittal, M. Rotter, D. Johrendt, Th. Brueckel, M. Loewenhaupt. Phys. Rev. B **79**, 064504(2009). 13

[36] S. Margadonna, Y. Takabayashi, M.T. McDonald, K. Kasperkiewicz, Y. Mizuguchi, Y. Takano, A.N. Fitch, E. Suarde, K. Prassides. Chem. Commun. 5607 (2008). 13

[37] W. Bao, Y. Qiu, Q. Huang, M.A. Green, P. Zajdel, M.R. Fitzsimmons, M. Zhernenkov, M. Fang, B. Qian, E.K. Vehstedt, J. Yang, H.M. Pham, L. Spinu, Z.Q. Mao. Phys. Rev. Lett. **102**, 247001 (2009).

[38] S. Li, C. de la Cruz, Q. Huang, Y. Chen, J.W. Lynn, J. Hu, Y.-L Huang, F.-C. Hsu, K.-W. Yeh, M.-K. Wu, P. Dai. Phys. Rev. B **79**, 054503 (2009).

[39] T.M. McQueen, Q. Huang, V. Ksenofontov, C. Felser, Q. Xu, H.W. Zandbergen, Y.S. Hor, J. Allred, A.J. Williams, D. Qu, J. Checkelsky, N.P. Ong, R.J. Cava. Rev. B **79**, 014522 (2009). 13

[40] D. J. Singh. Physica C **469**, 418(2009). 14

[41] Jun Zhao, Q. Huang, C. de la Cruz, Shiliang Li, J. W. Lynn, Y. Chen, M. A. Green, G. F. Chen, G. Li, Z. Li, J. L. Luo, N. L. Wang, Pengcheng Dai. Nature Materials **7**, 953 (2008). 15

[42] Y. Qiu, W. Bao, Q. Huang, T. Yildirim, J.M. Simmons, M.A. Green, J.W. Lynn, Y.C. Gasparovic, J. Li, T. Wu, G. Wu, X.H. Chen. Phys. Rev. Lett. **101**, (257002) (2008).

[43] J. Zhao, Q. Huang, Clarina de la Cruz, J.W. Lynn, M.D. Lumsden, Z.A. Ren, J. Yang, X. Shen, X. Dong, Z. Zhao, P. Dai. Phys. Rev. B **78**, (132504) (2008).

[44] S.A.J. Kimber, D.N. Argyriou, F. Yokaichiya, K. Habicht, S. Gerischer, T. Hansen, T. Chatterji, R. Klingeler, C. Hess, G. Behr, A. Kondrat, B. Buchner. Phys. Rev. B **78**, (140503) (2008). 15

[45] C. de la Cruz, Q. Huang, J.W. Lynn, J. Li, W. Ratcliff II, J.L. Zarestky, H.A. Mook, G.F. Chen, J.L. Luo, N.L. Wang, P. Dai. Nature **453**, (899) (2008). 16

[46] J. Zhao, Q. Huang, C. de al Cruz, S. Li, J.W. Lynn, Y. Chen, M.A. Green, G.F. Chen, G. Li, Z.C. Li, J.L. Luo, N.L. Wang, P. Dai. Nature Mater. **7**, (953) (2008). 17

[47] A.D. Christianson *et al.* Phys. Rev. Lett **103**, 087002 (2009). 18

[48] D.K. Pratt *et al.* Phys. Rev. Lett **103**, 087001 (2009). 18

[49] Miaoyin Wang, Huiqian Luo, Jun Zhao, Chenglin Zhang, Meng Wang, Karol Marty, Songxue Chi, Jeffrey W. Lynn, Astrid Schneidewind, Shiliang Li, Pengcheng Dai. Phys. Rev. B **81**, 174524 (2010). 18, 19

[50] S. Nandi, M. G. Kim, A. Kreyssig, R. M. Fernandes, D. K. Pratt, A. Thaler, N. Ni, S. L. Budko, P. C. Canfield, J. Schmalian, R. J. McQueeney, A. I. Goldman. Phys. Rev. Lett. **104**, 057006 (2010). 19

[51] Xingye Lu, H. Gretarsson, Rui Zhang, Xuerong Liu, Huiqian Luo, Wei Tian, Mark Laver, Z. Yamani, Young-June Kim, A. H. Nevidomskyy, Qimiao Si, Pengcheng Dai. Phys. Rev. Lett. **110**, 257001 (2013). 19

[52] Huiqian Luo, Rui Zhang, Mark Laver, Zahra Yamani, Meng Wang, Xingye Lu, Miaoyin Wang, Yanchao Chen, Shiliang Li, Sung Chang, Jeffrey W. Lynn, Pengcheng Dai. Phys. Rev. Lett **108**, 247002 (2012). 19, 20

[53] D. K. Pratt, M. G. Kim, A. Kreyssig, Y. B. Lee, G. S. Tucker, A. Thaler,W. Tian, J. L. Zarestky, S. L. Budko, P. C. Canfield, B. N. Harmon, A. I. Goldman, R. J. McQueeney. Phys. Rev. Lett **106**, 257001 (2011). 20

[54] J. Zhao *et al.* Nat. Phys. **5**, 555-560 (2009). 21, 22, 61, 62, 63, 65, 66, 71, 73

[55] L. W. Harriger *et al.* Phys. Rev. B **84**, 054544 (2011). 21, 22, 61, 62, 63, 65, 66, 71, 73, 74, 75, 78, 84, 89

[56] O. J. Lipscombe, G. F. Chen, Chen Fang, T. G. Perring, D. L. Abernathy, A. D. Christianson, Takeshi Egami, Nanlin Wang, Jiangping Hu, Pengcheng Dai. Phys. Rev. Lett. **106**, 057004(2011). 21, 22

[57] M. Wang *et al.* Phys. Rev. B **84**, 094504 (2011). 21, 61, 63, 65, 74, 75, 79, 82, 83, 86

[58] M. S. Liu, L. W. Harriger, H. Q. Luo, M. Wang, R. A. Ewings, T. Guidi, H. Park, K. Haule, G. Kotliar, S. M. Hayden, and P. C. Dai. Nat. Phys. **8**, 376 (2012). 21, 23, 78

[59] Miaoyin Wang, Chen Fang, Dao-Xin Yao, GuoTai Tan, Leland W. Harriger, Yu Song, Tucker Netherton, Chenglin Zhang, Meng Wang, Matthew B. Stone, Wei

Tian, Jiangping Hu, Pengcheng Dai. Nature Communications **2**, 580 (2011). 22, 73

[60] Meng Wang *et al.* Unpublished. 23

[61] A. Krzton-Maziopa *et al.* J. Phys.: Condens. Matter **23**, 052203 (2011). 23, 61, 83

[62] M. H. Fang, H. D. Wang, C. H. Dong, Z. J. Li, C. M. Feng, J. Chen, H. Q. Yuan. Europhys. Lett. **93**, 47004 (2011). 61, 83

[63] A.F. Wang *et al.* Phys. Rev. B **83**, 060512 (2011).

[64] D.M. Wang *et al.* P hys. Rev. B **83**, 132502 (2011). 23

[65] W. Bao *et al.* Chinese Phys. Lett. **28**, 086104 (2011). 24, 61, 63, 65, 70, 74, 83, 86

[66] F. Ye, S. Chi, Wei Bao, X. F. Wang, J. J. Ying, X. H. Chen, H. D. Wang, C. H. Dong, M. H. Fang. Phys. Rev. Lett. **107**, 137003 (2011). 24, 74, 75, 79, 82, 83, 86

[67] W. Bao *et al.* Chinese Physics Letters 30, 027402 (2013). 24, 61, 63, 65, 70

[68] Huiqian Luo, Zhaosheng Wang, Huan Yang, Peng Cheng, Xiyu Zhu, Hai-Hu Wen. Supercond. Sci. Technol. **21**, 125014 (2008). 29

[69] Yanchao Chen, Xingye Lu, Meng Wang, Huiqian Luo, Shiliang Li. Supercond. Sci. Technol. **24**, 065004 (2011). 29

[70] G. L. Squires. Introduction to the Theory of Thermal Neutron Scattering, Dover Publications (1996). 32

[71] G. Shirane, S. M. Shapiro, J. M. tranquada. Neutron Scattering with a Triple-Axis Spectrometer: Basic Techniques, Cambridge University Press (2002). 32

[72] I. I. Mazin, D. J. Singh, M. D. Johannes, and M. H. Du. Phys. Rev. Lett. **101**, 057003 (2008). 38, 48

[73] A. V. Chubukov. Physica C **469**, 640 (2009).

[74] F. Wang, H. Zhai, Y. Ran, A. Vishwanath, and D.-H. Lee. Phys. Rev. Lett. **102**, 047005 (2009).

[75] V. Cvetkovic and Z. Tesanovic. Eur. Phys. Lett. **85**, (2009). 71

[76] A. Moreo, M. Daghofer, J. A. Riera, and E. Dagotto. Phys. Rev. B **79**, 134502 (2009). 38, 48

[77] I. I. Mazin and J. Schmalian. Physica C **469**, 614 (2009). 38, 50

[78] T. A. Maier and D. J. Scalapino. Phys. Rev. B **78**, 020514(R) (2008). 38

[79] T. A. Maier, S. Graser, D. J. Scalapino, and P. Hirschfeld. Phys. Rev. B **79**, 134520 (2009). 48

[80] M. M. Korshunov, I. Eremin. Phys. Rev. B **78**, 140509(R) (2008). 50, 61, 83

[81] Kangjun Seo, Chen Fang, B. Andrei Bernevig, and Jiangping Hu. Phys. Rev. B **79**, 235207 (2009). 38, 48

[82] S. X. Chi, A. Schneidewind, J. Zhao, L. W. Harriger, L. J. Li, Y. K. Luo, G. H. Cao, Z. A. Xu, M. Loewenhaupt, J. P. Hu, and P. C. Dai. Phys. Rev. Lett. **102**, 107006 (2009). 38, 39

[83] A. D. Christianson, E. A. Goremychkin, R. Osborn, S. Rosenkranz, M. D. Lumsden, C. D. Malliakas, I. S. Todorov, H. Claus, D. Y. Chung, M. G. Kanatzidis, R. I. Bewley and T. Guidi. Nature (London) **456**, 930 (2008). 61

[84] M. D. Lumsden, A. D. Christianson, D. Parshall, M. B. Stone, S. E. Nagler, G. J. MacDougall, H. A. Mook, K. Lokshin, T. Egami, D. L. Abernathy, E. A. Goremychkin, R. Osborn, M. A. McGuire, A. S. Sefat, R. Jin, B. C. Sales, and D. Mandrus. Phys. Rev. Lett. **102**, 107005 (2009). 38, 46, 83

[85] S. L. Li, Y. Chen, S. Chang, J. W. Lynn, L. J. Li, Y. K. Luo, G. H. Cao, Z. A. Xu, and P. C. Dai. Phys. Rev. B **79**, 174527 (2009). 38

[86] D. Parshall, K. A. Lokshin, Jennifer Niedziela, A. D. Christianson, M. D. Lumsden, H. A. Mook, S. E. Nagler, M. A. McGuire, M. B. Stone, D. L. Abernathy, A. S. Sefat, B. C. Sales, D. G. Mandrus, and T. Egami. Phys. Rev. B **80**, 012502 (2009).

[87] D. K. Pratt, W. Tian, A. Kreyssig, J. L. Zarestky, S. Nandi, N. Ni, S. L. Bud'ko, P. C. Canfield, A. I. Goldman, and R. J. McQueeney. Phys. Rev. Lett. **103**, 087001 (2009). . 41, 43, 46, 50, 51, 52, 53

[88] A. D. Christianson, M. D. Lumsden, S. E. Nagler, G. J. MacDougall, M. A. McGuire, A. S. Sefat, R. Jin, B. C. Sales, and D. Mandrus. Phys. Rev. Lett. **103**, 087002 (2009). 41, 43, 50, 51, 52, 53

[89] D. S. Inosov, J. T. Park, P. Bourges, D. L. Sun, Y. Sidis, A. Schneidewind, K. Hradil, D. Haug, C. T. Lin, B. Keimer and V. Hinkov. Nat. Phys. **6**, 178 (2010). 38, 46, 83

[90] O. J. Lipscombe, G. F. Chen, C. Fang, T. G. Perring, D. L. Abernathy, A. D. Christianson, T. Egami, N. L. Wang, J. P. Hu, and P. C. Dai. Phys. Rev. Lett. **106**, 057004 (2011). 38, 61, 62, 65, 66, 71, 73

[91] J. Rossat-Mignod, L. P. Regnault, C. Vettier, P. Bourges, P. Burlet, J. Bossy, J. Y. Henry, and G. Lapertot. Physica C (Amsterdam) **185**, 86 (1991). 38

[92] H. F. Fong, B. Keimer, D. Reznik, D. L. Milius, and I. A. Aksay. Phys. Rev. B **54**, 6708 (1996).

[93] C. Stock, W. J. L. Buyers, R. Liang, D. Peets, Z. Tun, D. Bonn, W. N. Hardy, and R. J. Birgeneau. Phys. Rev. B **69**, 014502 (2004).

[94] Jun Zhao, Pengcheng Dai, Shiliang Li, Paul G. Freeman, Y. Onose, Y. Tokura. Phys. Rev. Lett. **99**, 017001 (2007). 38, 47

[95] Jun Zhao, Dao-Xin Yao, Shiliang Li, Tao Hong, Y. Chen, S. Chang, W. Ratcliff, II, J. W. Lynn, H. A. Mook, G. F. Chen, J. L. Luo, N. L. Wang, E. W. Carlson, Jiangping Hu, and Pengcheng Dai. Phys. Rev. Lett. **101**, 167203 (2008). 38, 41

[96] R. A. Ewings, T. G. Perring, R. I. Bewley, T. Guidi, M. J. Pitcher, D. R. Parker, S. J. Clarke, and A. T. Boothroyd. Phys. Rev. B **78**, 220501(R) (2008).

[97] R. J. McQueeney, S. O. Diallo, V. P. Antropov, G. D. Samolyuk, C. Broholm, N. Ni, S. Nandi, M. Yethiraj, J. L. Zarestky, J. J. Pulikkotil, A. Kreyssig, M. D. Lumsden, B. N. Harmon, P. C. Canfield, and A. I. Goldman. Phys. Rev. Lett. **101**, 227205 (2008).

[98] K. Matan, R. Morinaga, K. Iida, and T. J. Sato. Phys. Rev. B **79**, 054526 (2009).

[99] S. O. Diallo, V. P. Antropov, T. G. Perring, C. Broholm, J. J. Pulikkotil, N. Ni, S. L. Bud'ko, P. C. Canfield, A. Kreyssig, A. I. Goldman, and R. J. McQueeney. Phys. Rev. Lett. 102, 187206 (2009). 73

[100] Jun Zhao, D. T. Adroja, Dao-Xin Yao, R. Bewley, Shiliang Li, X. F. Wang, G. Wu, X. H. Chen, Jiangping Hu and Pengcheng Dai. Nat. Phys. **5**, 555 (2009). 38

[101] S. Chi, A. Schneidewind, J. Zhao, L. W. Harriger, L. Li, Y. Luo, G. Cao, Zhuan Xu, M. Loewenhaupt, J. Hu, and P. Dai. Phys. Rev. Lett. **102**, 107006 (2009). 38, 39, 41, 44, 46, 48, 83

[102] Shiliang Li, Ying Chen, Sung Chang, Jeffrey W. Lynn, Linjun Li, Yongkang Luo, Guanghan Cao, Zhuan Xu, and Pengcheng Dai. Phys. Rev. B **79**, 174527 (2009). 38, 39, 41, 46, 48

[103] L. J. Li, Y. K. Luo, Q. B. Wang, H. Chen, Z. Ren, Q. Tao, Y. K. Li, X. Lin, M. He, Z. W. Zhu, G. H. Cao, and Z. A. Xu. New J. Phys. **11**, 025008 (2009). 41

[104] Leland W. Harriger, Astrid Schneidewind, Shiliang Li, Jun Zhao, Zhengcai Li, Wei Lu, Xiaoli Dong, Fang Zhou, Zhongxian Zhao, Jiangping Hu, and Pengcheng Dai. Phys. Rev. Lett. **103**, 087005 (2009). 46, 48

[105] Jun Zhao, Louis-Pierre Regnault, Chenglin Zhang, Miaoying Wang, Zhengcai Li, Fang Zhou, Zhongxian Zhao, Pengcheng Dai. Phys. Rev. B **81**, 180505(2010). 46

[106] T. A. Maier and D. J. Scalapino. Phys. Rev. B **78**, 020514(R) (2008). 48, 61, 83

[107] M. Y. Wang *et al.* Phys. Rev. B **81**, 174524 (2010). 50, 51, 52, 53, 71

[108] R. M. Fernandes, D. K. Pratt, W. Tian, J. Zarestky, A. Kreyssig, S. Nandi, M. G. Kim, A. Thaler, N. Ni, P. C. Canfield, R. J. McQueeney, J. Schmalian, A. I. Goldman. Phys. Rev. B **81**, 140501(R) (2010). 50, 57

[109] R. M. Fernandes and J. Schmalian. Phys. Rev. B **82**, 014521 (2010). 50, 57

[110] C. Fang, H. Yao, W.-F. Tsai, J. P. Hu, and S. A. Kivelson. Phys. Rev. B **77**, 224509 (2008). 50

[111] C. Xu, M. Müller, and S. Sachdev. Phys. Rev. B **78**, 020501 (2008). 50

[112] C. Lester, Jiun-Haw Chu, J. G. Analytis, S. C. Capelli, A. S. Erickson, C. L. Condron, M. F. Toney, I. R. Fisher, and S. M. Hayden. Phys. Rev. B **79**, 144523 (2009). 50

[113] H. J. Kang, P. Dai, H. A. Mook, D. N. Argyriou, V. Sikolenko, J. W. Lynn, Y. Kurita, S. Komiya, and Y. Ando. Phys. Rev. B **71**, 214512 (2005). 50, 57

[114] S. D. Wilson, S. Li, J. Zhao, G. Mu, H.-h Wen, J. W. Lynn, P. G. Freeman, L.-P. Regnault, K. Habicht, Pengcheng Dai. PNAS **104**, 15259 (2007). 50, 57

[115] J. T. Park, D. S. Inosov, Ch. Niedermayer, G. L. Sun, D. Haug, N. B. Christensen, R. Dinnebier, A.V. Boris, A. J. Drew, L. Schulz, T. Shapoval, U. Wolff, V. Neu, Xiaoping Yang, C. T. Lin, B. Keimer, and V. Hinkov. Phys. Rev. Lett. **102**, 117006 (2009). 50

[116] J. Zhao, L.-P. Regnault, C. L. Zhang, M. Y. Wang, Z. C. Li, F. Zhou, Z. X. Zhao, C. Fang, J. P. Hu, and P. C. Dai. Phys. Rev. B **81**, 180505(R) (2010). 51

[117] J. S. Wen, G. Y. Xu, Z. J. Xu, Z. W. Lin, Q. Li, Y. Chen, S. X. Chi, G. D. Gu, and J. M. Tranquada. Phys. Rev. B **81**, 100513 (2010). 51

[118] J. A. Ridriguez, D. M. Adler, P. C. Brand, C. Broholm, J. C. Cook, C. Brocker, R. Hammond, Z. Huang, P. Hundertmark, J. W. Lynn, N. C. Maliszewskyj, J. Moyer, J. Orndorff, D. Pierce, T. D. Pike, G. Scharfstein, S. A. Smee, and R. Vilaseca. Meas. Sci. Technol. **19**, 034023 (2008). 52

[119] A. Yamamoto, J. Jaroszynski, C. Tarantini, L. Balicas, J. Jiang, A. Gurevich, D. C. Larbalestier, R. Jin, A. S. Sefat, M. A. McGuire, B. C. Sales, D. K. Christen, and D. Mandrus. App. Phys. Lett. **94**, 062511 (2009). 56, 58

[120] S. Katano, M. Sato, K. Yamada, T. Suzuki, and T. Fukase. Phys. Rev. B **62**, 14677(R) (2000). 57

[121] B. Khaykovich, Y. S. Lee, R. W. Erwin, S.-H. Lee, S. Wakimoto, K. J. Thomas, M. A. Kastner, and R. J. Birgeneau. Phys. Rev. B **66**, 014528 (2002).

[122] B. Lake, H. M. Ronnow, N. B. Christensen, G. Aeppli, K. Lefman, D. F. McMorrow, P. Vorderwisch, P. Smeibidl, N. Mangkornton, T. Sasagawa, M. Nohara, H. Takagi, and T. E. Mason. Nature (London) **415**, 299 (2002). 57

[123] Y. Zhang, E. Demler, and S. Sachdev. Phys. Rev. B **66**, 094501 (2002). 57

[124] J. Chang, Ch. Niedermayer, R. Gilardi, N. B. Christensen, H. M. Ronnow, D. F. McMorrow, M. Ay, J. Stahn, O. Sobolev, A. Hiess, S. Pailhes, C. Baines, N. Momono, M. Oda, M. Ido, and J. Mesot. Phys. Rev. B **78**, 104525 (2008). 57

[125] P. C. Dai, H. A. Mook, G. Aeppli, S. M. Hayden, and F. Doğan. Nature (London) **406**, 965 (2000). 57

[126] D. Haug, V. Hinkov, A. Suchaneck, D. S. Inosov, N. B. Christensen, Ch. Niedermayer, P. Bourges, Y. Sidis, J. T. Park, A. Ivanov, C. T. Lin, J. Mesot, and B. Keimer. Phys. Rev. Lett. **103**, 017001 (2009). 57

[127] C. Stock, W. J. L. Buyers, K. C. Rule, J.-H. Chung, R. Liang, D. Bonn, and W. N. Hardy. Phys. Rev. B **79**, 184514 (2009). 57

[128] G. M. Luke and Y. J. Uemura. (private communications). 57

[129] T. J. Williams, A. A. Aczel, E. Baggio-Saitovitch, S. L. Bud'ko, P. C. Canfield, J. P. Carlo, T. Goko, H. Kageyama, A. Kitada, J. Munevar, N. Ni, S. R. Saha, K. Kirschenbaum, J. Paglione, D. R. Sanchez-Candela, Y. J. Uemura, and G. M. Luke. Phys. Rev. B **82**, 094512 (2010). 58

[130] D. C. Johnston. Adv. in Phys. **59**, 803 (2010). 61, 62

[131] J. G. Guo *et al.* Rev. B **82**, 180520(R) (2010). 61, 83

[132] A. F. Wang *et al.* Phys. Rev. B **83**, 060512 (2011). 61, 83

[133] D. M. Wang, J. B. He, T.-L. Xia, G. F. Chen. Phys. Rev. B **83**, 132502 (2011). 61

[134] Y. Zhang *et al.* Nature Materials **10**, 273-277 (2011). 61, 83, 84, 89

[135] T. Qian *et al.* Phys. Rev. Lett. **106**, 187001 (2011).

[136] D. X. Mou *et al.* Phys. Rev. Lett. **106**, 107001 (2011). 61, 83, 84, 89

[137] I. I. Mazin. Physics **4**, 26 (2011). 61, 83

[138] L. Häggström, A. Seidel, and R. Berger. J. Magn. Magn. Mater. **98**, 37 (1991). 61, 83

[139] J. Bacsa *et al.* Chem. Sci. **2**, 1054 (2011).

[140] V. Yu *et al.* Phys. Rev. B **83**, 144410 (2011). 61, 63, 65, 70, 83, 86

[141] K. Seo, B. A. Bernevig, J. P. Hu. Phys. Rev. Lett. **101**, 206404 (2008). 61

[142] R. A. Ewings *et al.* Phys. Rev. B **83**, 214519 (2011). 61, 62, 63, 65, 66, 71

[143] C. Cao, J. Dai. Phys. Rev. Lett. **107**, 056401 (2011). 66

[144] Y. Z. You, H. Yao, D.-H. Lee. Phys. Rev. B **84**, 020406 (2011). 67

[145] C. Fang, B. Xu, P. C. Dai, T. Xiang, J. P. Hu. Phys. Rev. B **85**, 134406 (2012).

[146] F. Lu, X. Dai. (http://arxiv.org/abs/1103.5521).

[147] R. Yu, P. Goswami, Q. Si. Phys. Rev. B **84**, 094451 (2011). 66, 67

[148] C. Lester, Jiun-Haw Chu, J. G. Analytis, S. C. Capelli, A. S. Erickson, C. L. Condron, M. F. Toney, I. R. Fisher, and S. M. Hayden. Phys. Rev. B **79**, 144523 (2009). 68

[149] J. Lorenzana, G. Seibold, and R. Coldea. Phys. Rev. B **72**, 224511 (2005). 70, 78

[150] Q. Si, E. Abrahams. Phys. Rev. Lett. **101**, 076401 (2008). 72

[151] R. A. Ewings, T. G. Perring, J. Gillett, S. D. Das, S. E. Sebastian, A. E. Taylor, T. Guidi, and A. T. Boothroyd. Phys. Rev. B 83, 214519 (2011). 73

[152] S. O. Diallo, D. K. Pratt, R. M. Fernandes, W. Tian, J. L. Zarestky, M. Lumsden, T. G. Perring, C. L. Broholm, N. Ni, S. L. Bud'ko, P. C. Canfield, H.-F. Li, D. Vaknin, A. Kreyssig, A. I. Goldman, and R. J. McQueeney. Phys. Rev. B **81**, 214407 (2010).

[153] H. Park, K. Haul, and G. Kotliar. Phys. Rev. Lett. **107**, 137007 (2011).

[154] A. L. Wysocki, K. D. Belashchenko, and V. P. Antropov. Nature Phys. **7**, 485 (2011).

[155] R. Yu, Z. T. Wang, P. Goswami, A. H. Nevidomskyy, Q. Si, and E. Abrahams. Phys. Rev. B **86**, 085148 (2012). 73

[156] M. H. Fang, H. M. Pham, B. Qian, T. J. Liu, E. K. Vehstedt, Y. Liu, L. Spinu, and Z. Q. Mao. Phys. Rev. B **78**, 224503, (2008). 73

[157] W. Bao, Y. Qiu, Q. Huang, M. A. Green, P. Zajdel, M. R. Fitzsimmons, M. Zhernenkov, S. Chang, M. H. Fang, B. Qian, E. K. Vehstedt, J. H. Yang, H. M. Pham, L. Spinu, and Z. Q. Mao. Phys. Rev. Lett. **102**, 247001 (2009).

[158] S. L. Li, C. de la Cruz, Q. Huang, Y. Chen, J. W. Lynn, J. P. Hu, Y. L. Huang, F-C. Hsu, K. W. Yeh, M.-K. Wu, and P. C. Dai. Phys. Rev. B **79**, 054503 (2009). 73

[159] I. A. Zaliznyak, Z. J. Xu, J. M. Tranquada, G. D. Gu, A. M. Tsvelik, and M. B. Stone. Phys. Rev. Lett. **107**, 216403 (2011). 73, 74, 78, 80, 81

[160] L. W. Harriger, M. S. Liu, H. Q. Luo, R. A. Ewings, C. Frost, T. G. Perring, and P. C. Dai. Phys. Rev. B **86**, 140403(R) (2012). 73, 74, 75, 78, 80, 81

[161] R. Yu, J.-X. Zhu, and Q. Si. Phys. Rev. Lett. **106**, 186401 (2011). 73

[162] Q. Huang, Y. Qiu, W. Bao, M. A. Green, J. W. Lynn, Y. C. Gasparovic, T. Wu, G. Wu, and X. H. Chen. Phys. Rev. Lett. 101, 257003 (2008). 73

[163] J. Zhao, W. Ratcliff, II, J. W. Lynn, G. F. Chen, J. L. Luo, N. L. Wang, J. P. Hu, and P. C. Dai. Phys. Rev. B 78, 140504(R) (2008). 73

[164] P. J. Hirschfeld, M. M. Korshunov, and I. I. Mazin. Rep. Prog. Phys. **74**, 124508 (2011). 73

[165] Miaoyin Wang, Chen Fang, Dao-Xin Yao, GuoTai Tan, Leland W. Harriger, Yu Song, Tucker Netherton, Chenglin Zhang, Meng Wang, Matthew B. Stone, Wei Tian, Jiangping Hu, and Pengcheng Dai. Nature Commun. **2**, 580 (2011). 74, 75, 76, 78, 79, 84, 85, 86

[166] W. Bao, Q. Huang, G. F. Chen, M. A. Green, D. M. Wang, J. B. He, X. Q. Wang, Y. Qiu. Chinese Phys. Lett. **28**, 086104 (2011). 75, 79, 82

[167] A. Tucciarone, H. Y. Lau, L. M. Corliss, A. Delapalme, and J. M. Hastings. Phys. Rev. B **4**, 3206 (1971). 78

[168] R. Coldea, S. M. Hayden, G. Aeppli, T. G. Perring, C. D. Frost, T. E. Mason, S.-W. Cheong, and Z. Fisk. Phys. Rev. Lett. **86**, 5377 (2001). 81

[169] X. W. Yan, M. Gao, Z. Y. Lu, and T. Xiang. Phys. Rev. B **83**, 233205 (2011). 81

[170] Y. Z. You, F. Yang, S. P. Kou, and Z. Y. Weng. Phys. Rev. Lett. **107**, 167001 (2011). 81

[171] W. G. Yin, G. H. Lin, and W. Ku. Phys. Rev. B **86**, 081106(R) (2012).

[172] Z. P. Yin, K. Haule, and G. Kotliar. Nature Mater. **10**, 932 (2011). 81

[173] W. Li, H. Ding, Z. Li, P. Deng, K. Chang, K. He, S. H. Ji, L. L. Wang, X. C. Ma, J. P. Hu, X. Chen, and Q.-K. Xue. Phys. Rev. Lett. **109**, 057003 (2012). 82

[174] J. Zhao, H. B. Cao, E. Bourret-Courchesne, D.-H. Lee, and R. J. Birgeneau. Phys. Rev. Lett. **109**, 267003 (2012). 82

[175] C. L. Zhang, M. Wang, H. Q. Luo, M. Y. Wang, M. S. Liu, J. Zhao, D. L. Abernathy, K. Marty, M. D. Lumsden, S. X. Chi, S. Chang, J. A. Rodriguez-Rivera, J. W. Lynn, T. Xiang, J. P. Hu, P. C. Dai. Scientific Reports **1**, 115 (2011). 83

[176] T. A. Maier, S. Graser, P. J. Hirschfeld, and D. J. Scalapino. Phys. Rev. B **83**, 100515(R) (2011). 83

[177] G. Friemel, J. T. Park, T. A. Maier, V. Tsurkan, Yuan Li, J. Deisenhofer, H.-A. Krug von Nidda, A. Loidl, A. Ivanov, B. Keimer, and D. S. Inosov. Phys. Rev. B **85**, 140511 (2012). 83, 84, 85, 86, 89

[178] J. T. Park, G. Friemel, Yuan Li, J.-H. Kim, V. Tsurkan, J. Deisenhofer, H.-A. Krug von Nidda, A. Loidl, A. Ivanov, B. Keimer, and D. S. Inosov. Phys. Rev. Lett. **107**, 177005 (2011). 83, 84, 85, 86, 89

[179] Q. Si and E. Abrahams. Phys. Rev. Lett. **101**, 76401 (2008). 84, 89

[180] S. M. Hayden, H. A. Mook, P. Dai, T. G. Perring, and F. Doğan. Nature **429**, 531 (2004). 84, 91

[181] J. M. Tranquada. Cond - mat / 0512115. 84, 91

[182] A. T. Boothroyd, P. Babkevich, D. Prabhakaran, and P. G. Freeman. Nature (London) **471**, 341 (2011). 84, 91

[183] S. A. Kivelson, I. P. Bindloss, E. Fradkin, V. Oganesyan, J. M. Tranquada, A. Kapitulnik, and C. Howald. Rev. Mod. Phys. **75**, 1201 (2003). 84, 91

[184] G. Friemel, W. P. Liu, E. A. Goremychkin, Y. Liu, J. T. Park, O. Sobolev, C. T. Lin, B. Keimer, D. S. Inosov. EPL **99**, 67004 (2012). 92

[185] A. E. Taylor, R. A. Ewings, T. G. Perring, J. S. White, P. Babkevich, A. Krzton-Maziopa, E. Pomjakushina, K. Conder, A. T. Boothroyd. Phys. Rev. B **86**, 094528 (2012). 92

[186] Xingye Lu, H. Gretarsson, Rui Zhang, Xuerong Liu, Huiqian Luo, Wei Tian, Mark Laver, Z. Yamani, Young-June Kim, A. H. Nevidomskyy, Qimiao Si, Pengcheng Da. Phys. Rev. Lett. **110**, 257001 (2013). 94

Vita

Miaoyin Wang was born on March 29th, 1986 in Shanghai, China. He graduated from High School Affiliated to Shanghai Jiao Tong University (HSASJTU) in 2004. After one year of study in electronic engineering at Shanghai Jiao Tong University (SJTU), he changed his major to physics. In 2008, he received a Bachelor of Science degree in physic from Shanghai Jiao Tong University and came to U.S. for further study in physics at The University of Tennessee, Knoxville. He expects to receive a Doctorate of Philosophy degree in physics in 2013.